



Danmarks  
Tekniske  
Universitet



DEPARTMENT OF ARCTIC TECHNOLOGY (UNIS)  
DEPARTMENT OF CIVIL ENGINEERING (NTNU & DTU)

TBA4900 - GEOTECHNICAL ENGINEERING  
MASTER'S THESIS

---

# GPR and in-situ measurements of different periglacial landforms in the High Arctic, Svalbard. A case study for the ExoMars mission.

---

*Author:*  
Esther Mas I Sanz

*Supervisor (UNIS):* Aleksey Shestov  
*Supervisor (NTNU):* Gustav Grimstad  
*Co-Supervisor (NTNU):* Jan Steinar Rønning  
*Supervisor (DTU):* Thomas Ingeman-Nielsen

June, 2022

# Abstract

Central Spitsbergen is known for the wide variety of periglacial landforms found in a relatively small area. Particularly, the Adventdalen Valley hosts several pingos, ice-wedge polygons (that populate terraces, flatlands and even mountain sides), gullies and massive alluvial fans. In the vicinity of Longyearbyen the periglacial domain transforms into a glacial environment bifurcating into two easily accessible cold glaciers, Longyearbreen and Larsbreen. On the other side of the fjord, meltwater channels merge into small rivers that carve the stone, exposing the soil stratification and accidentally revealing the geological history of the location. It is the proximity of all these features that poses an advantage for researchers who look for analogous geomorphologies found on ice-rich planetary bodies and perhaps to a more distant past of Mars.

In this project, a total of five sites along Adventdalen Valley have been investigated within the context of WISDOM (ExoMars GPR unit) fieldwork campaign: Longyearbreen glacier, Innerhytta and River Bed Pingo, Helvetidalen entrance (alluvial fan and polygon terrace) and Revneset-Hanaskogdalen outcrops. The main methodology for data retrieval has been GPR profiling, but it has been complemented with the drilling of ice cores when possible (and their subsequent salinity study and relative permittivity estimation), fieldwork annotations, snow investigations and GIS data analysis. Each site has provided unique GPR signatures that are contextualised with *in-situ* ground truth data and available information: detection of ice-rich soil at Innerhytta pingo, calculation of the talik ice crust at River Bed Pingo, visualisation and interpretation of rock layering at sandstone outcrop, determination of snow-ice and ice-bedrock interfaces at the glacier, etc. At the mouth of Helvetidalen valley, the target study area is an ice wedge polygon network for which geomorphometric parameters undergo an statistical analysis. The polygon area is mapped by using two GPR grids (a small one of 50 m×30 m and a large one of 160 m×70 m) in order to estimate the amount of wedge ice and its distribution. Despite no other obvious geomorphometrical correlations, the wedge ice distribution is found to be only at the troughs of lower elevations and the results of total ice volume contrast between methods, around 15% vol. (GIS-derived) and between 1.5-4.5% (GPR-derived).

This research project aims to further comprehend how ice is distributed in ice wedge polygon networks and to provide solid, contextualised data on the different periglacial (and glacial) target landforms in order to contribute in the interpretation and validation of WISDOM's analysis tools and data processing.

# Acknowledgements

The preparations for this Master Thesis started well before officially starting and many people's contributions have been essential to its completion. This work might be titled as well *Against All Odds* as the project took place despite initially lacking a GPR, having no knowledge on how to operate it and the only course at UNIS offering such lectures cancelled, while on the background a receding pandemic and an unexpected war that has caused the cancellation of ESA-Roscosmos collaborations were threatening to jeopardise the totality of the fieldwork campaign.

I would like start thanking Jan Steinar Rønning. The previous semester (during my Specialisation Project), we met a bit by chance after my unfruitful quest to find information on NTNU's GPRs. Luck was on my side because he turned out to be the main responsible of UNIS pulseEKKO unit for many years. He kindly shared his GPR and ERT lectures and provided his expertise and advice when I explained my proposals. Not only that but thanks to him I could join an NGU's ERT and GPR surveys to learn about the systems first-hand. After that, not only agreed to act as co-supervisor but also to come one last time to UNIS for teaching (me) about the GPR... on his senior holidays! If that was not enough, when the pulseEKKO's DVL broke down he arranged to have NGU's unit so I could continue my work, has also shared historical data from his former course and allowed me to work in his office when I travelled to Trondheim for data processing. I think words cannot express my enormous gratitude for all your help and such opportunities given. *Muchísimas gracias.*

I want to give a special mention to my supervisor Aleksey Shestov. First of all, thanks for accepting the project and putting all the means necessary to make it possible. I really appreciate you put all your body and soul during the exhausting 10-day WISDOM campaign providing all the help necessary with logistics, safety and problems to be solved on-the-fly. We were unsuccessful with the drilling but we can say we tried our best, it simply did not work. Also, thanks to the department leader, Gijsbert Breedveld, for giving the green light for this project. Thanks to both for your patience when dealing with my stubbornness.

I also want to thank the WISDOM team -LATMOS (Le Laboratoire Atmosphères, Observations Spatiales) and TUD (Technische Universität Dresden)- team for coming to Svalbard and giving me the opportunity to contribute in a real Space mission for ESA. It has been a pleasure to become part of the team during such an amazing endeavour. My most sincere thanks to Valérie Ciarletti (and to Jorge Vago who put me in contact with her on the first place) who after several months of doing Zoom meetings and listening to proposals decided it was worth a try to take WISDOM prototype up to the Arctic despite not knowing me personally.

I would like to also thank the NGU team for welcoming me into their fieldwork session and in particular Georgios Tassis, geophysicist at NGU, for later helping with the data processing and arranging the new DVL parcel.

In addition, thanks to the Svalbard Science Forum for awarding the AFG (Arctic Field Grant) to the *WISDOMSvalbard* project, which includes this Master Thesis.

Finally, a huge thanks to my beloved Rocca who has unconditionally supported me throughout all the project despite being busy himself with his *nanolab* investigations. Can't wait for the new adventures together!

# Contents

<b>List of Figures</b>	<b>iv</b>
<b>List of Tables</b>	<b>vi</b>
<b>1 Introduction</b>	<b>1</b>
1.1 Background	1
1.1.1 State-of-the-art	1
1.1.2 ExoMars Mission	2
1.2 Master Thesis overview	3
1.2.1 Motivation	3
1.2.2 Aims and Scope	3
1.2.3 Organisation	4
<b>2 Study Areas</b>	<b>5</b>
2.1 Central Spitsbergen, Adventdalen Region	5
2.1.1 Location and geomorphology	5
2.1.2 Glacial history and permafrost formation	6
2.1.3 Climate	6
<b>3 Periglacial Landforms</b>	<b>8</b>
3.1 Permafrost Environments	8
3.2 Patterned ground	10
3.2.1 Ice wedge polygons	14
3.2.1.1 Adventdalen polygons	15
3.3 Pingos	16
3.4 Other periglacial landforms	18
3.4.1 Alluvial fan	18
3.4.2 Gullies	19
3.5 Mars Landforms	20
<b>4 Methodology and Data retrieval</b>	<b>24</b>
4.1 Fieldwork	24
4.1.1 Site 1	25
4.1.2 Site 2	26
4.1.3 Site 3	26
4.1.4 Site 4	27
4.1.5 Site 5	28
4.2 RS and GIS	29

4.2.1	Geometrical characterisation of ice-wedge polygons . . . . .	29
4.2.2	Estimation of subsurface ice in ice-wedge polygon region . . . . .	30
4.3	GPR . . . . .	34
4.3.1	Overview of the basic principles . . . . .	34
4.3.1.1	Electromagnetic properties and wave phenomena . . . . .	34
4.3.1.2	Ground Penetrating Radar Design Specifications . . . . .	36
4.3.1.3	Velocity Analysis . . . . .	38
4.3.1.4	Signal Processing . . . . .	38
4.3.1.5	Antenna orientation . . . . .	39
4.3.2	Main GPR Unit: PulseEKKO Pro . . . . .	40
4.3.3	Other GPR units . . . . .	41
4.3.3.1	WISDOM . . . . .	41
<b>5</b>	<b>Results and Interpretation</b> . . . . .	<b>44</b>
5.1	Site 1: Longyearbreen . . . . .	44
5.1.1	Glacier measurements . . . . .	44
5.1.1.1	Snow investigation . . . . .	45
5.1.2	Ice Cave . . . . .	48
5.2	Site 2: Innerhytta Pingo . . . . .	51
5.3	Site 3: Helvetidalen . . . . .	54
5.3.1	Alluvial Fan . . . . .	54
5.3.2	Ice Wedge Polygons . . . . .	56
5.3.2.1	Geomorphology of polygons . . . . .	56
5.3.2.2	B-Scans . . . . .	60
5.3.2.3	Grid and 3D-radargrams . . . . .	63
5.3.2.4	Ice Wedge Volume estimation . . . . .	69
5.4	Site 4: River Bed Pingo . . . . .	72
5.4.1	Pingo crest and slope . . . . .	72
5.4.2	Ice crust region . . . . .	74
5.4.2.1	Salinity analysis . . . . .	77
5.5	Site 5: Sandstone Outcrop . . . . .	78
<b>6</b>	<b>Discussion</b> . . . . .	<b>80</b>
6.1	Decrease in Longyearbreen's thickness . . . . .	80
6.2	Near-surface ice at Innerhytta . . . . .	80
6.3	Ice Wedge Polygons . . . . .	81
6.3.1	Geomorphometric analysis . . . . .	81
6.3.2	Correlation between GPR reflections and ice wedge polygon features . . . . .	81
6.3.3	Estimation and Distribution of wedge ice . . . . .	82
6.4	Attenuation and Salinity at River Bed Pingo . . . . .	84

---

6.5 Geological structure of the Sandstone Outcrop . . . . .	84
6.6 Active Layer . . . . .	85
6.6.1 Estimation of the active layer thickness . . . . .	85
6.6.2 Shallow penetration with frozen active layer . . . . .	86
<b>7 Conclusions</b>	<b>87</b>
<b>8 Further work</b>	<b>88</b>
<b>A Appendix</b>	<b>94</b>
A.1 Preliminary Study . . . . .	94
A.1.1 Old Aurora Station . . . . .	94

# List of Figures

2.1	Svalbard, Central Spitsbergen and Adventdalen valley . . . . .	5
2.2	Geological map of Adventdalen Valley . . . . .	6
2.3	Thermal regimes in Adventdalen Valley (2005-2017) . . . . .	7
3.1	Permafrost thermal regime and layers . . . . .	8
3.2	Worldwide distribution of permafrost regions as of 2020 data . . . . .	9
3.3	Formation of an ice-wedge polygon . . . . .	14
3.4	. . . . .	15
3.5	Distribution of ice-wedge polygons in Adventdalen area, Svalbard . . . . .	16
3.6	Pingos in Adventdalen valley . . . . .	17
3.7	Formation of a pingo . . . . .	18
3.8	. . . . .	19
3.9	Comparison between a polygon pattern in Mars and on Earth . . . . .	21
3.10	Comparison between a pingo in Mars and on Earth . . . . .	21
3.11	Comparison between gullies and alluvial fan formations in Mars and on Earth . . . . .	22
3.12	Permafrost landforms found in different climate regions (from Earth and Mars) and corresponding location on the Martian subsurface . . . . .	23
4.1	Map of fieldwork campaign sites. Background image credit: © Norwegian Polar Institute/CC BY 4.0 . . . . .	24
4.2	Site 1 - Longyearbreen . . . . .	25
4.3	Site 2 - Innerhytta . . . . .	26
4.4	Site 3 - Ice wedge polygons and alluvial fan . . . . .	27
4.5	Site 4 - River Bed Pingo . . . . .	27
4.6	Site 5 - Sandstone Outcrop . . . . .	28
4.7	Definition of geometrical parameters of ice-wedge polygons . . . . .	30
4.8	Digitisation of ice-wedge polygons with GIS . . . . .	32
4.9	Diagram of ice-wedge polygons . . . . .	33
4.10	GPR system basic functioning . . . . .	34
4.11	Wave phenomena . . . . .	35
4.12	Definition of lateral and vertical resolution. . . . .	37
4.13	Antenna orientation . . . . .	40
4.14	PulseEKKO different configurations . . . . .	40
4.15	WISDOM antennas . . . . .	42
4.16	WISDOM prototype mobility configurations. Images credit: A.Le Gall, LATMOS. . . . .	43
4.17	WISDOM <i>FS2</i> mobility configurations. Images credit: W.S.Benedix, TU Dresden. . . . .	43

5.1	Snow-ice interface layer measurements by GPR and snow-probing . . . . .	45
5.2	Location and GPR profiles on Longyearbreen. . . . .	47
5.3	Ice Cave profile lines . . . . .	48
5.4	Ice Cave radargrams . . . . .	50
5.5	Profile lines at Innerhytta Pingo . . . . .	51
5.7	. . . . .	53
5.8	Loop profile targeting pingo features. . . . .	53
5.9	Profile line at Alluvial Fan . . . . .	54
5.10	GPR visualisation of deep snow accumulation . . . . .	54
5.11	Alluvial fan GPR profiles . . . . .	55
5.12	Ice wedge polygons at Site 3 . . . . .	56
5.13	Polygon 10 inside minimum bounding polygon. Background map: © Norwegian Polar Institute/CC BY 4.0 . . . . .	57
5.14	Correlation matrix of ice-wedge polygons geometrical parameters . . . . .	58
5.15	Profile lines at ice wedge polygons site. . . . .	60
5.16	Perpendicular lines over ice wedge polygons . . . . .	61
5.17	Profile lines by WISDOM units . . . . .	62
5.18	GPR grids . . . . .	63
5.19	Data processing diagram . . . . .	64
5.20	GPR depth slices . . . . .	66
5.21	3D rendered images . . . . .	66
5.22	Large grid depth slices . . . . .	67
5.23	Small grid depth slices . . . . .	68
5.24	trough buffer . . . . .	69
5.25	Ice Wedge coverage area for different thresholds . . . . .	71
5.26	Profile lines at River Bed Pingo . . . . .	72
5.27	Pingo crest and slope radargrams . . . . .	73
5.28	Ice crust radargrams . . . . .	75
5.29	Ice core drills . . . . .	76
5.30	Site 5, sandstone outcrop . . . . .	78
5.31	<i>Line 2</i> (pulseEKKO, config. 4). Processing: Dewow + Background Substraction + SEC2Gain	78
5.32	. . . . .	79
6.1	Ice Wedge width vs. depth . . . . .	83
6.2	Example of simple duplex structure (thrust fault) showing different stacking of thrust faults.	84
6.3	Sandstone fault . . . . .	85



# List of Tables

3.1	Recompilation of different patterned grounds and their formation phenomena . . . . .	12
4.1	Fieldwork campaign sites . . . . .	25
4.2	Permittivity, velocity propagation and attenuation through different media . . . . .	36
4.3	Acquisition parameters for different pulseEKKO configurations . . . . .	41
4.4	WISDOM nominal parameters . . . . .	42
5.1	Snow depth and travel times for WISDOM <i>prototype Line 4</i> (selected every 5 m) . . . . .	46
5.2	Axis values for polygon 10 applying different methods. . . . .	57
5.3	Geometrical and statistical parameters of ice-wedge polygons in Site 3. The second box corresponds to the values obtained in Ulrich, 2011 (Table 3.2) for region <i>AD 2</i> and third box is the relative error between each statistical parameter result (min., max., average) of this project using <i>AD 2</i> as reference . . . . .	59
5.4	Polygon network parameters . . . . .	69
5.5	WIV estimation on GIS . . . . .	70
5.6	WIV estimation according to GPR data, depth slice $z = 4\text{ m}$ . . . . .	70
5.7	In-situ measurements vs. GPR estimated values . . . . .	74
5.8	Salinity values of ice core samples . . . . .	77
A.1	Start and End positions for GPR measurements at Aurora station. . . . .	94
A.2	GPR acquisition parameters during Aurora station fieldwork . . . . .	94

# 1. Introduction

## 1.1 Background

### 1.1.1 State-of-the-art

GPR (Ground Penetrating Radar) is a commonly used geophysical tool for investigating glacial and periglacial geomorphologies. In combination with other monitoring methods, GPR has been extensively used in Svalbard glaciers to estimate ice-volume changes (eg. Lapazaran et al., 2013; Navarro et al., 2016), to better understand their thermal structure and drainage systems (Bælum and Benn, 2011), to investigate the origin of layered structures and location of reflectors (Berthling et al., 2000), etc. The work of Senger et al., 2014 within the framework of *UNIS CO<sub>2</sub> lab project* (in the Botneheia study area, close to Kapp Toscana, Svalbard) showed that GPR is capable to effectively indicate meaningful geological data while at the same time proving to be cost and time effective. In the recent surveys carried out by Janocha et al., 2021, GPR profiles are incorporated into a digital outcrop model of a paleokarst breccias system belonging to the rift basin of Billefjorden Trough (Svalbard). Their findings support the utilisation of GPR as a complement to 2D outcrops for strengthening and extending outcrop features interpretations.

Given the versatility and usefulness of GPRs, there is little wonder in why these instruments have also been used in ice-wedge polygons. Ice wedge-polygons are a subcategory of patterned ground that has attracted much attention since early explorers and scientists travelled to the Polar Regions due to their distinctive geometrical features (French, 2017). Since the 1960s there has been a continuous effort to understand how they originate and evolve, which processes affect their geometry and what they can tell us from the past changes in climate (eg. Lachenbruch, 1963, Mackay, 1980, Washburn, 1979). The current research on these Arctic landforms in Svalbard focuses on ice-wedge dynamics and how rapid cooling periods might affect the heave-thaw settlement as well as thermal expansion-contraction cycles which in turn cause cracking events (eg. Christiansen, 2005; Christiansen et al., 2016; Matsuoka et al., 2018) as well as the link between their properties and changes in hydrological, environmental and climatic characteristics (Oliva et al., 2014; Wales et al., 2020). Furthermore, ice-wedges of Axel Heiberg island (Canadian Arctic) have been even subject to astrobiology investigations with the aim to understand a subsurface ice environment as a suitable habitat for extraterrestrial life (Wilhelm et al., 2012). GPR surveys' principal goal on ice-wedge polygon landforms is to map the distribution of excess ice, often, being complemented by ground truth data from drillings and excavations, and remote sensing techniques. In May 1999, Hinkel et al., 2001 conducted a GPR survey on Barrow (Alaska) obtaining clearly visible subsurface hyperbolic reflectors corresponding to the ice wedges which, due to their ice-rich nature, allowed to trace the long-term position of the permafrost table. Further studies have taken place in Northern Canada such as Bode et al., 2007, where GPR and aerial photographs provided enough information to estimate the ice-wedge volume around a large area in relatively short time; or in Fortier and Allard, 2004 using GPR profiles as a tool for stratigraphic reconstruction of the polygons alongside sedimentological analysis, boreholes, radiocarbon data and cross sections. Similar studies investigating polygonal frozen ground have been carried out in Siberia (Schwamborn et al., 2006).

GPR surveys have evolved from 2D profiles to 3D grids, a novel technique that produces more precise images and reduces misinterpretation and ambiguity of traditional profiles. The method has been applied by Doolittle and Nelson, 2009 on relict cryogenetic macrostructures in USA's mid-latitude areas with the aim of delineating buried networks of sediment-filled wedges which proved the superiority of the 3D imaging over 2D GPR profiles. The latter resulting in indistinguishable or blurred features that often where imprecise, overlooked or simply misinterpreted. Other 3D GPR surveys include investigations of the subsurface structures of ice-wedge polygons and other features of active layer and near-surface permafrost close to Barrow, Alaska (Munroe et al., 2007). The recent study of Andres, 2020 in the Canadian High Arctic combines GPR surveys (2D and 3D), LiDAR (remote sensing) for periglacial mapping and sedimentology; not focusing only on Earth but transferring the knowledge acquired to a broader field of

planetary geomorphology. The only comparable studies carried out in Svalbard are Watanabe et al., 2013 and Ulrich, 2011. The first, targeting ice-wedge polygons in Kapp Linné via 2D and 3D GPR surveys and obtaining similar results as those in Canada: 3D GPR offers more reliable results. The latter, mapping polygons in Adventdalen valley and Martian mid-latitudes using remote sensing data for contrasting their shape and dimensions and discussing the genesis process in both planets.

### 1.1.2 ExoMars Mission

The European Space Agency (ESA) and the Roscosmos Space Corporation planned the mission ExoMars 2020, in which a lander and a rover are sent to Mars with the aim to determine if there has ever been life on Mars and to improve our understanding of the history of water on the planet (ESA, 2020). The launch has been delayed to October 2022 due to the necessity of performing more tests on the spacecraft with the definitive hardware and software, partly, caused by the general industry halt during the COVID-19 pandemic. The rover is expected to land on the red planet on the 10th of June of 2023 on Oxia Planum, a region located between 16° and 19° latitude North and -23° and -28° longitude East (Ciarletti et al., 2015) and particularly interesting for its wide clay-bearing plain (abundant presence of phyllosilicates) suggesting a diverse aqueous history (Quantin-Nataf et al., 2021).

The quest for exploring the Martian subsurface already starting since the first missions that considered the possibility of finding signs of life on Mars, the 1976 Viking Landers (Toulmin et al., 1977). Despite their failure to detect organic molecules, they planted a seed for future missions which materialised in the successful 1996 Mars Global Surveyor and the 2003 Mars Exploration Rovers (MER) demonstrating the existence in the past of wet environments on the red planet (Vago et al., 2017). Particularly, the presence of two main families of hydration altered products, sulphates and phyllosilicates (both found from *in-situ* samples and unambiguous remote sensing detections (Bibring et al., 2005)), are of major interest as their presence is associated with liquid water and water-related processes. In addition, the unexpected discovery of perchlorates ( $\text{ClO}_4^-$ ) by the 2007 *Phoenix* lander (Smith et al., 2009) and of oxygen ( $\text{O}_2$ ) released by thermal decomposition of oxychlorine species (Archer et al., 2016). The presence of perchlorates opens new possibilities for Mars investigations and even *in-situ* resources utilisation, as for example, ammonium perchlorates constitutes a powerful oxidizer that could be used as rocket fuel. In addition, the presence -or lack of- these chemical components might sheds some light into depositional processes in Mars, if dependent on the action of water as a transport agent or rather concentration agent (Vago et al., 2017).

If proof of life on Mars is ever to be found, in case it exists at all, most probably lays ca. 2 m below the subsurface where organic molecules can be well preserved and likely have escaped the long-term radiation and chemical damage caused by UV rays (Kminek and Bada, 2006). This is the reason the *Rosalind Franklin* Rover (ExoMars Rover) is equipped with a drill capable of reaching up to 2 m depth on hard formations (sedimentary rocks, evaporitic deposits) and a series of instruments that allow and accurate visual and spectral characterisation of the Martian surface to look for biosignatures. All these instruments constitute the *Pasteur* payload (ESA, 2020): *PanCam* (a panoramic camera to map digitally Martian terrain), *ISEM* (an infrared spectrometer to determine the mineralogical composition of the surface targets), *CLUPI* (a camera system to take high-resolution colour close-up images of rocks, drill samples, etc.), *WISDOM* (a ground-penetrating radar for characterising the stratigraphy of the Martian soil), *ADRON* (an active detector for gamma rays and neutrons with the aim of searching for subsurface water and hydrated minerals), *Ma\_MISS* (a multispectral imager for carrying out subsurface studies focusing on the Martian mineralogy and rock formation), *MicrOmega* (a visible and infrared imaging spectrometer for studying the mineralogy of Martian samples), *RLS* (a Raman Spectrometer to identify organic pigments and decipher the mineralogical composition) and *MOMA* (a Mars organic molecule analyser targeting biomarkers).

## 1.2 Master Thesis overview

### 1.2.1 Motivation

The driving force for starting this project was the existing connection between investigations on Earth's periglacial landforms and planetary science. Such unique environments on the Arctic can play a role as large-scale laboratories for testing instrumentation, exploring the combination of different techniques and analysing the system's performance in order to increase the chances of success for the coming missions in other worlds.

Interpretation of GPR soundings are by no means trivial. The last example is given by the latest dispute on the presence of liquid water below the martian polar caps. Back in 2018, a study by Orosei et al., 2018 analysed the Planum Australe region using MARSIS (Mars Advanced Radar for Subsurface and Ionosphere sounding), a low-frequency radar onboard ESA's Mars Express spacecraft. The retrieved radar profiles showed anomalous reflections, particularly displaying a bright subsurface in a well-defined 20-km wide area, and high relative dielectric permittivity (above 15). The authors interpreted the feature as a *stable body of liquid water on Mars*. Grima et al., 2022 has recently challenged this statement by proving that other existing volcanic-related terrains are able to produce very strong signals that could lead to a similar result of what is observed at the South polar cap of Mars. Furthermore, there are laboratory measurements that suggest clay, metallic inclusions or salt-rich ice could also produce the same strong signals.

Radargrams here on Earth do require from ground truth (eg. soil type, grain size distribution, moist content...) and an external context (eg. nearby geological formations, potential interactions with the environment...) for the correct interpretation of the data, and even when those are provided, some features can be misleading. The constraints in space exploration make data interpretation even more challenging. For this reason, experimental data from terrestrial regions -that might even represent the past geology of Mars- could fill current knowledge gaps in data analysis within the framework of planetary science.

### 1.2.2 Aims and Scope

The original project targeted only one site, Adventdalen's ice wedge polygons, with one GPR system, the pulseEKKO. However, this project has eventually taken place within the context of further tests and experimental validations of ExoMars GPR *WISDOM*, both flight spare model and prototype. The latter already having been tested in four different natural environments, two of them dry (the Atacama Desert in Chile and Mount Etna, in Italy) and the other two cold (a glacier in the Alps and the Dachstein ice caves in Austria) (Ciarletti et al., 2017).

Ice wedge polygons remained the focus as patterned ground is found on Mars and GPR investigations on this periglacial landform are rather scarce. Particularly, mapping (GPR slicing) the distribution of wedge ice would have only been done previously in Svalbard -to the best of knowledge- on Kapp Linné (Watanabe et al., 2013). In addition to these results, some *WISDOM* profiles have also been included.

Therefore, the aim of this Master Thesis is twofold:

- i Estimating the amount of wedge ice and its distribution according to GPR readings and compare it to GIS estimations
- ii Characterising target sites by providing GPR soundings and, when possible, ground truth data for the validation of *WISDOM*'s data processing and analysis tools

The first goal, being the main one, should address the following questions:

- How are ice wedge signatures featured in GPR soundings?
- Which polygon's geomorphometric characteristics, if any, correlate to wedge ice distribution?

- What are the differences between GIS and GPR wedge ice estimations?

The second goal focuses on the characterisation of each specific profile and questions apply on an individual basis depending on the available information:

- What type of features were identified in the profile?
- Which is the relative permittivity of the media and how was it obtained?
- Do the identified signatures fit with previous investigations or available data (eg. geological maps, drilling investigations, etc.)?

The findings of pulseEKKO will serve as reference for the future data processing of WISDOM profiles.

It is considered out-of-the-scope for this project the full wave-form inversion of the GPR profiles. Also, a detailed assessment of WISDOM's performance and an in-detail analysis of the data, such as the estimation of the shallow sub-surface dielectric constant.

### 1.2.3 Organisation

This master thesis is organised in the following sections:

- *Section 1*: provides a literature review of the state-of-the-art of GPR research and the ExoMars Mission.
- *Section 2*: describes the location, geomorphology, glacial history and climate of the study area (Adventdalen Region).
- *Section 3*: contains an overview of permafrost environments and periglacial landforms found in Adventdalen as well as a comparison with Mars analogous periglacial landforms.
- *Section 4*: gives a full description of the data and methods utilised to retrieve it. It includes the fieldwork campaign, the investigated sites, the GIS methods, an overview of the principles of GPRs and the different operating units.
- *Section 5*: provides the radargrams and their corresponding interpretation as well as the wedge ice mapping and volume estimation.
- *Section 6*: discusses the results of Section 5 and compares them with previous investigations when available.
- *Section 7*: synthesises the results and draws a conclusion
- *Section 8*: proposes improvements and new areas of study for future projects

*Section 1, 2, 3* and *4* either include passages or build up on the prelude of this work, *Geophysical Survey Methods on Central Spitsbergen*, a specialisation project (Course TBA4115) at NTNU.

## 2. Study Areas

### 2.1 Central Spitsbergen, Adventdalen Region

#### 2.1.1 Location and geomorphology

Spitsbergen is the largest island belonging to the Svalbard archipelago, in the Norwegian High-Arctic, located near the western margin of the Barents Sea Shelf and on the most northern side of the Atlantic ocean.

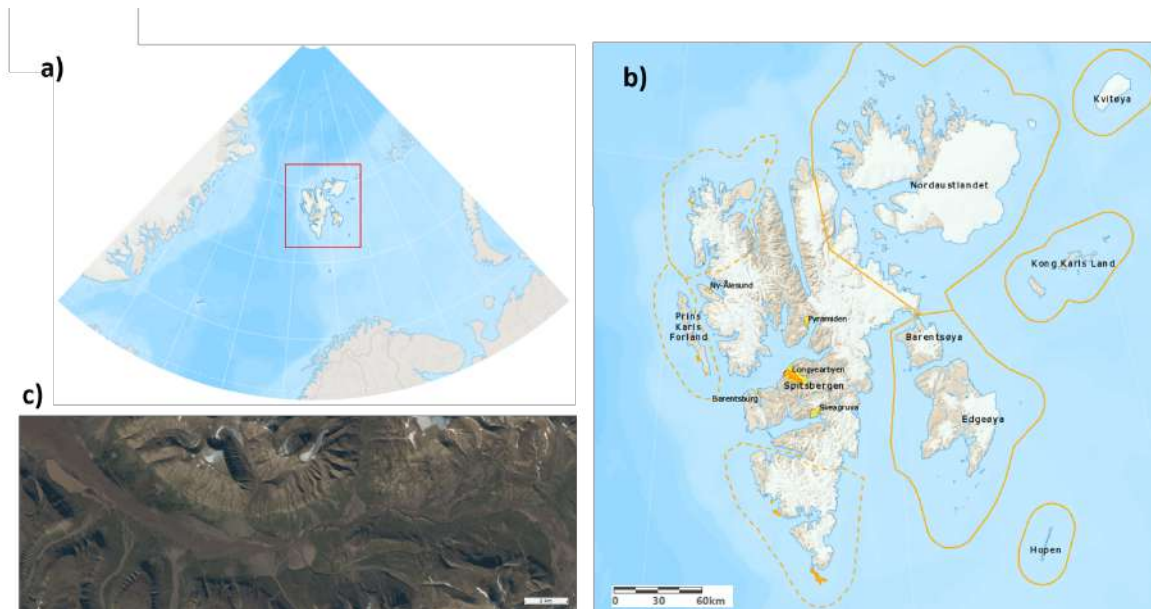


Figure 2.1: Svalbard, Central Spitsbergen and Adventdalen valley. a) Svalbard archipelago location. b) Map of Svalbard with most relevant locations and marked study area. c) Satellite image of Adventdalen Valley. Credit: © Norwegian Polar Institute/CC BY 4.0, Topographic map and Orthophoto

The main study area is Adventdalen, a U-shaped fjord-valley of 30 km length in Central Spitsbergen (78.2°N, 15.8°E). Its name is given by the valley-wide braided river system, Adventelva (Gilbert et al., 2018). The valley is covered by unconsolidated glacial, colluvial, alluvial and marine aeolian deposits from the Holocene (Oliva et al., 2014) and surrounded by 800-900 m high flat-top mountains and comprised of sedimentary rocks dating of Early Permian to Eocene (Matsuoka et al., 2018). While slopes of mainly Jurassic to Triassic deposits expose tertiary coal seams, most of the bedrock massifs belong to the Helvetiafjellet and Carolinefjellet formations (Major et al., 2001; Dallmann et al., 2001 as cited in Oliva et al., 2014). Tributary streams have built large alluvial fans along the sides of the valley in their way to drain the Adventelva river (Oliva et al., 2014). The lowest glaciofluvial terraces of the Adventelva river are covered by aeolian sediments in which a common patterned ground become ice-wedge polygon networks and pingos. The fluvial activity is seasonal, meaning that Adventelva river and its tributaries transport sediments and meltwater for a period of four months a year, starting on late May or Early June and are frozen during the winter (Gilbert et al., 2018).

Permafrost environments in Svalbard are laterally continuous and comprises at least 90% of the land surface which is not covered by glaciers (Christiansen et al., 2010). The thickness varies from around 200 m to 450 m in the surrounding mountains to thins towards the shore and the bottom of the valley

(Isaksen et al., 2000 as cited in Cable et al., 2018).

The active layer thickness is ca. 1 m in the valley bottom (Christiansen et al., 2010). When frozen, the frozen active layer and top permafrost are characterised by being rich in segregation ice, having a gravimetric water content about 50% and an excess in ice content of 15% (Cable et al., 2018).

### 2.1.2 Glacial history and permafrost formation

During the late Quaternary Svalbard was glaciated multiple times (Mangerud et al., 1998 as cited in Gilbert et al., 2019). The last glaciation reached its peak ca. 20 ka ago, referred as the Last Glacial Maximum, LGM, (Gilbert et al., 2019). During the LGM most of the sedimentary records from previous interglacial and glacial periods found on fjord and valleys disappeared. A period of deglaciation started ca. 15 ka prompting the sea levels to rise on the study region around 62-70 m above the present and to regress exponentially until the current sea level in the Late Holocene, ca. 5 ka (Lønne, 2008; Lønne et al., 2004 as cited in Gilbert et al., 2019).



Figure 2.2: Geological map of Adventdalen Valley. Dashed black line indicates the marine limit based on (Cable et al., 2018). Different colors stand for different geological formations. Credit: © Norwegian Polar Institute/CC BY 4.0, Geokart map

The formation of permafrost in Adventdalen commenced with fjord-fill reaching the sea level and the increasingly subaerial exposure due to the regression of the relative sea level (RSL) (Gilbert et al., 2018). This permafrost is classified as epigenetic<sup>1</sup> permafrost, characterised by being ice-poor. Its formation might be seen as strictly a Holocene phenomena (Gilbert et al., 2019). According to Jeppesen, 2001 Todalen's tributary valley permafrost is ca. 2.9 ka or older and the radiocarbon dating from nearby areas (Cable et al., 2018; Oliva et al., 2014) support the hypotheses of Holocene permafrost formation. Hence, epigenetic permafrost formed by downward freezing into the fjord-valley fill deposits (Gilbert et al., 2018). In contrast, syngenetic<sup>1</sup> permafrost is found on upper topographies of Adventalen and is characterised by being ice-rich and more ancient. This type of permafrost grew upward as a result of the accumulation of aeolian deposits on alluvial terraces. Permafrost found on the neighbouring mountain peaks has been dated from the Pleistocene (Cable et al., 2018).

### 2.1.3 Climate

The mean annual air temperature (MAAT) was  $-5.1^{\circ}\text{C}$  and annual precipitation 192 mm from 1990 to 2004 according to the meteorological station at Longyearbyen Airport (Matsuoka et al., 2018). It must be noted the non-negligible difference on annual precipitation depending on the source, for example, 400 mm of annual precipitation on the same monitoring station (Christiansen et al., 2010). Additionally, taking

<sup>1</sup>See Section 3.2.1.

into account that the shielding of the mountains might causes the station to actually underestimate the precipitation (Hanssen-Bauer et al., 1990). Regarding temperatures, it is also important to work with up-to-date data. During the period of 2005 to 2017 the MAAT rose to  $-2.6^{\circ}\text{C}$  (Matsuoka et al., 2018) and the trend of continuous warming does not seem to come to a halt.

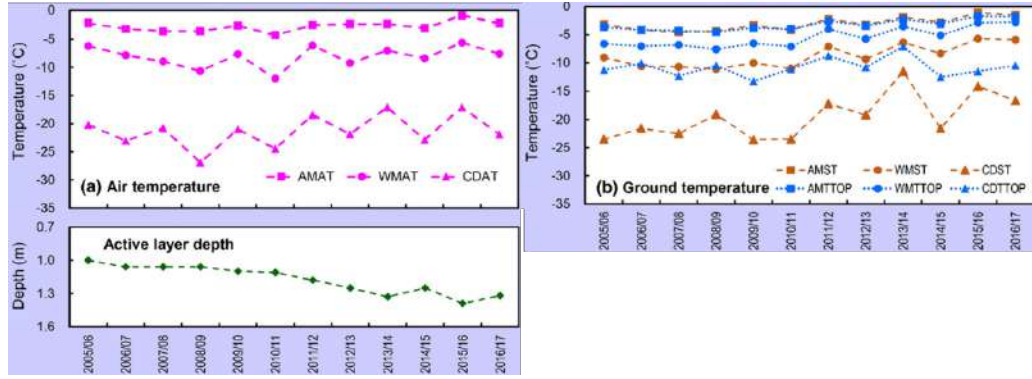


Figure 2.3: Thermal regimes in Adventdalen Valley (2005-2017). AM stands for annual mean, WM stands for winter mean, CD stands for coldest day, AT stands for air temperature, ST stands for surface temperature, TTOP stands for temperature at the top of permafrost. Image Credit: Norikazu Matsuoka/CC BY 4.0 from Matsuoka et al., 2018.

According to Matsuoka et al., 2018, in winter there are great air temperature fluctuations between  $0^{\circ}\text{C}$  to  $-20^{\circ}\text{C}$ , even as low as  $-30^{\circ}\text{C}$  (see Figure 2.3). Heavy, persistent winds sweep and erode the valley, keeping snow at a thin thickness and provoking an efficient cooling effect. In midwinter is possible that temperatures rise to positive values, causing snowmelt and in turn ground cooling with the formation of thin-ice covers. Summer, on the other hand, is characterised by fairly stable and positive temperatures (between  $5^{\circ}\text{C}$  to  $8^{\circ}\text{C}$ ) (Christiansen et al., 2013). The AMT on the permafrost have been registered by several boreholes and varied between  $-3^{\circ}\text{C}$  to  $-6^{\circ}\text{C}$  at a depth of 10m (Matsuoka et al., 2018).



### 3. Periglacial Landforms

"A periglacial landform is a feature resulting from the action of intense frost, often combined with the presence of permafrost. Periglacial landforms are restricted to areas that experience cold but essentially nonglacial climates."- (French, 2015)

#### 3.1 Introduction to permafrost environments

Permafrost is defined as a soil or rock that remains at or below 0°C for at least two consecutive years (Van Everdingen, 1998). Note that this does not necessarily imply permanently frozen but rather perennial (French, 2017). Indeed, the freezing point of water might be depressed several degrees below 0°C due to -most commonly- high salinity. As moisture of water can be present, a common way to classify permafrost according to ACGR, 1988 is either by the temperature (eg. thermal) or by the state (eg. frozen/cryotic, unfrozen/non-cryotic and *dry*; the latter referring to permafrost with very few ice content). Figure 3.1 presents the typical ground-thermal regime versus depth of permafrost (a) while showing the different divisions in the soil (b). The following concepts are key to describe a permafrost soil (modified from French, 2017 and Dobinski, 2011):

- **Permafrost table:** upper surface of the permafrost. Note on Figure 3.1 that the permafrost table includes seasonally active permafrost.
- **Active layer:** region above the permafrost table that seasonally freezes on winter. It is not considered permafrost but it is the responsible of the heat exchange between the lithosphere and the surface, which in turn, interacts with the atmosphere.
- **Supra-permafrost table:** ground above the permafrost table, commonly the active layer and supra-permafrost taliks.
- **Tálik:** unfrozen zone usually between the bottom of the seasonal frost and the permafrost table. Taliks might also exist on the top of the permafrost table (supra-permafrost talik) or inside the permafrost layer (intra-permafrost and closed taliks). See Figure 3.1.

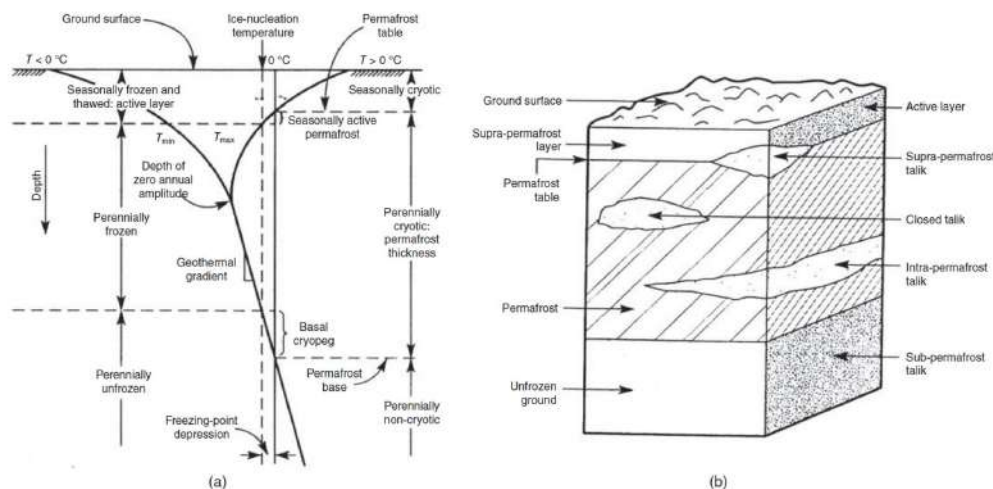


Figure 3.1: Permafrost diagrams. a) Presents the ground-thermal regime (temperature vs. depth) indicating maximum and minimum temperatures, zero annual amplitude depth and marks on the seasonal thaw. b) Schematic representation of the different layers of permafrost. Image source: French, 2017.

Permafrost's distribution is mostly caused by climate but other factors may affect its appearance to a local level. According to French, 2017 these include the relief and slope orientation (which influence the amount of solar radiation or accumulation of snow), the type of soil and rock in the region (altering albedo, thermal conductivity), vegetation (its presence affects directly on the ground thermal regime and protects the soil from incident radiation), snow coverage (snow acts as thermal insulator as well as protects from the sunlight) and fire (common in boreal forests due to lightning strikes during storms; the speed of the fire might cause considerable changes on the permafrost) and the presence of lakes and surface water bodies (water is known for its high volumetric heat capacity, creating natural heat storages).

The spatial extent of permafrost can be divided in three main categories (Dobinski, 2011): *altitudinal permafrost* (in which occurrence is on mountainous regions at high elevation), *latitudinal permafrost* (permafrost of the polar regions) and *plateau permafrost* (in areas of high elevation, of Central Asia). There are two other, less common, permafrost categories that bear no relation to the current climatic conditions which are *sub-sea permafrost* (eg. on the continental shelf of Beaufort Seas) and *relict permafrost* (French, 2017). Latitudinal permafrost constitutes the 39.4% of the northern hemisphere land surface (Dobinski, 2011). If the frozen ground regions are separated by areas of unfrozen ground it is referred as *discontinuous permafrost* (if the spatial extent is less than 50% then it is *sporadic permafrost* and below 10% *isolated permafrost*), whereas a total uninterrupted of frozen ground (with exception of water bodies) is known as *continuous permafrost* (French, 2017). The boundary between sporadic and continuous occurs as far south as 50°N and 60°N to the northeast of Lake Baikal (Russia) and even 50°N to the north of Mongolia, while it starts around 55°N in North America (Zhang et al., 1999). According to Figure 3.2 the permafrost found in Svalbard Archipelago is mostly continuous permafrost.

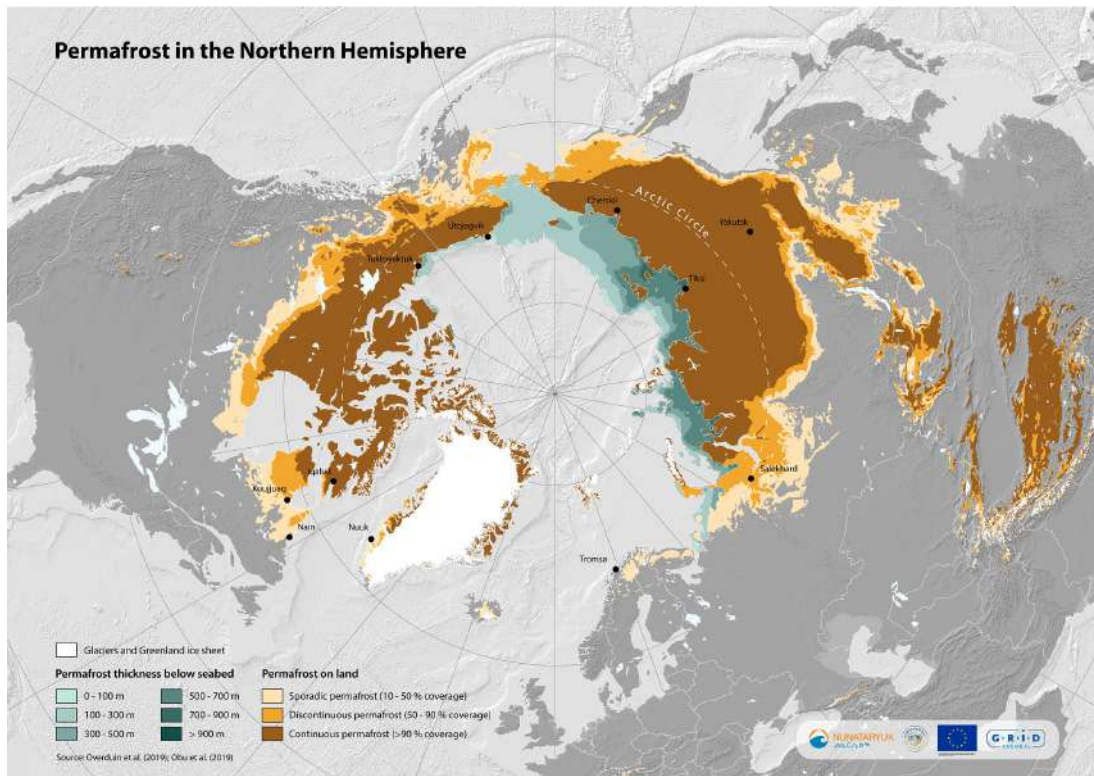


Figure 3.2: Worldwide distribution of permafrost regions as of 2020 data. Map courtesy of GRID-Arendal produced as part of *Nunataryuk*, an EU-funded Horizon 2020 project focused on permafrost coastlines in the Arctic. Image Credit: Georgios Fylakis (GIS expert)/CC BY-NC-SA 2.0/link: [www.grida.no/resources/13519](http://www.grida.no/resources/13519)

## 3.2 Patterned ground

Patterned ground phenomena is a manifestation in the relief of a series of processes of polygenetic origin (thermal-physical, physico-chemical, mechanical) that result in characteristic topographic morphologies, namely, *polygons*, *circles*, *stripes* and *steps* or (solifluction) *lobes* (Yershov, 2004). These geometries might appear isolated but most of the time they interact with each other and form a resulting pattern, called *net*. Patterned-ground features can be divided into two categories: sorted or unsorted. The criteria for this classification is in regards of the material distribution forming the geomorphology, mostly, the transport and uneven accumulation of fine sediments and coarse ones (French, 2017). In Table 3.1 is presented an overview of the different geometric patterns alongside their respective formation process based on the descriptions of periglacial environments in French, 2017. It must be noted that the classification given is, by no means, unique and other authors arrange the categories differently (eg. Andres et al., 2020; Ulrich, 2011; Yershov, 2004).

As aforementioned, the genesis phenomena for patterned ground features is very diverse and not fully comprehended. Polygon patterns are the result of thermal-contraction-cracks which form in response to volumetric tensions associated to temperature changes of the ground (Yershov, 2004). After the cracking process in winter the fissures might be filled by sand driven by strong winds or by snow-melt water (see Table 3.1 and Section 3.2.1 for a in-depth description of ice-wedges). The geometry of the polygon itself, dimensions and orthogonality<sup>1</sup> vary according to the vertical temperature gradient with depth, distance from another fracture, the modulus of elasticity during shear, the coefficient of thermal expansion of the ground, time at which the processes take place, etc (Christiansen et al., 2016; Yershov, 2004). The greater the temperature variation, the smaller is the distance between fractures, hence, smaller the polygons: under drastic deep freezing conditions the frost fissures are spaced from 0.5-2 m to 10-12 m; in less extreme continental climate polygon cracks are spaced ranging from 20-40 m to 50-80 m (Yershov, 2004). The very nature of the networks formed and their pattern complexity (orthogonality) relies on the composition of the soil (mechanical properties) as well as its heterogeneity where materials with similar properties (homogeneous) result in rectangular-prone nets. Furthermore, a polygon might display secondary and even tertiary fissures in its network as mechanism to relieve thermal stress when the main cracks (primary fissures) are prevented from cracking owing to snow accumulation (French, 2017). All things considered, the average diameters of terrestrial thermal contraction polygons range from a few meters to a few tenths of meters (Frederick et al., 2016).

Circles originate during cryoturbation processes. The term *cryoturbation* is an umbrella term referring to all soil movements caused by frost action (necessarily implying a water-ice phase change) such as heave, thaw, settlement, thermal contraction and expansion, and growth and disappearance of ice-segregated bodies (ACGR, 1988). In particular for the formation of circles, frost heaving and sorting are thought to have a high impact in this fine-grained, frost-susceptible soils (Yershov, 2004). An equilibrium model based on thermally-induced soil circulation was proposed by Mackay, 1990 in which the upward displacement of material is caused by the freezing and thawing of the ice lenses at the top and bottom of the ice layer, creating a cell-like, gravity-induced motion. Yet, the model has limitations to explain the origin of some circular forms (French, 2017). Both circle and polygon features mostly occur in flat or nearly-flat surfaces but as slope angle increases, the patterns become elongated and irregular, to the point of morphing to a new pattern: stripes (French, 2017). These microrelief topographies are the result of cryoturbation processes dominated by gravity. Surface wash (seepage) has a preference for removing fines, hence, leaving coarser material and even boulders and stones accumulated on the edges of the lines of movement.

Solifluction lobes are also a type of feature resulting from the action of gravity in cryoturbation processes. *Solifluction* describes a viscoplastic flow of granular materials and loose deposits on slopes, (Yershov, 2004). The term *gelifluction* might be used to describe a solifluction process in frozen-ground conditions which is restricted to the active layer region and is associated exclusively to the thaw period (Washburn, 1979). In essence, solifluction lobes originate in slopes of fine silty clays and silty sands with



<sup>1</sup>Classified by French, 2017 into 90° intersection, 120° intersection or random

high content of rudaceous<sup>2</sup> material where downward percolation of water is limited by frozen ground and where melted ice provides excess water that reduces the cohesion of the soil (French, 2017; Yershov, 2004). The viscoplastic displacement of the soil takes place at different rates and deposits in laminates (lobes).

---



<sup>2</sup>Sedimentary rock formed by mostly fragments coarser than sand grains.

Table 3.1: Recompilation of different patterned grounds and their formation phenomena based on the descriptions of periglacial environments in French, 2017

Geometric Pattern	Landform Image	Types	Description	Genesis phenomena	Formation Process
Polygon		Ice-wedge	Wedge-shaped bodies of ice formed by foliated or vertically-banded ice	Thermal contraction and water infilling	During winter the soil contracts due to low temperatures and cracks develop. In spring the water from melting snow penetrates the crack and creates (or feeds) an ice wedge.
		Sand-wedge	Wedge-shaped bodies with a mineral infill (from loess to medium/-coarse sand)	Thermal contraction and wind-driven infilling	A thermal-contraction-crack is filled with wind-blown sediment in a region of absent moisture
		Pseudomorph wedge	Wedge-shaped bodies with a secondary infilling material different from the material that originally formed the structure	Thermal contraction; thermokarst (for ice-wedge pseudo-morphs)	There are two categories: Ice-wedge pseudomorphs in which the secondary mineral infilling resulted from the thermokarst phenomena (melting of excess ice). Composite wedges present both ice and clastic sediments in variable proportions, but do not contain excess ice, the resulting infilling is caused by both thawing and wind.
Circle		Plug circle	Non-sorted circle in which the center feature remains flat	Cryoturbation	Combination of ice-induced soil movements that result in the segregation of particles by their size
		Hummock	Non-sorted circle with central feature adopting a raised topography. If the circle is completely bare is named <i>mud hummock</i> , if it presents vegetation as <i>earth hummock</i> .		
		Mud boil	Extrusion features of poorly sorted sediments with high silt/clay content	Cryoturbation (high hydraulic potentials)	There are two mechanisms: after summer rain, water confined between the underlying permafrost develops artesian-induced pressures and causes the extrusion feature. The high hydraulic potential is derived from desiccation and hardening of the surface in late summer resulting in water confined below the overlying semi-rigid carapace.

Continued on next page

Table 3.1 – *Continued from previous page*

Geometric Pattern	Landform Image	Types	Description	Genesis phenomena	Formation Process
Stripe	 <sup>5</sup>	-	Parallel lines with their axis aligned to the line of movement. They can be sorted or unsorted. The former shows a marked differentiation between lines of coarser and finer material oriented parallel to the gradient.	Cryoturbation dominated by gravity	Most probably the action of several phenomena involving: sliding, rolling, snowmelt erosion and surface wash.
Solifluction lobe	 <sup>6</sup>	-	Viscoplastic slow flow of loose deposits typical of silty clays and silty sands. It creates a micro-relief landforms (lobes) originating from the different rates of displacement of the heterogeneous material.	Cryoturbation dominated by gravity	Caused by its own weight the loose deposit is driven down-slope while causing plastic deformations on the ground. The rate of solifluction is a function of slope steepness, depth of the thawing, composition of deposits, etc.

<sup>3</sup>Ice-wedge polygons in Adventdalen, Svalbard. Image from Christiansen et al., 2016

<sup>4</sup>Sorted circles in Kvadehuksletta, Svalbard. Image from <https://mapio.net/pic/p-1538325/>.

<sup>5</sup>Stripes in Murchisonfjorden area of Nordaustlandet, Svalbard. Image Credit: © Glaciers online

<sup>6</sup>Solifluction lobes in Dracoisen, Ny Friesland, Svalbard. Image Credit: © Glaciers online

### 3.2.1 Ice wedge polygons

Ice wedge polygons are the one of the most featured landform in permafrost Arctic lowlands and they constitute the most prevalent type of ice in the most superficial layers of permafrost, ca. 2-3 m (Christiansen et al., 2016; Frederick et al., 2016; Wales et al., 2020). The ice wedges are wedge-shaped bodies of ice formed by vertically-banded or foliated ice (vein ice) that developed after a thermal contraction-cracked opened in winter and was filled by water from melting snow that penetrating during spring (French, 2017) (See Figure 3.3).

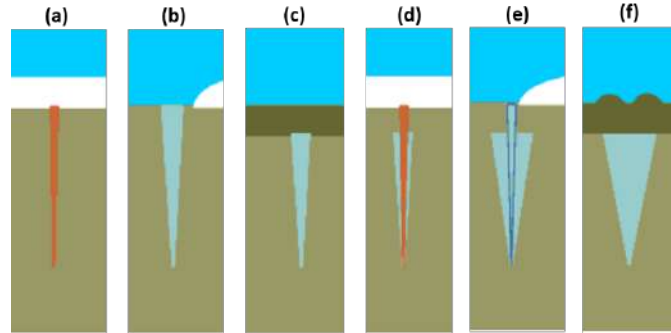
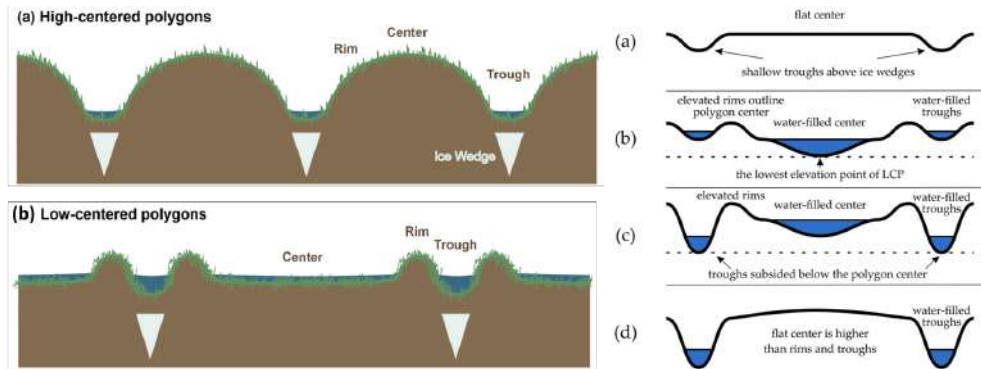


Figure 3.3: Formation of an ice-wedge polygon. a) The winter cold causes the soil to shrink and cracks. b) During spring, in warm days the water drains into the cracks and then freezes inside forming an ice wedge. c) In summer the active layer and top of the ice wedge melts. d) The following winter the crack is opened again. e) On the next spring additional water enters the crack and feeds the ice wedge. f) The soil above the ice wedge is pushed up forming ridges, creating a polygon pattern on the surface. Image modified from: U.S. Fish and Wildlife Service, [USFW](#).

Ice wedges can be classified according to their growth direction and growth sequence. The former distinguishes between three different categories: epigenetic, syngenetic and anti-syngenetic (Mackay, 1990). In *epigenetic* wedges ice forms in pre-existing permafrost (being younger than the surrounding sediment) and grows laterally, so progressively the ice wedge becomes wider but not deeper, as a product of cyclical cracking and infilling. *Syngenetic* wedges grow upwards owing to surface aggradation, that is to say, as sediments accumulate and the ground surface rises also the ice wedge does. Hence, these ice wedges form simultaneously as the host sediment. According to Ulrich et al., 2014 epigenetic ice-wedges found in thermokarst basins are characterised by a V-shape (inverted isosceles triangle) while syngenetic ice-wedges rather resemble an inverted trapezoid with only a slight narrowing of its width as depth increases. *Anti-syngenetic* ice wedges are characterised for their veins penetrating to greater depths with time. If surface lowers (eg. erosion) the active layer drops leading to thaw of the top part of the ice wedge (French, 2017). The growth sequence establishes a classification of the wedges by their age, from oldest (*primary* wedge) to youngest (*terciary* wedge), having *secondary wedges* as intermediate stage.

In turn, the growth sequence is determined by the corresponding geomorphology displayed by the ice-wedge polygons. The characteristics of relevance of the polygons aside from their size are the centers, rims and troughs which describe their microtopography (Wales et al., 2020). According to these characteristics one can classify polygons in two main categories: *low-centered* polygons and *high-centered* polygons. Before forming low-centered polygons and still while the ice wedges are growing, the polygons experience two other stages referred as *incipient polygon* and *fen polygon* in which the terrain barely hints the presence of the ice wedges (French, 2017). Once sufficient ice wedge growth is reached, polygons have delineated raised rims as a result from the thermal expansion and lateral displacements of the active-layer above the growing ice, giving birth to low-centered polygons (French, 2017; Mackay, 1980). Progressively, the troughs become deeper due to thermokarst processes (intermediate-centred polygon) until the flat center is higher than the rims and troughs (See Figure.3.4(b)). These processes of degradation lead to the formation of high-centered polygons. The ground above the wedges has subsided and the polygon outlining troughs

have enlarged and deepened, causing an inverted topography (Wales et al., 2020).



(a) Polygon types. Image Credit: Lydia J. S. Vaughn and Margaret S. Torn/CC BY 4.0 from Vaughn and Torn, 2018.

(b) Transition from low to high-centered polygon. Image Credit: Andrei Kartoziia/CC BY 4.0 from Kartoziia, 2019.

Figure 3.4

### 3.2.1.1 Adventdalen polygons

In the region of interest of this project, Adventdalen valley, ice wedge-polygons are common from sea level to altitudes of more than 500 m above the sea level (Sørbel and Tolgensbakk, 2002). According to Sørbel and Tolgensbakk, 2002, polygons occur both on flat terrain and inclined slopes (up to 25°). Most flat regions correspond to lower areas of valley bottoms where polygons are located in glaciofluvial sediments. In contrast, those on higher altitudes (250 m and above) occur in weathering material lying on Cretaceous bedrock. Polygons closer to the sea level are thought to be younger than their higher-altitude counterparts, reaching back to the Weichselian Period<sup>7</sup> (Sørbel and Tolgensbakk, 2002). According to Cable et al., 2018 evidence supports a polygenetic formation of Adventdalen's valley permafrost as well as variations of the cryostructure subjected to the landform, topography and local drainage conditions. Saline permafrost (regions closer to the coast) originated when the sea-level drop in mid-Holocene, causing an accelerated epigenetic freezing after the exposure of terraces above the water level. In contrast, near-surface non-saline permafrost (eg. eluvial deposits, solifluction slopes) indicates shifts in the ice microstructure correlating with late Holocene variations between syngenetic and quasi-syngenetic permafrost aggradation.

The investigations from Matsuoka et al., 2018 on an alluvial fan fed by Todalen valley and from Ulrich, 2011 in different locations across Adventdalen (See Figure 3.5), are key to understand the different polygon networks found in the valley. The study site of Matsuoka et al., 2018, respectively labelled as AD1 site in Ulrich, 2011 study, corresponds to an ice-wedge polygon formation in the convergence of Adventelva river and an inactive alluvial fan originating from Todalen valley at approximately 10 m a.s.l (site A in Figure 3.5). This site is characterised by fine-grained eolian sediment of ca. 2-3 m depth over silty-sand, silty-clay gravelly sediments of fluvial origin (Matsuoka et al., 2018). The site is characterised by low-centered polygons that form most commonly quadrangles, pentagons and hexagons of an average diameter size of 20 m, ranging from minimum ca. 8 m to a maximum of 51 m (Matsuoka et al., 2018; Ulrich, 2011). Both authors describe the polygons as delimited by relatively shallow (10-40 cm deep) and narrow (20 cm to 100 cm) troughs and slightly raised rims. The largest polygons show cracks forming secondary and tertiary polygons with smaller troughs and no ridges. Different drilling and geophysical investigations have shown that ice wedges are found below the troughs underneath the active layer (ca. 0.8 m-1 m) and that the width of the through (ca. 0.5-3 m) is the minimum of the width of the ice wedge (Matsuoka et al., 2018; Watanabe et al., 2008). According to Matsuoka et al., 2018 the geomorphology of

<sup>7</sup>Division of late Pleistocene deposits in Western Europe.



the polygons changes as altitude increases, diminishing their size (diameters below 3 m) and transforming to other patterns such as earth hummocks and mudboils.

Sites *B*, *C* and *D* corresponding to Ulrich, 2011 *AD2*, *AD3* and *AD4* respectively (See Figure 3.5) belong to the high-centered polygon type and are found between ca. 80 m and 170 m a.s.l. *B* and *C* are located in terraced slopes in which polygons decrease in size with steeper terrain. The troughs in *B* are smaller and shallower than the neighbouring investigated sites, with average values of 1.4 m (width) and 0.5 m (depth) and peak values of 4.2 m and more than 1 m respectively. Those in *C* present similar peak values but display considerably bigger troughs with a minimum width of 2.3 m and greater depths (between 0.3 m and more than 1 m) as troughs merge with drainage fluvial channels. Polygons in site *D* present the maximum width recorded ranging from 2.9 m to 7.5 m and depths above 1 m. The reader is referred to Ulrich, 2011 Table 3.3 and Table 3.4 for an overview of the polygon's geometrical characteristics.

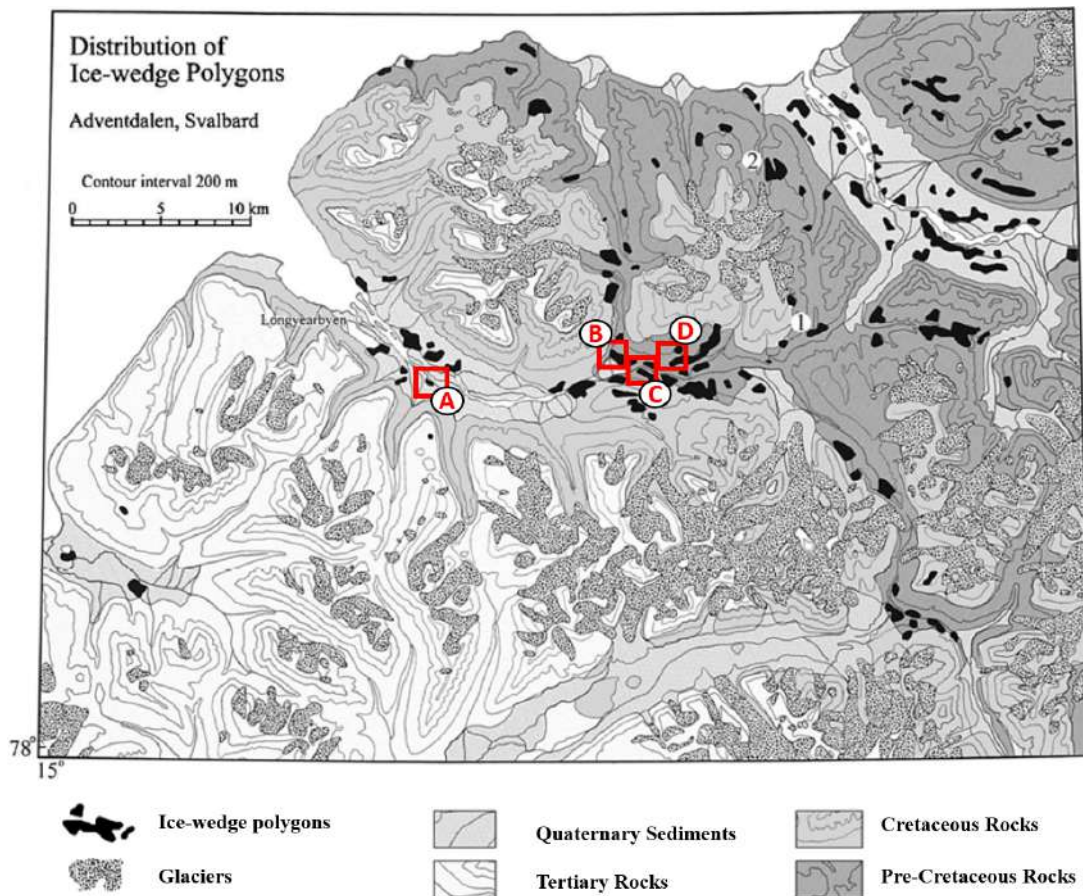


Figure 3.5: Distribution of ice-wedge polygons in Adventdalen area, Svalbard. Location *A* corresponds to the investigation site in Matsuoka et al., 2018 and *AD1* in Ulrich, 2011. Locations *B*, *C* and *D* correspond to *AD2*, *AD3* and *AD4* in Ulrich, 2011. Image modified from Sørbel and Tolgensbakk, 2002.

### 3.3 Pingos

Pingos are ice-cored hills which have a massive ice core and rise around 3 to 70 m height with a diameter of 30 to 300 m wide, mostly with a circular shape (French, 2017). They are periglacial morphologies that belong almost exclusively to high arctic conditions with continuous permafrost, even though they are not particularly common features of the arctic landscape (Seppälä, 1982 as cited by French, 2017). There

are two different types of pingo depending on their genesis: *closed-system* pingos and *open-system* pingos (Hornum et al., 2020). Closed-system pingos are created after permafrost aggradation in water-saturated rich in sandy sediments expulses the pore water (Mackay, 1998). As permafrost advances deeper into the soil, water in the pore spaces freezes, expanding during the process. However, while this is true for shallow depths, the deeper the soil the more the lithostatic pressure which is preventing the ground to heave (to either settle or swell) and instead, the ice expansion prompts an overpressure which in turn increases the piezometric level of groundwater. This groundwater is enclosed by the permafrost until can be expelled to the surface through unfrozen parts of the soil (Hornum et al., 2020) (See Figure 3.7). Closed-system pingos are typically found in shallow lakes or ancient lake beds, usually originating as single landforms and not in groups (French, 2017).

On the other hand, the open-system pingos are formed by intra- or sub-permafrost groundwater flow that is not trapped by the permafrost and that by artesian<sup>8</sup> pressure eventually reaches the surface (Liestøl, 1977 as cited by French, 2017). According to French, 2017 the presence of open-system pingos is associated with elements with relief such as hill slopes, alluvial fans or valley bottoms, where groundwater seepage from sub-glacier meltwater provides large hydraulic heads. It is important to note that pingos are not particularly well-documented due to the inaccessibility to sub-permafrost groundwater systems and hydrogeological mechanisms in permafrost environments today not fully understood (Hornum et al., 2020).

On Svalbard, the most prominent pingos are linked to either geological faults or high artesian pressures continuously fed by subglacial melt-ice from the warm-based glaciers (Liestøl, 1977 as cited by French, 2017). As Figure 3.6 shows, a set of five open-system pingos are found in Adventdalen, parallel to the valley axis (Hornum et al., 2003). Yoshikawa, 1993 reports that the pingos located in the north-eastern side of the valley (Lagoon, Longyear and Førstehytte) formed during Quaternary marine muds and near to the boundary with the sedimentary bedrock. The remaining two (Innerhytte and River pingos), further inland, formed in shales just lying above a fault situated in the vicinity of Adventelva.



Figure 3.6: Pingos in Adventdalen valley. The dashed line marks the marine limit, the pingo locations are represented by green and yellow circles: LP: Lagoon Pingo; LYRP: Longyear Pingo; FHP: Førstehytte Pingo; IHP: Innerhytte Pingo; and RP: River Pingo. Image Credit (background image): © Norwegian Polar Institute/CC BY 4.0. Pingo sites from Hornum et al., 2020

<sup>8</sup>Water trapped between layers of poorly permeable soils, confined under pressure. See <https://www.usgs.gov/>

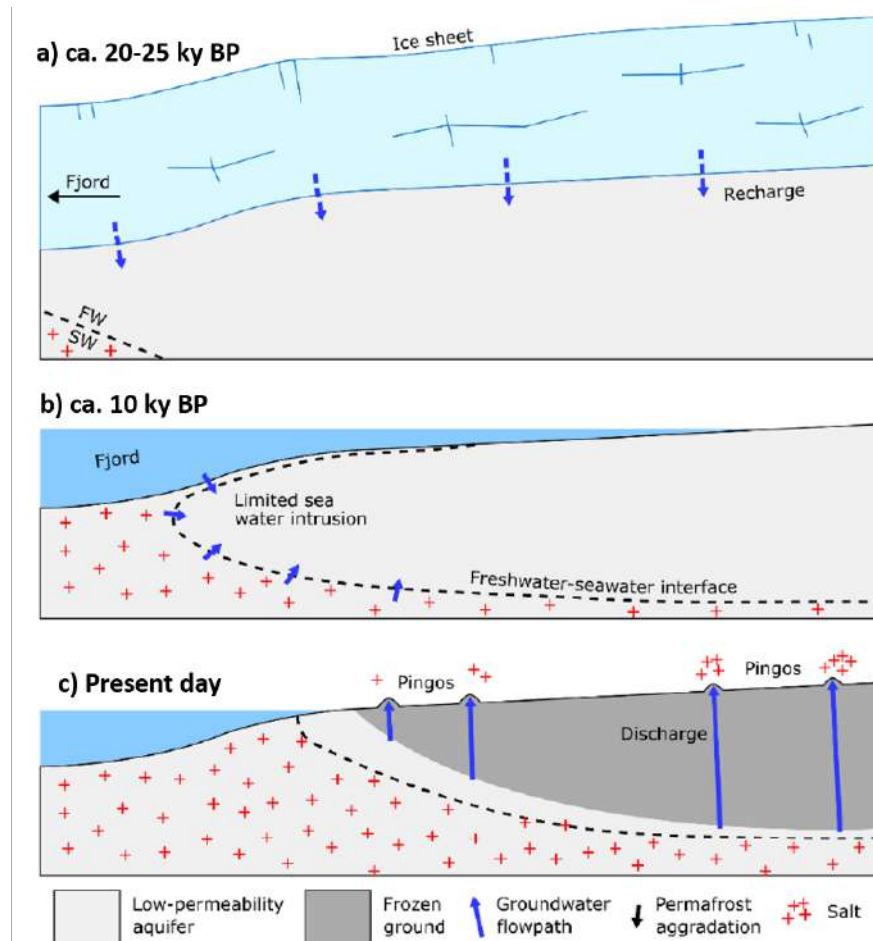


Figure 3.7: Formation of a pingo. a) The subglacial melting of the ice sheet recharges the groundwater system with freshwater. b) Low-permeability rocks limit seawater infiltration and allow freshwater body to persist. c) Permafrost advances with depth and confined groundwater is expelled to the surface. Image Credit: Mikkel Toft Hornum/CC BY 4.0 from Hornum et al., 2020.

## 3.4 Other periglacial landforms

### 3.4.1 Alluvial fan

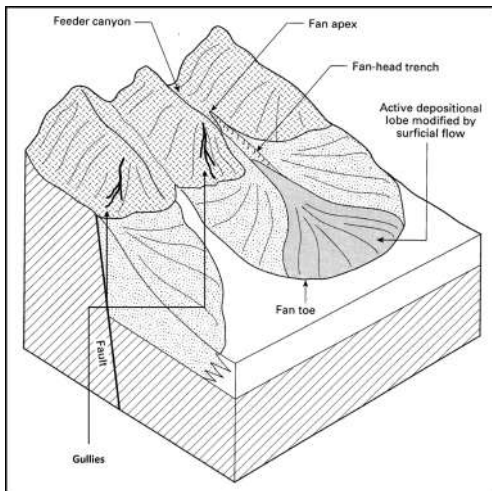
An alluvial fan is large deposit of sediment with the characteristic shape of a fan on which a braided stream flows over (Pidwirny, 2006). Its genesis derives from the accumulation of sediments derived from fluvial (Catto, 1993) and sheet flood<sup>9</sup> processes (alluvium). In a simplified way, the streams that descend down the mountain carry with them heavy loads (stones, pebbles, and coarse grained sands) and as their velocity reduces due to the horizontal terrain, they deposit the sediments (Pidwirny, 2006). However, alluvial fans represent a continuum of depositional processes and particularly for paraglacial<sup>10</sup> zones, on small debris cones where debris-flow processes concentrate flows (Harvey et al., 2005). The fan features seem to be strongly correlated to sediment supply and flood regime, but not so strongly to differences in environments (arctic vs. subtropical).

<sup>9</sup>Flat area with low slope and not well defined washes that can contain the water.

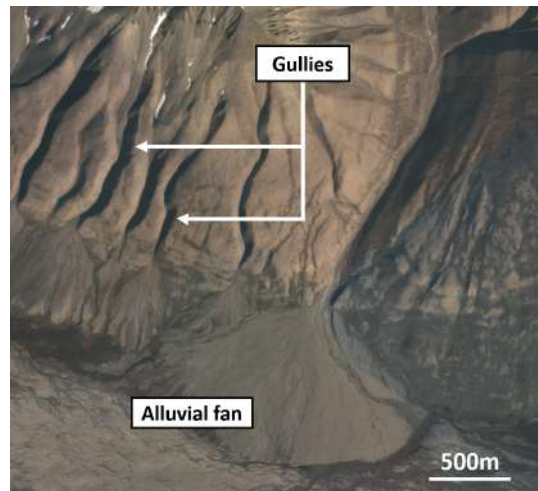
<sup>10</sup>Transitional landform, not defined by glaciers nor cold-climate processes. See Slaymaker, 2009 for extensive discussion on the term.

### 3.4.2 Gullies

Gullies are steep-sided eroding water courses that are caused during rainstorms due to ephemeral abundant floods (Bocco, 1991; Morgan, 1980). These features develop when a geomorphic threshold is transgressed (Bocco, 1991; Patton and Schumm, 1975), for example, because of the loss of resistance of the materials and/or an increase of the erosion of the runoff. Gullies resulting from thermal erosion (meltwater eroding permafrost) are often characterised by an inverted "T" cross profile as water erodes first vertically more aggressively and then on the lateral direction, as the bed is reinforced by the deposited sediments (French, 2017). Gullies might also be formed in the absence of water but -at least on Earth- they can only generate small gully-like features which are not comparable with water driven erosion (Sidorchuk and Matveeva, 2020).



(a) Diagram of alluvial fan including gullies. Image Credit: Marli Bryant Miller, Department of Earth Sciences, University Of Oregon (Eugene, Oregon, USA). Source: [seddepseq.co.uk](http://seddepseq.co.uk)



(b) Close-up on gullies and alluvial fan on the valley side of Adventdalen. The alluvial fan is fed on Adventelva river by tributary valley Koslådalen. Credit: © Norwegian Polar Institute/CC BY 4.0, Ortophoto) map

Figure 3.8

## 3.5 Mars analogous periglacial landforms

Periglacial geomorphologies found on Spitsbergen (Svalbard, Norway) are similar to those on Mars, suggesting a possible relation with past and/or present existence of ice near or at the subsurface of the red planet (Hauber et al., 2011). Martian permafrost landforms include gullies, thermal-contraction crack polygons and latitude-dependent mantle (LDM) formed more recently than c. 5 Ma. Other landforms seem to indicate the preservation of near-surface ice (such as pedestal craters) with latitude-dependent differences (Hauber et al., 2011).

But, is the Martian permafrost terrain similar to that found on Earth? According to (Laskar et al., 2002) the Martian surface and shallow subsurface have experienced mean annual temperatures below 273 K (0°C), usually decreasing to 220 K or more (Mellon and Jakosky, 1993 as cited by Levy et al., 2011). Hence, the Martian subsurface lacks a wet active layer and most likely, for the last 5 to 10 Ma the planet has not experienced favourable climate conditions for a widespread development of its wet active layer (Kreslavsky et al., 2008). Ground ice is thought to be only stable at higher latitudes (Hauber et al., 2011) as supported by the evidence provided by the *Phoenix* lander (Smith et al., 2009) (See also the distribution of most relevant periglacial landforms on the Martian surface on Figure 3.12.b). The latitude ranges in which Mars ground ice is stable turns out to be a correlation to the planet's tilt on its rotational axis (obliquity) (Hauber et al., 2011). It seems that water ice has been cyclically driven from the poles to lower latitudes during periods of higher obliquities when the polar regions were exposed to increasing solar energy. Conversely, the water ice was again redistributed to higher latitudes following periods of lower obliquities (Levrard et al., 2004). In addition, the presence of recently discovered hydrated minerals suggests the past presence of liquid water and water-related process on Mars (Poulet et al., 2005). In particular, two main families of hydration altered products are of interest, sulphates and phyllosilicates. The latter being previously suggested based on *in situ* elemental analysis of the Viking Landers (Toulmin et al., 1977) and from current unambiguous remote sensing detections (Bibring et al., 2005). Therefore, ground ice is expected to be a significant factor on Martian landscape evolution and present in even mid to low-latitude regions (Hauber et al., 2011).

As shown on Figure 3.12.a polar regions might play a role as geomorphological analogues of Mars. In particular, Spitsbergen (the largest island of Svalbard archipelago) displays a great variety of periglacial landforms in a relatively small area and close to the settlements of Longyearbyen and Ny Ålesund (Hauber et al., 2011): pingos, ice-wedge polygons, gullies, alluvial fans, rock glaciers (as seen in Sections 3.2.1, 3.3 and 3.4).

### *Polygon patterns*

The criteria to investigate Mars patterned ground is mirroring that on Earth, based on the network features, the microtopography of the polygon, its size (diameter), its correlation to specific latitudes (see Figure 3.12.b) and particular slope orientations, the surface age (mostly occurring in young areas), bedrock presence (most of polygon patterns taking place in unconsolidated sedimentary units), affinity with other landforms (suggesting periglacial processes on the region) and albedo (Levy et al., 2011). Research carried out by Levy et al., 2011; Levy et al., 2009 clearly shows that Martian polygons are mostly high-centered with depressed boundary troughs and flat interiors. The presence of low-centered polygons is more scarce and the lack of other surrounding landforms with the impossibility of a recent active-layer leads to think they are not ice-wedge polygons, rather sand-wedge polygons or sublimation polygons (Dundas and McEwen, 2010; Lefort et al., 2009).

In Ulrich, 2011 different polygonal patterns are investigated in the western part of Utopia Planitia (an area of the northern Martian lowlands between 30°-60°N and 80°-120° E) and compared to network polygons found in Adventdalen valley. The study concludes that doing a geomorphometric comparison alone is not enough to discern if Martian polygons are due to ice-wedges, sand-wedges or sublimation. Evidence seems to point to thermal contraction cracking origin of the polygons in Utopia Planitia under specific small-scale local environmental conditions and mostly, by degradation processes such as ground-ice sublimation. As this process is extremely slow, it would explain the static conditions observed on the

region and hardly no changes on the geomorphology of the martian polygons.

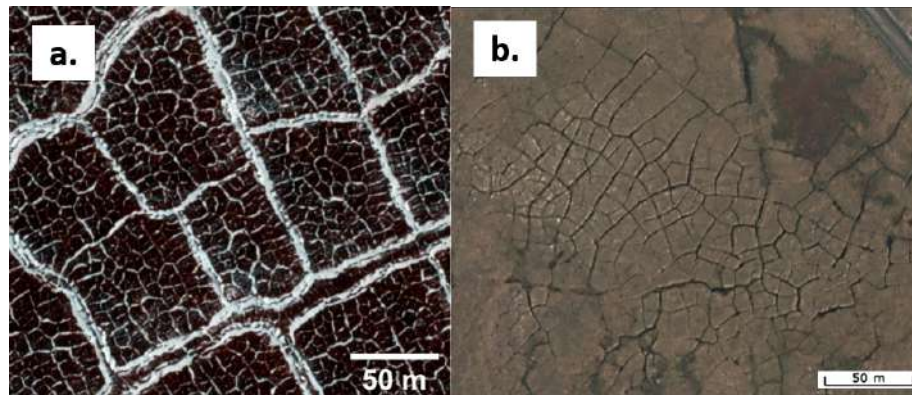


Figure 3.9: Comparison between a polygon pattern in Mars and on Earth. a) Multiple polygon pattern inside a crater on Mars, near  $69.787^{\circ}\text{N}$   $64.919^{\circ}\text{E}$  (Image from HiRise, ESP\_016641\_2500. Credit: NASA JPL University of Arizona). b) Polygon pattern due to ice-wedges on Adventalen Valley. Credit: © Norwegian Polar Institute/CC BY 4.0, Ortophoto

### *Pingos*

The identification of pingos on the Mars surface is by no means easy, as it can be easily misinterpreted (Dundas and McEwen, 2010). On the study of Soare et al., 2014 they propose three different scenarios for the formation of pingos in the Argyre impact basin (around  $37^{\circ}\text{S}$ ). The first one, considering a glacially driven hydraulic glacier supported by *wet flow* characteristics are also displayed by nearby landforms (eg. gullies). This scenario would be the same as those occurring on Earth (see Section 3.3) but instead of a valley, in a crater (Hauber et al., 2011). The second, a topographically induced hydraulic gradient, hypothesising that just a partial thaw of the crater slopes would be enough to cause meltwater migration into fissures, fractures under the regolith and give emergence to a pingo. The third, an hydraulic gradient from tectonic origin that would channel concentrated groundwater moved by artesian pressure and create the open-system pingo.

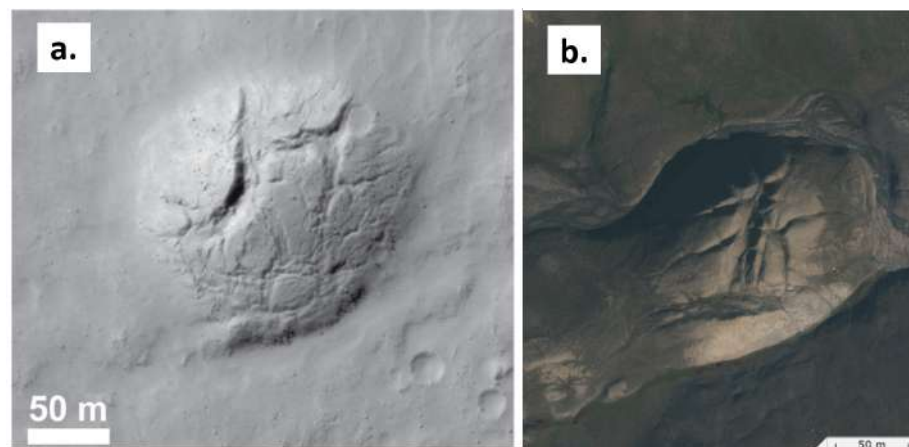


Figure 3.10: Comparison between a pingo in Mars and on Earth. a) Pingo on Mars ( $37.98^{\circ}\text{S}$ ,  $347.28^{\circ}\text{E}$ ) (Image from HiRise, Credit: NASA JPL University of Arizona). b) Pingo in Eskerdalen. Credit: © Norwegian Polar Institute/CC BY 4.0, Ortophoto

### *Alluvial fans and gullies*

Gullies are Martian landforms of particular interest. They are classified as young geomorphologies of 1-2 km long which are formed by recessed alcoves<sup>11</sup>, at least one sinuous channel and a fan or apron at the end of the channel mouth (Levy et al., 2011). It is not clear if their origin is linked to the presence of water. According to Levy et al., 2011 the geometry of martian gully channels seems to agree with fluid viscosities similar to those on Earth and not caused by dry granular debris flow. These geomorphologies are mostly found on surfaces modified by patterned ground (polygons), even though they might be also found on mid-latitude craters (Hauber et al., 2011)

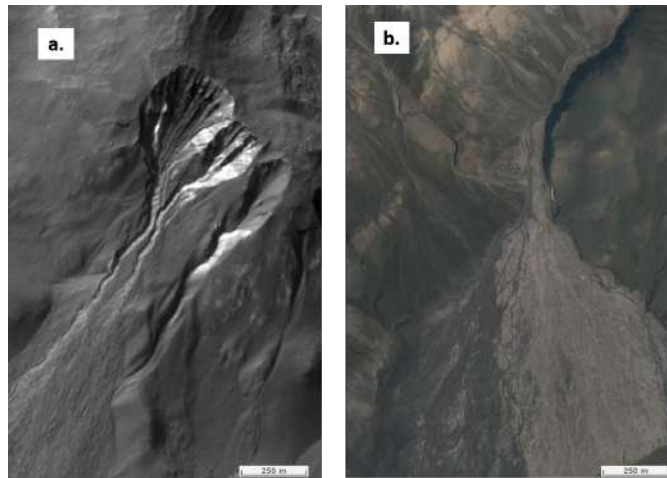
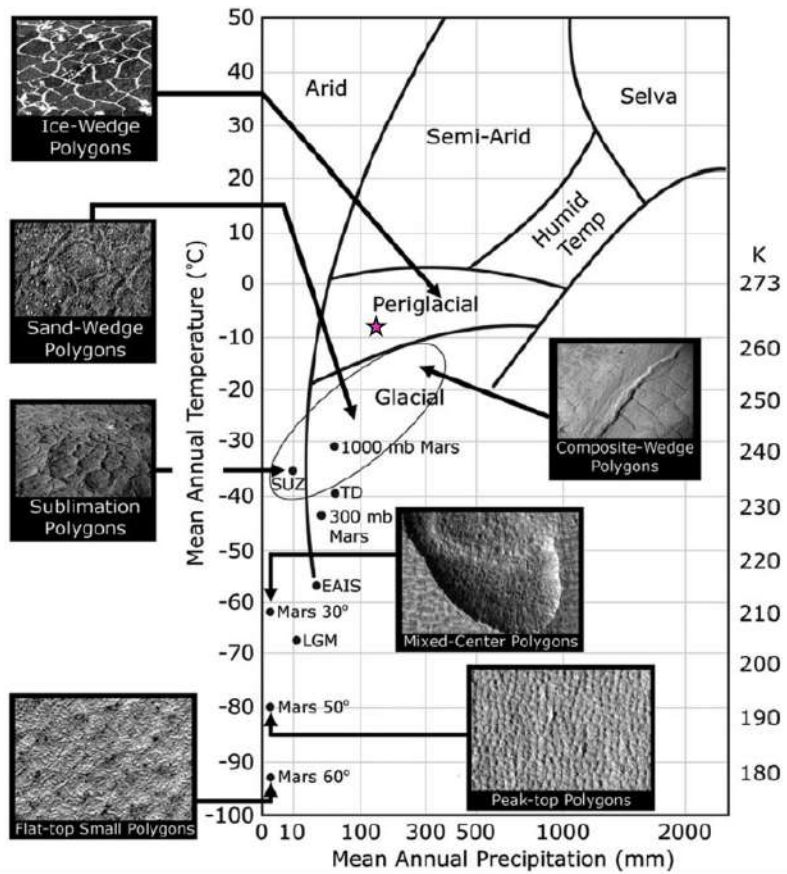
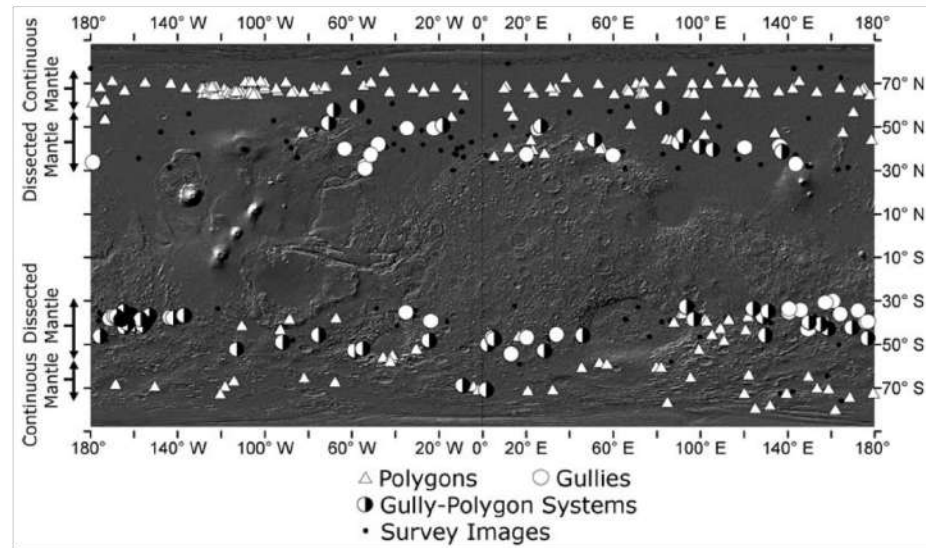


Figure 3.11: Comparison between gullies and alluvial fan formations in Mars and on Earth. a) Gullies ending with fan shape on Martian crater (38.58°S, 319.88°E) (Image from HiRise PSP\_006888\_1410, Credit: NASA JPL University of Arizona). b) Alluvial fan and gullies on Adventdalen. © Norwegian Polar Institute/CC BY 4.0, Ortophoto

<sup>11</sup>A steep, one-sided hollow on a rock wall caused by water erosion.



a)



b)

Figure 3.12: Permafrost landforms found in different climate regions (from Earth and Mars) and corresponding location on the Martian subsurface. a) Plot of permafrost landforms according to climate regions on Earth and Mars. The magenta star marks Svalbard; the oval shape represents the mean annual climatic conditions of the Antarctic Dry Valleys; SUZ stands for Antarctic Stable Upland Zone; TD indicates Taylor Dome; LGM indicates the Last Glacial Maximum in inland Antarctica. Image from Levy et al., 2011. b) Map showing the geographical distribution of periglacial landforms on the Martian surface. Note that these geomorphologies are clustered latitude-wise. Image from Levy et al., 2011



## 4. Methodology and Data retrieval

### 4.1 Fieldwork

The fieldwork campaign was conducted on Adventdalen valley and its vicinity (see [Figure 4.1](#)) by making GPR measurements, observing different periglacial landforms, collecting soil samples and drilling cores. The participants of the campaign are on one side UNIS and as external partners LATMOS (Le Laboratoire Atmosphères, Observations Spatiales) and TUD (Technische Universität Dresden), which integrate the WISDOM team.

Due to a malfunctioning pulseEKKO unit and later delay in receiving the spare part, the fieldwork was forced to split into two. First, a WISDOM campaign that took place during the 8th and the 18th of March 2022 and the second campaign, UNIS, on late March, late April and mid-May of the same year. The original period of time was chosen as temperatures in early March are well below  $0^{\circ}\text{C}$  (see [Section 2.1.3](#)) and therefore, the active layer is frozen. However, particularly from the 14th to the 17th of March temperatures were anomalously high even reaching positive values. On the 14th harsh weather conditions prevented fieldwork and instead, calibration measurements were done at UNIS snowmobile park. On the 16th, fieldwork had to be cancelled due to precipitation in form of rain. In contrast, UNIS campaign took place in days with cold conditions. On 1st of March temperatures ranged between  $-15^{\circ}\text{C}$  and  $-17^{\circ}\text{C}$ , late-March was extremely cold, plunging down to  $-22^{\circ}\text{C}$ , while mid-May they were at  $-10^{\circ}\text{C}$ . Despite the huge temperature differences between the campaigns and variations in snow accumulation of up to 1 m, it is assumed the main GPR targets remained the same and hence were comparable between surveys. [Table 4.1](#) shows the Eastings and Northings of the field sites and the date fieldwork was carried out.

A total of five different sites were visited. Site 1 (A and B) and Site 5 do not constitute a periglacial environment but the geological features were advantageous for GPR investigations. Sites 2, 3 and 4 target various periglacial landforms found at a relatively small area, upper Adventdalen and the start of Helvetidalen. Furthermore, the region is particularly interesting as it corresponds to the transition between land and sea level of ca. 15 ka ago, also known as the marine limit (ca. 70 m above the present sea level). The following sections briefly describe each of the sites in order to provide a context of the surroundings and conditions at the time of the WISDOM survey.



Figure 4.1: Map of fieldwork campaign sites. Background image credit: [© Norwegian Polar Institute/CC BY 4.0](#)

Table 4.1: Fieldwork campaign sites

Site ID	Name	WISDOM campaign	UNIS campaign	Geological Features	Activities	Position UTM 33 [m]	
						E	N
Site 1A	Longyearbreen	08-09/03/2022	1/03/2022	Snow-ice interface Ice-bedrock interface Meltwater channels	GPR investigations	511389	8677953
Site 1B	Longyearbreen	10/03/2022	11/05/2022	Snow-ice interface Ice-bedrock interface Meltwater channels Ice Cave	GPR investigations	510748	8677770
Site 2	Innerhytta	11/03/2022	28/03/2022	Pingo	GPR investigations Hand drilling (failed)	530798	8679912
Site 3	Adventdalen-Helvetidalen	(12;14)/03/2022	28/03/2022	Ice wedge polygons Alluvial fan	GPR investigations	531249	8681121
Site 4	River Bed Pingo	13-14/03/2022	28/03/2022	Pingo	GPR investigations Ice core drilling	533038	8680524
Site 5	Revneset-Hanaskogdalen	17-18/03/2022	27/03/2022	Ice-water interface Sandstone outcrop	GPR investigations	513477	8690340

### 4.1.1 Site 1

Site 1 corresponds to Longyearbreen, a small high-Arctic, low-activity and cold based glacier (Etzelmüller et al., 2000). The location has been chosen to proximity to Longyearbyen and the favourable conditions snow and ice present for GPR investigations. The site is subdivided into Site 1A and Site 1B. The first with the aim of testing the instruments and taking advantage of historical GPR data<sup>1</sup>. Mainly, the targets focus on the detection of the snow-ice interface compared to ground truth measurements (profile probing) and the detection of the glacier bedrock. Site 1B focuses on an ice cave<sup>2</sup> as GPR target. The goal is to detect the ice-air interface of the cave chambers and estimate its depth, in other words, to map the cave from above. Both sites are located at the edge of the glaciers were also small meltwater channels have been detected.



(a) Snow probing. Image credit: A.Le Gall, LATMOS



(b) WISDOM survey at the edge of Longyearbreen. Note the survey line going up-slope. Image credit: A.Le Gall, LATMOS



(c) Insights of the ice cave. Image credit: E.Zakutin, TU Dresden

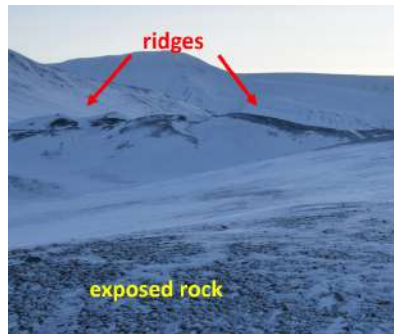
Figure 4.2: Site 1 - Longyearbreen

<sup>1</sup>GPR data that dates back to 2012 during UNIS course AT-329 led by prof.J.S. Rønning.

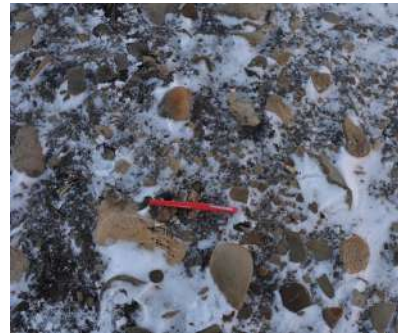
<sup>2</sup>The described *ice cave* is a prominent meltwater channel that people can access and walk through for about 150 m.

### 4.1.2 Site 2

Innerhytte pingo is located 20-km inland following Adventdalen valley, at the alluvial fan outwashing from Helvetidalen, constituting Site 2. It is a relatively big formation, with dimensions 410 m in the east-west direction and 200 m in the north-south direction and 28 m in height. Innerhytte is characterised by irregular and complex shapes, with a steep south flank caused by Adventelva river erosion and surface ice resulting of the pingo's discharge (Yoshikawa, 1993). In contrast, its north slope dips only mildly due to sediment accumulation. The surface lithology is characterised by glacio-fluvial deposits carried by the river and dark shales and siltstones of the Agardhfjellet Formation (Late Jurassic) that are exposed on the ridges (Major et al., 2000). This open-system pingo includes GPR surveys (Ross et al., 2005), electric resistivity tomography (ERT) (Ross et al., 2007) and seismic investigations (Rossi et al., 2018). In addition, within the framework of the Thermal State of Permafrost Norway International Polar Year project (Christiansen et al., 2010), a 20-metre-deep borehole was drilled close to the top of the pingo. Summarising from past research, it has not been possible to determine the existence of an underlying massive ice body, strengthening the hypothesis of only the presence of a bedrock remnant. Interesting features observed with GPR have been limited to the layering of alternating ice-rich shale structure.



(a) Top part of Innerhytta pingo. Image credit: W.S.Benedix, TU Dresden



(b) Exposed rock, pebbles and dark shale on Innerhytta. Pen for dimensions. Image credit: A.Le Gall, LATMOS

Figure 4.3: Site 2 - Innerhytta

### 4.1.3 Site 3

Site 3 is located at the opening of the massive alluvial fan that outwashes from Helvetidalen to Adventdalen valley up to Innerhytta. The area is surrounded by mountains of steep and uneven terrain (Arctowskifjellet to the East and Helvetiafjellet to the West), characterised by the abundant presence of gullies. On the south-eastern side of Helvetiafjellet, a carved path along the mountain slope (gullie), rocks and exposed debris indicate past activity (probably on summer) of a meltwater stream that ends in a smaller alluvial fan feeding the Helvetidalen outwash. On the south-western flank of Arctowskifjellet the terrain elevates itself from the alluvial fan and hosts a series of polygonal patterns that have been previously studied in the context of Martian geomorphologies by Ulrich, 2011 (see Section 3.2.1.1). This elevated terrain corresponds to a solifluction sheet<sup>3</sup> and has been targeted for cryostratigraphy investigations (Cable et al., 2018), indicating little visible ice both in the active and permafrost layer.

During the campaign the terrain was covered by snow and it is not possible to appreciate by naked-eye the troughs or centres of polygons.

<sup>3</sup>Layers of material in which movement is the result of differential downhill displacements provoked by a cyclic freezing-thawing of the active layer (Matsuoka, 2001).

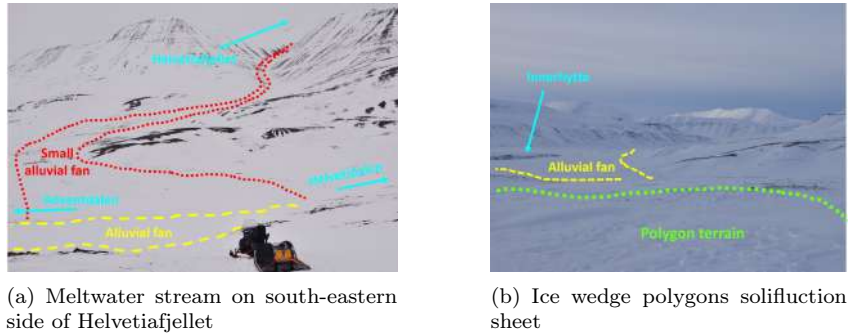


Figure 4.4: Site 3 - Ice wedge polygons and alluvial fan

#### 4.1.4 Site 4

Site 4 is on River Bed Pingo, which is located 1.5 km upstream for Innerhytta. Its topography is simple, one single dome of 100 m from east to west and 50 m from north to south. As with Innerhytta, its northern slope has been eroded by the Adventelva river accumulating glacio-fluvial material for a thickness of over 2.5 m while the southern slope is steeper and with a sediment layer of less than 1 m thick (Yoshikawa, 1993). The lithology comprises glacio-fluvial sediments, shales and siltstones of the Agardhfjellet Formation (Major et al., 2000). Another feature of the pingo is a flooded area surrounding its southern and south-western flanks. This water surcharge comes from underground forming large ponds covered by a crust of orange-brown ice, in some cases half a meter thick and in others barely a centimetre, and ice domes. This formation has also constituted a target on itself due to alternation of ice, water and bedrock layers. It must be noted that River Bed Pingo has also been subject of several investigations. A comprehensive study on the ice core, its crystallography and different ice layers was done by Yoshikawa, 1993. More recent studies include a GPR survey (Ross et al., 2005) and ERT (Ross et al., 2007).



(a) River Bed Pingo (image from south-western side)

(b) Frozen underground water



(c) Shales and glacio-fluvial sediments

(d) Ice core from River Bed Pingo ice dome

Figure 4.5: Site 4 - River Bed Pingo. Image credit: A.Le Gall, LATMOS

### 4.1.5 Site 5

Site 5 focuses on two different outcrops at Reveneset-Hanaskogdalen location. Despite not corresponding to a periglacial landform per se, outcrops are interesting features from the point of view of GPR survey. They present direct ground-truth and provide a visual display of the actual layering of the terrain just below the GPR readings. One of the target outcrops is ca. 20 m high and has been carved by Hanaskogelva river. The top is characterised by a soil layer (shales and sediments) of 20 cm or less (in some cases bare rock is exposed) while below it is found weathered sandstone, with many fractures and mostly horizontal foliation. The second outcrop is a fault provoked by a sandstone formation protruding out of the soil. The stones are totally exposed and bare, with no sediments on top, only ice and snow. Both outcrops belong to Rurikfjellet Formation (early Barremian) (Major et al., 2000).



(a) Hanaskogelva outcrop

(b) Sandstone fault outcrop

Figure 4.6: Site 5 - Sandstone Outcrop

## 4.2 Remote Sensing and GIS analysis

According to USGS (United States Geological Survey) *Remote Sensing* consists of the detection and monitoring (via satellite or aircraft) of the physical characteristics of a specific region by means of measuring the emitted and reflected radiation. Whereas GIS, as its name indicates (Geographic Information System), establishes a relationship between a given information and its geographical reference. Both have been used for studying the different periglacial landforms in Adventdalen.

The database developed by the (NPI) provides topographical information as well as high-resolution aerial images of the region of interest. The same database offers different *cached* and *dynamic* (WMS) base map services, ready to be used as layers in mainstream GIS software. For this project, the WMS service of Svalbard ortophotos has been used. It consists of a true-color mosaic of airborne orthoimages of Svalbard with a resolution up to 0.17 m approximately (1:625 scale). These high resolution images have been paramount to determine the regions of interest and made possible the geomorphological analysis of their periglacial landforms. However, topographic lines from the topographical basemap dataset *S100 Kartdata*, a vector basemap of Svalbard in scale 1:100000 are spaced every 50 m except the first 50 m in which they are subdivided into 0 m to 25 m and 25 m to 50 m. These topographic lines are not particularly detailed and hence another source was used. The topographic lines have been obtained from the open-source [Arctic DEM](#) as the height interval can be reduced down to 1 m divisions.

[QGIS 3.14](#), an opensource GIS software, was employed for visualising the different GPR lines retrieved at the periglacial landforms, analysing the ice-wedge polygons and complementing GPS information by generating a DEM based on the aforementioned source.

### 4.2.1 Geometrical characterisation of ice-wedge polygons

The geometrical characteristics of ice-wedge polygons are a relevant to understand the context in the formation of these patterns on the ground (see Section 3.2.1.1). The following geometrical parameters have been selected as the principal ones defined in Ulrich, 2011 that provide a description of the shape and dimension of the polygons. Below, a brief description of the parameter and how is given; note that some definitions are conceptually different from Ulrich, 2011:

- **Area (A):** dimensions parameter obtained with [QGIS 3.14](#) geometry tools.
- **Perimeter (P):** dimension parameter obtained with [QGIS 3.14](#) geometry tools.
- **Diameter (D):** dimension parameter. It is defined as  $\sqrt{4A/\pi}$ . In Ulrich, 2011 Table 3.2 is defined as *Size*. This parameter is derived from the definition of an area of a circle  $A_c = \pi(D/2)^2$ , isolating the diameter  $D$ . Hence, it is the diameter associated to the real area of the polygon if this area was contained in a circle.
- **Max. and Min. diameter (L,S):** dimension parameters. They are defined as the longest (L) and shortest axis (S) of the polygon, respectively. According to Ulrich, 2011 Table 3.2 and Figure 3.3 the length and the width are calculated as the longest and shortest side of a minimum bounding rectangle. [Figure 4.7](#) illustrates the difference between definitions. The choice of using the axis is because they correspond to the actual mathematical definition to calculate the elongation ( $E$ ) of a polygon  $E = 1 - S/L$ , being  $S$  the shortest axis and  $L$  the longest, where both lines cross the centroid of the polygon. By defining a minimum bounding rectangle, the length and width obtained do not necessarily cross the centroid.
- **Circularity (C):** shape parameter. Indicates how far from a circle shape the polygon is, ranging from 0 (extreme case of a line) to 1 (circle). It is defined as  $4\pi A/P^2$ . If the polygon is a circle, then  $P = 2\pi r$  and  $A = \pi r^2$  and hence  $C = 4\pi \cdot \pi r^2 / (2\pi r)^2 = 1$ .

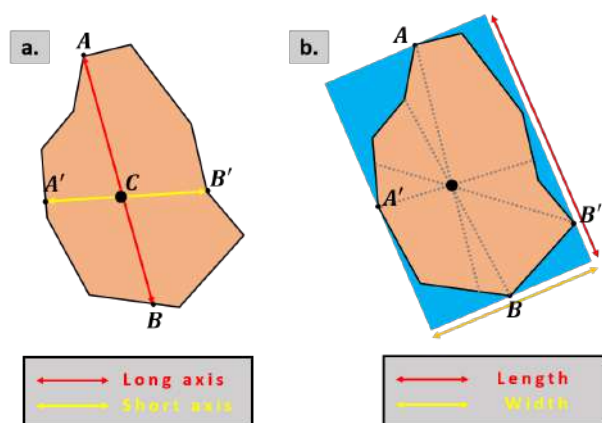


Figure 4.7: Definition of geometrical parameters of ice-wedge polygons. (a) Definition of maximum and minimum diameter (long and short axis) in this project. (b) Definition of largest and minimum diameter in Ulrich, 2011. Note how the points defining the Length and the Width do not generate a line crossing the centroid. The definition in (a) imposes that the distances cross through the centroid of the polygon, being mathematically accurate on the definition of a polygon's elongation. Method in (b) yields close results to (a) and it is possible to obtain find at *QGIS Minimum Bounding Geometry*

- **Aspect Ratio (AR):** shape parameter. It is the complementary to elongation and it is defined as the ratio between the shortest and longest axis,  $AR = S/L$ . Similar to circularity, indicates how much the polygon tends to a circle, taking values from 0 (extreme case of a polygon degenerating to line) and 1 (circle).

#### 4.2.2 Estimation of subsurface ice in ice-wedge polygon region

*QGIS* is a powerful tool to quantify the volume of the ice wedges in Adventdalen patterned ground areas. In fact, GIS analysis has already been used on ice-wedge polygon patterns to determine the amount of ice below the subsurface. The work of Ulrich et al., 2014 in Siberia's and Alaska's polygonal networks aimed to develop a relatively simple GIS-based method to calculate ice-wedge volumes, combining remote sensing and -limited- ground data. The methodology applied was divided into manual delineation of polygons and a semi-automated method based in the generation of a Voronoi diagram (Thiessen polygons<sup>4</sup>). Bernard-Grand'Maison and Pollard, 2018 built upon polygon network GIS mapping and added another method of semi-automated delineation known as watershed segmentation. This last method has similarities with petrographic analysis, where the edges from the grain boundaries of thin sections are detected. It must be noted that the purpose of semi-automated techniques for delineating the ice-wedge polygons is improving the time efficiency and coverage extension but do not present an advantage quality-wise compared to manual delineation.

The process to quantify ice-wedge volume is based on the methodology described in Ulrich et al., 2014 with slight modifications. First, polygons lines are drawn following the trough centerlines of the ice-wedge polygons. Second, the polygons are converted into lines and a buffer with the same width as the troughs is applied. It is assumed that the width of the troughs is the same as the width of the top of the ice-wedge (Matsuoka et al., 2018) being this assumption also carried out in the estimations of Ulrich et al., 2014 and Bernard-Grand'Maison and Pollard, 2018).

Two approaches have been considered to calculate the total ice-wedge volume. On the one hand, taking the resulting buffer area ( $A_{buffer}$ , Figure 4.8.d) as the area corresponding to the the top of the ice-wedges

<sup>4</sup>Voronoi tessellation or Thiessen polygons are the result of a geometric interpolation given a set of points. Each point is connected through a line to its neighbouring points. The mediatrices of each connecting line segment are drawn and will intersect each other, resulting in a Thiessen polygon.

and calculating straightforward the volume given the depth  $d$  of the ice-wedges and their isosceles shape,

$$V_{ice} = A_{buffer} \cdot 1/2 \cdot d \quad (4.1)$$

This method presents a problem at the intersection of the buffer lines where there is a discontinuity in ice distribution. This *missing* ice results in a *lower bound* estimation of the total ice-wedge ice.

On the other hand, the ice-wedge volume can also be calculated as the difference between the total volume of the studied area minus the volume of the sediments (non-icy volume of the polygons). It can be expressed in the following way:

$$V_{ice} = V_{total} - V_{sediments}$$

In fact, the above equation is rearranged so that the wedge ice is calculated at the interior of each polygon and for the perimeter of the great polygon area formed by all polygons:

$$V_{ice} = \sum_i^N (V_{polygon_i} - V_{sediment_i}) + (V_{great\ polygon} - V_{inv\ pyramid}) \quad (4.2)$$

Let's focus on the first term. The volume of sediments of the  $i$ -th polygon is calculated as the trunk of a pyramid volume following the formula:

$$V_{sediment_i} = \frac{1}{3} \cdot d \cdot (A_{top} + A_{bottom} + \sqrt{A_{top} \cdot A_{bottom}}) \quad (4.3)$$

Where  $A_{top}$  corresponds to the area of the polygon once subtracted the buffer and  $A_{bottom}$  the area corresponding to the original delineated polygon (see [Figure 4.8.e](#) [Figure 4.9](#) Cross Section I). The total volume (ice and sediments) from the  $i$ -th polygon is calculated according to:

$$V_{polygon_i} = A_{polygon_i} \cdot d; \quad A_{polygon} \Leftrightarrow A_{bottom} \quad (4.4)$$

The term  $\sum_i^N (V_{polygon_i} - V_{sediment_i})$  results in the volume of ice at the half-buffer areas surrounding polygons (see [Figure 4.8.h](#) and blue non-patterned areas of [Figure 4.9](#) Top View). This volume does not correspond to the complete wedge-ice volume as it is missing half of the area for the outer-buffer boundary<sup>5</sup> (see blue striped areas of [Figure 4.9](#)). The corresponding wedge-ice volume for the outer boundary is calculated as the difference of the total volume from all polygons included the buffer ( $V_{great\ polygon}$ ) and an imaginary inverted trunk of pyramid ( $V_{inv\ pyramid}$ ) with top surface  $A_{great\ polygon}$  and bottom  $A_{merged\ polygons}$ <sup>6</sup> (see [Figure 4.9](#) Cross Section II). This calculation takes advantage of the fact that the outer-boundary ice-wedge volume is geometrically equivalent to remaining soil under the ice-wedge (see "reciprocal volume" in [Figure 4.9](#)). Once all parameters are calculated the total wedge-ice is obtained applying eq.4.2, which presents an *upper bound* estimation.

It must be noted that this method comes with its limitations. First, it assumes the shape and depth of all ice-wedges to be homogeneous in the chosen area. According to Mackay, 1990 epigenetic ice-wedges usually take an inverted isosceles triangle shape, but this does not exclude that some ice-wedges might be irregularly shaped nor the fact that their depth will vary alongside characteristics of that particular crack. Furthermore, it is possible these ice-wedges contain veins of silt or sand and even gas inclusions (French, 2017) while the model presumes they are made of pure ice. In Bernard-Grand'Maison and Pollard, 2018 the very retrieval method of the images is discussed as source for error. Indeed, the delineation of ice-wedge polygons on satellite or airborne images is bounded to the visible features in those images. Shadowing, vegetation and many other factors might lead to absence of a *perceptible* trough (even limit its formation) leading to a mistaken conclusion of lack of wedge-ice. The opposite is also true, attributing wedge-ice to troughs which might not contain it. For this reason, both in Ulrich et al., 2014 and Bernard-Grand'Maison and Pollard, 2018 ground truth data complements remote sensing imagery.

The ice-wedge volume estimation from GIS is therefore, taken as a first approximation and providing an order of magnitude of the subsurface ice in the selected patterned ground regions.

<sup>5</sup>From now on the half of the area for the outer-buffer boundary will be referred to as outer-boundary.

<sup>6</sup>Note:  $A_{great\ polygon}$  is the area enclosed by the outermost boundary of the buffer while  $A_{merged\ polygons}$  is the area enclosed by the boundary of the originally delineated polygons.  $A_{merged\ polygons}$  can be calculated by summation of the area of each individual delineated polygon



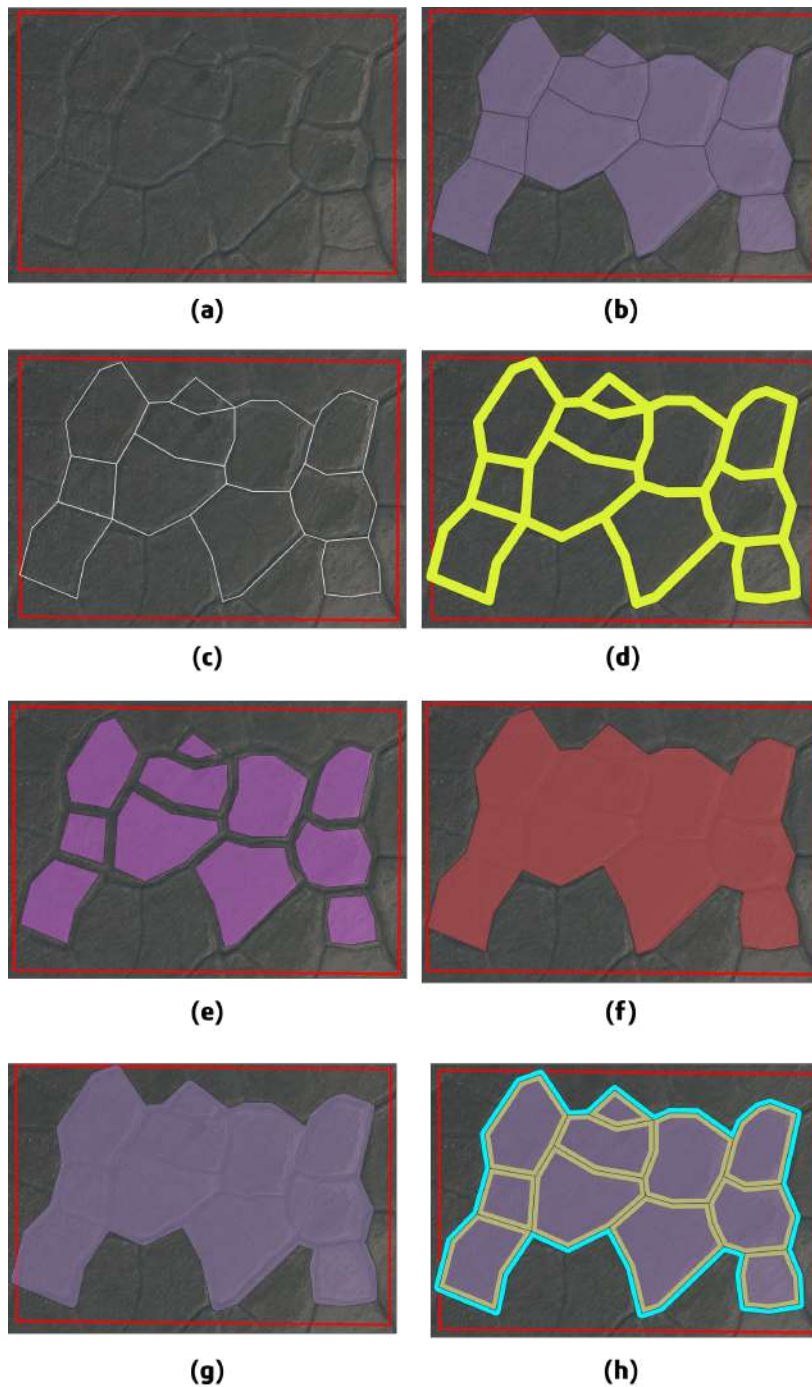


Figure 4.8: Digitisation of ice-wedge polygons with GIS. a) Close-up to example study area in Adventdalen. b) Manually delineated polygons. Polygon lines are drawn over the centerlines of the troughs. c) Polygon features turned into lines. d) Buffer lines of 2 m (total width 4 m) marking the complete extent of the troughs. e) Inner polygons obtained by subtracting the buffer lines in (d) from the originally delineated polygons in (b). These areas will correspond to the top area for the sediment volume calculation. f) Merged polygons (polygons in (b) dissolved into one). g) Area corresponding to the polygons in (b) plus the extent of the buffer line in (d). h) Blue: half-buffer area outer boundary. Yellow: half-buffer area surrounding polygons. Purple: Inner polygons. Background image credit: © Norwegian Polar Institute/CC BY 4.0

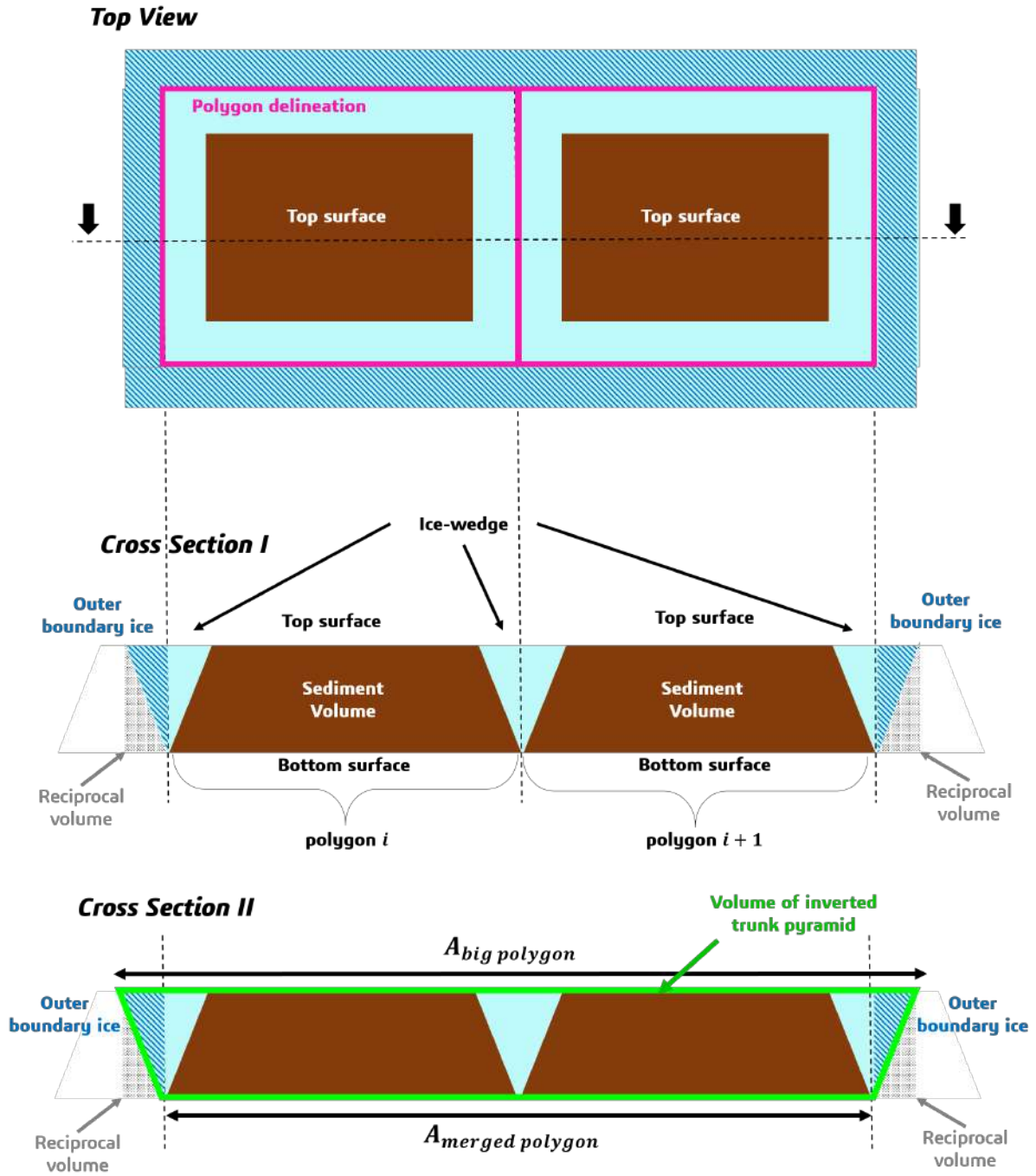


Figure 4.9: Diagram of ice-wedge polygons. Top View: simplified representation of rectangle-shaped ice-wedge polygons. The buffer area is formed by the outer boundary (blue stripes) and the inner boundary surrounding each polygon (plain light blue). The magenta lines mark the original delineated polygons. The brown area marks the inner polygons. Cross Section I: sliced-view of polygons and ice-wedges. The sediment volume has a trunk-of-pyramid shape. Adjacent sides of the polygon to another polygon form a full ice-wedge inside the buffer boundary. Cross Section II: Visualisation of the inverted pyramid to calculate the outer-boundary wedge-ice. Geometrically is reciprocal to the volume corresponding to the soil below the wedge-ice.

## 4.3 Ground Penetrating Radar

Ground Penetrating Radar (GPR) is a geophysical technique that uses radio waves to *see* below the surface of the ground (Jol, 2009). It consists of a central unit, a transmitting antenna, a receiving antenna and a computer and it uses the principle of scattering electromagnetic (EM) waves to locate buried objects (Daniels, 2000).

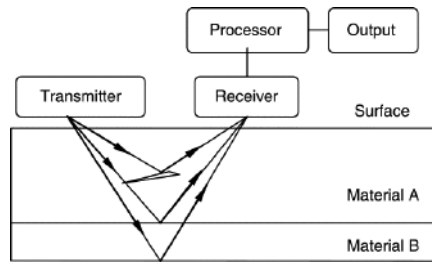


Figure 4.10: GPR system basic functioning. Image from (Dong and Ansari, 2011)

The central unit generates an EM signal <sup>7</sup> that is radiated towards the probed material with a conical volume shape and travels through the media at a velocity determined primarily by the permittivity of the material (Daniels, 2000; Persico, 2014). The waves spread downwards until they encounter discontinuities (which can be buried objects, the interface between two soil layers, a cavity, different moisture content, etc.), provoking a scattering of the EM waves (Daniels, 2000; Dong and Ansari, 2011). Part of the waves remain in the same direction of travel while others are reflected. These reflected pulses are received by the receiver antenna and their corresponding amplitudes and arrival times are used for determining the properties

and location of the discontinuity (Dong and Ansari, 2011). The versatile nature of GPR systems has caused a proliferation of its usage, including research taking place in periglacial environments for example, to map discontinuous reflectors<sup>8</sup> (Senger et al., 2014), to define geophysical facies of a paleokarst system (Janocha et al., 2021), to investigate the structure, drainage system and estimate volume changes of glaciers (Bælum and Benn, 2011; Berthling et al., 2000; Lapazaran et al., 2013; Navarro et al., 2016), the estimation of sub-surface ice volume in ice-wedge polygons areas (Andres et al., 2020; Bode et al., 2007; Watanabe et al., 2013), the study of pingos (Ross et al., 2005), the estimation of the soil moisture content (Gacitúa et al., 2012), etc. Still, further research on permafrost environments by GPR systems is required to fully understand its performance in such conditions, in particular, 3D surveys.

### 4.3.1 Overview of the basic principles

#### 4.3.1.1 Electromagnetic properties and wave phenomena

GPR investigations are based on EM theory<sup>9</sup>, which explains the interaction between the emitted signal and the soil media. These interactions might be the product of changes in the materials that conform the soil or the intrinsic properties of the material itself.

When an the emitted EM wave goes through an interface between two materials, its amplitude and direction of travel varies. The wavefront might be: reflected, transmitted, refracted or scattered just as shown in Figure 4.11.

<sup>7</sup>EM waves usually in the range of 10 to 1000 MHz (Dong and Ansari, 2011)

<sup>8</sup>Such as sub-seismic faults, the variation of sedimentary facies and igneous intrusions.

<sup>9</sup>The reader is referred to Chapter 1 of Jol, 2009 for an overview of the principles of EM theory applied to GPRs.

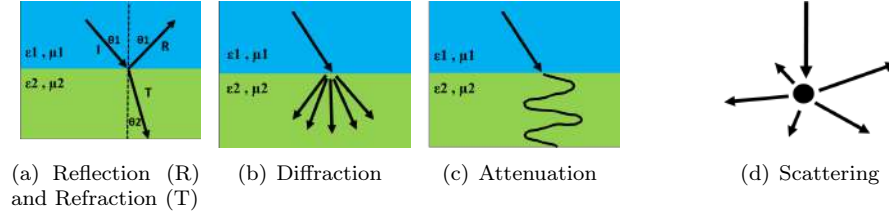


Figure 4.11: Wave phenomena. Adapted from (Robinson and Clark, 2017).

The causes for a change in amplitude and direction in the emitted signal can be explained by the changes in the electrical conductivity, the dielectric permittivity and the magnetic permeability of the different media, which constitute the most relevant properties of a soil for GPR surveys (Fitterman, 2015; Jol, 2009):

- **Electrical conductivity ( $\sigma$ ):** the movement of free charges (or in other words, the creation of an electric current) when an electric field is applied. The electrical conductivity is expressed in Siemens per meter ( $S \cdot m^{-1}$ ) and it is reciprocal to electrical resistivity (ohm-meter,  $\Omega m$ ), being  $\sigma = 1/\rho$ .
- **Dielectric permittivity ( $\epsilon$ ):** the displacements of constrained charges (polarization) after the application of an electric field. The value of dielectric permittivity influences the magnitude of the electric field created by the charges, being inversely proportional. The permittivity in vacuum is expressed as  $\epsilon_0 = 10^{-9}/36\pi F/m = 8.89 \cdot 10^{-12} F/m$  and is constant. This parameter is one of the most important quantities in GPR applications, expressing dielectric permittivity in terms of *relative permittivity* or *dielectric constant*  $\epsilon_r = \kappa = \frac{\epsilon}{\epsilon_0}$ .
- **Magnetic permeability ( $\mu$ ):** response of the atomic and molecular magnetic moments to an external magnetic field. In geological materials this is caused by the presence of magnetic minerals. Just mirroring the definition of relative permittivity, the *relative permeability* is defined as  $\mu_r = \frac{\mu}{\mu_0}$ . Expressed in henry per meter  $H/m$ . Where magnetic permeability in vacuum is  $\mu_0 = 1.25 \cdot 10^{-6} H/m$

For the sake of simplicity, in most GPR applications the values of  $\sigma$ ,  $\epsilon$  and  $\mu$  are considered to be scalar constants, independent of the field strength and invariable in time. In fact, for practical purposes the variations in  $\mu$  are of hardly any relevance, thus, centering the attention to variations in  $\epsilon$  as  $\sigma$  (Jol, 2009).

But, how do these properties affect the GPR signal? A GPR efficacy relies on low-loss materials where the energy dissipation is small compared to the energy storage (Jol, 2009), so that the soil conditions yield a wave-like response. As EM waves propagate, their amplitude ( $A$ ) exponentially decays from its original value ( $A_0$ ) as distance ( $z$ ) increases (Neal, 2004), where  $\alpha$  is the attenuation constant:

$$A(z) = A_0 e^{-\alpha z} \quad (4.5)$$

Hence, a key parameter is the attenuation, defined by Equation 4.6 and expressed in dB/m.

$$\alpha = 8.686\omega \sqrt{\frac{\mu\epsilon}{2} \left( \sqrt{1 + \left(\frac{\sigma}{\epsilon\omega}\right)^2} - 1 \right)} \quad (4.6)$$

Other key parameters that determine the EM field properties are the propagation velocity ( $v$ ) and the impedance ( $Z^{10}$ ) (Annan, 2005).

The velocity (m/s) is expressed in Equation 4.7 (Balanis, 2012) where  $c$  is the speed of light ( $3 \cdot 10^8 m/s$ ) and  $\omega = 2\pi f$ ,  $f$  being the frequency in Hz. :

$$v = \frac{c}{\sqrt{\frac{\mu\epsilon}{2} \left( \sqrt{1 + \left(\frac{\sigma}{\epsilon\omega}\right)^2} + 1 \right)}} \quad (4.7)$$

<sup>10</sup>The impedance is defined as the ratio between the transverse electric and magnetic field and it is expressed in ohms ( $\Omega$ ):  $Z = \sqrt{\mu/\epsilon}$ .

Both equations present the dependency with the media properties and the frequency of the wave signal. Hence, the properties of the soil and the operational frequency of the GPR will have a direct impact on its resolution and depth penetration. The higher the frequency, the more attenuation, so the GPR system will have to keep its operational frequency below the transition frequency<sup>11</sup> in order to optimise its efficiency.

A simplified version of the propagation velocity and attenuation for a soil with low losses is (Jol, 2009):

$$v = \sqrt{\frac{1}{\epsilon \cdot \mu}} = \frac{c}{\sqrt{\kappa}}; \quad \alpha = \frac{\sigma}{2} \sqrt{\frac{\mu}{\epsilon}} = Z_0 \cdot \frac{\sigma}{2\sqrt{\kappa}} \quad (4.8)$$

exclusively dependant on the media properties of relative permittivity,  $\kappa$ , and conductivity,  $\sigma$ . Table 4.2 shows how the propagation velocity decreases as permittivity increases and how attenuation mostly influenced by the conductivity (high conductivity, high attenuation).

Table 4.2: Permittivity, velocity propagation and attenuation through different media. Data values retrieved from Cassidy, 2008 and Reynolds, 2011, ordered from lowest to highest permittivity.

Material	Permittivity ( $\epsilon_r$ )	Propagation velocity ( $v$ ) [m/ns]	Electical conductivity ( $\sigma$ ) [mS/m]	Attenuation ( $\alpha$ ) [dB/m]
Air	1	0.3	$10^{-9}$	<1
Polar snow	1.4-3	0.194-0.252	5	<1
Polar ice	3-3.15	0.168	1-10	<1
Fresh water ice	3-4	0.15-0.17	1	<1
Sand (dry)	4-6	0.12-0.15	0.001-1	<1
Limestone (dry)	4-8	0.11-0.15	0.001-0.000001	<1
Sea water ice	4-8	0.11-0.15	10-100	8-57
Granite (dry)	5-8	0.11-0.13	0.001-0.00001	<1-5
Concrete (dry)	4-10	0.09-0.15	1-10	<1-5
Granite (wet)	5-15	0.08-0.13	1-10	<1-4
Limestone (wet)	6-15	0.08-0.12	10-100	6-42
Clay (dry)	2-20	0.07-0.21	1-100	1-36
Concrete (wet)	10-20	0.07-0.09	10-100	5-36
Soil (average)	16	0.08	5	2
Sand (wet)	10-30	0.05-0.09	0.1-10	<1-3
Clay (wet)	15-40	0.05-0.08	100-1000	42-252
Fresh water	81	0.03	0.1-10	<1
Sea water	81	0.03	4000	>600

#### 4.3.1.2 Ground Penetrating Radar Design Specifications

The parameters that are essential for the design specifications of a GPR system are: the bandwidth and center frequency, the resolution, the dynamic range and the unambiguous range (Jol, 2009).

##### *Bandwidth and Center frequency*

The center frequency  $f_c$  is the one that characterises a GPR system. For practical reasons, the bandwidth  $B$  of the system is centered at  $f_c$  and usually has an equal value (Jol, 2009). For example, a 100MHz GPR refers to a system centered at 100MHz with a 100MHz bandwidth. The bandwidth can be defined as the inverse of the pulse width  $\tau_p$  for impulse systems and as the difference between start  $f_{min}$  and stop frequencies  $f_{max}$  for continuous-wave systems:

$$B = \frac{1}{\tau_p}; \quad B = (f_{max} - f_{min}) \quad (4.9)$$

##### *Resolution*

Resolution is the limit of certainty to determine the position and geometry of a target (size, shape,

<sup>11</sup>Frequency threshold that if surpassed, in an ideal media, attenuation would increase linearly with frequency

thickness). Expressed in terms of wave phenomena, resolution establishes how closely spaced in time two reflected pulses can be to be distinguished from one another. For a GPR, resolution is divided into the two possible dimensions as depicted in Figure 4.12 (Warren, 2009):

- **Vertical or depth resolution:** also known as range or longitudinal resolution. The minimum vertical spacing between two targets ( $\Delta r$ ) is proportional to the width of the pulse ( $W$ ) and the travelling velocity ( $v$ ), but independent of the distance from the target<sup>12</sup>. The higher the frequency the GPR uses the more the pulse width shrinks, hence, a greater accuracy for the vertical spacing which equates to a higher the resolution. The depth resolution can also be expressed in terms of the a bandwidth  $B$ , the dielectric constant  $\epsilon_r$  and the speed of light  $c$  (Jol, 2009):

$$\Delta r = \frac{Wv}{4}; \Delta r = \frac{1.39c}{2B\sqrt{\epsilon_r}} \quad (4.10)$$

- **Horizontal or lateral resolution:** angular or sideways displacements. The minimum horizontal spacing ( $\Delta l$ ) is proportional to the width of the pulse, the travelling velocity and the distance from the target ( $d$ )

$$\Delta l = \sqrt{\frac{vrW}{2}} \quad (4.11)$$

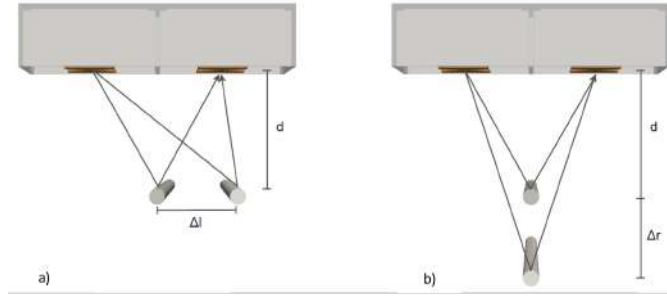


Figure 4.12: Definition of lateral (a) and vertical (b) resolution. Image from Warren, 2009

### *Dynamic Range*

The dynamic range is defined as the ratio between the largest receivable signal and the minimal detectable signal, expressed in decibels (dB) and directly affects the maximum range at which a target can be detected (Jol, 2009):

$$\text{Dynamic Range} = 20 \log \left( \frac{V_{max}}{V_{min}} \right) \quad (4.12)$$

Its value is given together with a specific bandwidth, expressed in Hz. The value of  $V_{max}$  (after the gain) corresponds to the maximum sample voltage of the ADC and the  $V_{min}$  is the minimum detectable signal, with minimum SNR and above the receiver noise.

### *Unambiguous range and Penetration Depth*

The unambiguous range is defined as the furthest distance from which a target can be distinguished without the signal experimenting aliasing<sup>13</sup> (Jol, 2009). If a target surpasses the unambiguous range, it means that by the time the reflected signal has returned to the receiver, the next pulse was emitted, hence, the GPR system cannot deduce if the signal received belongs to the second pulse or the first (ambiguity). In fact, targets beyond the unambiguous range would appear erroneously in the same location as closer

<sup>12</sup>In practice, this is not true as with depth there is an increase in signal dispersion and attenuation (Jol, 2009)

<sup>13</sup>Indistinguishable signals

targets. For impulse radars, the unambiguous range is defined as (Jol, 2009):

$$R_{max} = \frac{cT_r}{2\sqrt{\epsilon_r}} \quad (4.13)$$

Where  $\epsilon_r$  is the dielectric constant,  $c$  the speed of light and  $T$  is the pulse repetition interval in which signals are emitted (usually referred to as *programmable time window*). For continuous wave radars, the following equation defines the  $R_{max}$  (Jol, 2009):

$$R_{max} = \frac{Nc}{4B\sqrt{\epsilon_r}} \quad (4.14)$$

where  $N$  is the number of frequency steps and  $B$  the bandwidth. It is important that the unambiguous range and the penetration depth are conceptually different. Penetration depth is the maximum range at which the signal reflected is still detectable by the receiver. The penetration depth of a GPR system is highly affected by the properties of the soil, such as the presence of clays, ions in water, specific minerals, etc. which in turn, affect the dielectric constant and the electrical conductivity of the media (being magnetic permeability negligible). This, affects both the wave propagation velocity ( $v$ ) and the attenuation ( $\alpha$ ), being the attenuation the governing parameter to determine depth penetration (Leucci, 2008; Warren, 2009). The unambiguous range is strictly defined by the travelling time towards and back from the target in which a signal is distinguishable from another.

#### 4.3.1.3 Velocity Analysis

The propagation velocity of the signal through the media allows to convert the travelling time to position (depth), according to the following relation:

$$v = \frac{2 \cdot d}{TWTT} \iff d = \frac{v \cdot TWTT}{2} \quad (4.15)$$

Where TWTT is the Two-Way Travelling Time (from the GPR to the target and back to the receiver, hence the "2" factor) and  $d$  is the *apparent depth*<sup>14</sup>. As the choice of velocity will condition the depth at which the objects are positioned, there are several strategies to estimate it. If the geology of the area is known, it is possible to do a first guess with the guidance of tabulated values for different media which can be found for eg. in Cassidy, 2008; Davis and Annan, 1989; Reynolds, 2011. Other methods include CMP (Common Midpoint) gathering, consisting of varying the antenna spacing and measuring the change in the TWTT to obtain an estimate of the velocity versus ground depth (Jol, 2009) and hyperbola fitting. The latter based on the hyperbolic shapes that point reflections take with different velocities. Then, it is possible through an iterative process to find a velocity that fits best the hyperbola shapes generated.

#### 4.3.1.4 Signal Processing

Signal processing of GPR data encompasses from simple editing to total transformation of the GPR information. The processing method is an iterative exercise which is subjected to the bias of the interpreter who will judge the suitability of the final data obtained in contrast with the initial raw data.

The most common processing steps that have been used for this project include:

- **Dewow filtering:** The effect of *wow* on a GPR signal consists of a *lifting* up or down from the base level of the signal (Jol, 2009). The dewowing process brings the signal down suppressing this effect.

<sup>14</sup>The velocity of propagation value varies due to heterogeneities on the media. An average value is chosen, hence the true depth cannot be calculated as would be necessary to model the exact layers of the soil. It is referred as *apparent depth* as it is bound to the velocity of propagation chosen.

- **Signal gain:** As depth increases the signal becomes weaker due to attenuation. To compensate this phenomena is common to introduce a time-dependent gain function which boosts the amplitude at deeper depths. There are many different ways to implement a time gain, but the most common ones are power gain ( $x_g(t) = x(t) \cdot t^\alpha$ ), exponential gain<sup>15</sup> ( $x_g(t) = x(t) \cdot e^{\alpha t}$ ) and automatic gain control (the gain is equal to the local root mean squared signal) (Huber and Hans, 2018).
- **Deconvolution<sup>16</sup>:** is an analytical process designed to remove the effect of a previous filtering operation (Kearey and Brooks, 2002; Neal, 2004). The purpose is to maximize the bandwidth and reduce the dispersion of the pulse to obtain maximum resolution, however, GPR pulses are already the shortest and most compressed that can be achieved for optimal SNR conditions, making this method rarely of high benefit (Jol, 2009).
- **Migration:** consists of the removal of diffractions, changes in the dip of slope, distortions and reflections to reconstruct the geometrically correct distribution of the subsurface (Jol, 2009; Neal, 2004). It is a form of spatial deconvolution to increase spatial resolution, and to do so, it is necessary to know the velocity structure (Jol, 2009; Kearey and Brooks, 2002; Neal, 2004). There are different methods for migration: Kirchoff, Stolt, reverse time, finite difference, etc Huber and Hans, 2018; Jol, 2009; Neal, 2004.
- **Frequency filters:** Frequency filters act on the following principle: some frequencies are kept and others are rejected. Depending on which ones are filtered they are given different names: bandpass (allows to pass frequencies of a certain range and rejects the rest), low-pass (only allows to pass low frequencies), high-pass (allows to pass only high frequencies), notch-filters (rejects a specific frequency or range of frequencies, etc).
- **Topographic correction:** As the name indicates, topographic correction is compensates for the topographical profile variations which can be solved by time-shifting of the data traces (Jol, 2009).
- **Trace difference:** consists of substracting consecutive traces. This allows to visualise the difference from one trace to the other, particularly favourable for dipping structures.
- **Background substraction:** useful technique to eliminate noises manifested in many traces. An average trace is calculated and it is substracted from each of them.

#### 4.3.1.5 Antenna orientation

The configuration of the antennas will aim for the maximum response of the GPR due to asymetries in the conductivity of the terrain. There is a maximum coupling of the signal if the electric field is along the maximum length of the object, hence the EM field will be absorbed by the object and its detection on the radargram will be poor. The most common antenna orientations are PL-BD (parallel broadside), PL-EF (parallel endfire), PR-BD (perpendicular broadside), PR-EF (perpendicular endfire) and XPOL (cross polarisation) (See Figure 4.13). For example, a buried pipeline will be hard to see using a PL-EF configuration if the direction of the survey is parallel to the axis of the pipeline. On the contrary, the same configuration with the direction of the survey perpendicular to the axis of the pipeline will clearly reveal a reflection. An exhaustive survey would include the repetition of the same lines with different antenna orientations with the aim of crosschecking if any object was missing on the radargrams due to EM coupling.

<sup>15</sup>In S&S referred as SEC2Gain, exponentially compensated gain (Sensors&Software, 1996).

<sup>16</sup>Deconvolution is just the inverse operation of a convolution. Convolution is defined as  $h = f * g = \int_{-\infty}^{\infty} f(\tau)g(\tau - x)d\tau$ . The purpose for deconvolution is, given  $h$  (raw GPR data), separate the  $f$  from the  $g$  (noise component) of the signal.



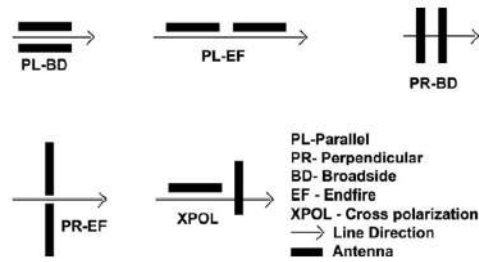


Figure 4.13: Most common antenna orientations in a GPR survey. The most used configuration for reflection surveys is the PR-BD (Perpendicular Broadside). Image Credit: © Sensors&Software from User Manual (Sensors&Software, 1996)

### 4.3.2 Main GPR Unit: PulseEKKO Pro

The PulseEKKO Pro is a GPR system manufactured by Sensors&Software™ that can be used for many different applications given the wide range of frequencies of its performance. This GPR, as its name indicates, is a pulsed-system, meaning that it radiates and receives echoes of EM pulses and represents the amplitude of the reflection as a function of time (Jol, 2009; Persico, 2014).

For this project, two different systems have been used, low-frequency and high-frequency<sup>17</sup>. The antennas of 50 MHz and 100 MHz have been chosen as low-frequency system due to its suitability for investigations in glaciology, geology and geotechnical surveys. The high-frequency system used is with the 900-450-250 MHz transducers<sup>18</sup> which are commonly used for the investigation of the different snow layers and the few first centimetres of the soil subsurface. Regardless of being a high or low-frequency system the four essential components of the pulseEKKO are the DVL (Digital Video Logger), the control module, the transmitting unit and the receiving unit (including antennas), the rest consists of the batteries and cables that connect the different components to each other. While it is possible to add a GPS device, for this project an independent GPS unit (InReach™) has been used.



(a) pulseEKKO 100 MHz on orange sledge. Image credit: M. Richter, UNIS student



(b) pulseEKKO 100 MHz on black sledge. Image credit: J. Jonas, UNIS student



(c) pulseEKKO 900 MHz on HF sledge. Image credit: J. Jonas, UNIS student

Figure 4.14: PulseEKKO 100 MHz system on two different sledge configurations: manual pulling (a), snowmobile towing (b). Note that due to extreme cold conditions the DVL battery is kept inside the snowmobile suit to provide the heat from the body. PulseEKKO HF system on sledge (c).

<sup>17</sup>The high frequency system could only be used during preliminary investigations before the WISDOM campaign. A malfunctioning DVL had to be replaced and the new one was incompatible with the old high-frequency system.

<sup>18</sup>Units that contain both the transmitter and receiver assembled together.

The combination of antennas, mobility configuration (sledge) and environment conditions have a direct effect on the choice of acquisition parameters of the GPR survey. For example, the sledge compartments only allowed for an antenna configuration of perpendicular-broadside (PR-BD). Table 4.3 presents the different configurations used for pulseEKKO. The choice of using a Free Run (continuous signal recording) for configurations 3 and 4 was due to the inability of using the odometer wheel after the failure and replacement for a newer DVL unit. In configuration 3 and 5 was necessary to leave a 2 m spacing between the antennas (Sensors&Software™ recommends to arrange them at a minimum distance of 1 m) due to signal coupling inside the sledge and subsequent clipping of the signal. This effect is very critical as it is hardware related (the system is saturated above the 50 mV threshold) and it simply cannot be removed via any processing, resulting in a *blinded* region in the radargram where clipping occurs.

Table 4.3: Acquisition parameters for different pulseEKKO configurations. Note in the last configuration the trace interval is given instead of step size as velocity was hard to keep constant.

	pulseEKKO system				
	config. 1 50 MHz	config 2. 900 MHz	config 3. 100 MHz	config 4. 100 MHz	config 5. 100 MHz
Antenna Separation [m]	2	0.17	2	1	2
Time window [ns]	1820	50	300	500	1200
Sampling Interval [ns]	1.6	0.1	0.4	0.4	0.8
Step Size [m] (Trace interval [s])	0.50	0.50	0.25	0.15	(0.3)
Num. Stacks	8	16	4	4	2
Trigger method	Odometer	Odometer	Free Run	Free Run	Free Run

### 4.3.3 Other GPR units

#### 4.3.3.1 WISDOM

*WISDOM*, *Water Ice Subsurface Deposits Observations on Mars*, is the GPR on ExoMars 2023 rover mission to Mars. It is designed to perform investigations on the first 3 meters of Mars' subsurface with a vertical resolution of just a few centimeters (Ciarletti et al., 2011). The purpose is to detect and characterise the structure and stratigraphy (eg. massive ice deposits, layers of sediments) of the subsurface and also to serve as guidance for the drilling operations to locations of interest and preventing operations in hazardous locations (Ciarletti et al., 2011; Dorizon et al., 2016; Hervé et al., 2020).

WISDOM is a step-frequency radar<sup>19</sup> operating at a frequency range between 0.5 and 3 GHz that transmits a series of continuous wave signals, each at a specific frequency during a time step of duration  $\Delta t$  (Ciarletti et al., 2011). The WISDOM instrument is divided into two subsystems (WISDOM-radar, 2022): the WISDOM Electronic Unit (WEU), which constitutes the frontend<sup>20</sup> for the GPR, and WISDOM antenna (WAA), which transmits and receives the signal generated by the WEU. The units are connected via four coaxial cables that transmit the signals. The WEU generates a sinusoidal signal at frequency  $f_1$  and it is emitted by the WAA as EM wave. The reflected waves are collected by the receiver part of the WAA. After  $\Delta t$  the WEU generates the next frequency ( $f_2$ ) and the process is repeated to the last frequency ( $f_n$ ) until the GPR frequency bandwidth  $B$  is covered, obtaining a single sounding or single acquisition (Dorizon et al., 2016; WISDOM-radar, 2022). After the data retrieval, an Inverse Fourier Transform (IFT) is applied to obtain the time-domain impulse response of each of the traces, originally in frequency-domain. Once transformed, the concatenated traces form a radargram, in which the time of reflections is related to their depth according to a velocity of propagation. This velocity is the key parameter to calculate the depth of the signal penetration as it is directly linked with the dielectric constant of the media. WISDOM provides two different methods to estimate the dielectric constant of the subsurface (Dorizon et al., 2016): based on the surface echo amplitude or based on the individual scatterer's typical signature by fitting the hyperbola on the radargram. The latter is commonly known

<sup>19</sup>A type of GPR that decomposes the EM pulse into spectral components and radiate them in a sequence, receiving trains of sinusoidal signals (Persico, 2014).

<sup>20</sup>Module that allows user interaction with the system.

among geophysicists and it is described in Section 4.3.1.3. The surface echo method, on the other hand, takes advantage from the fact that the antennas on the ExoMars rover are located approximately 37 cm above the surface which allows to disentangle the surface echo from the direct coupling between the antennas and therefore, it is possible to estimate<sup>21</sup> the dielectric constant of the surface layer (Dorizon et al., 2016).

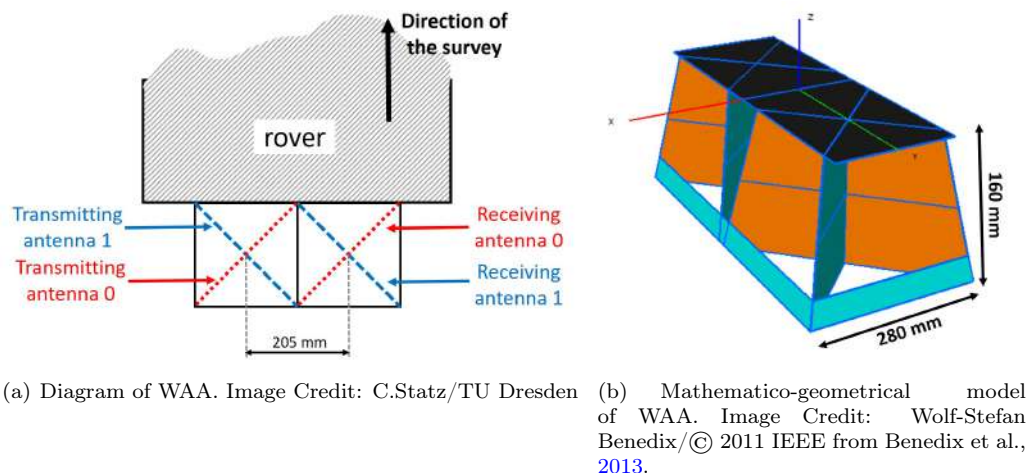


Figure 4.15: WISDOM antennas

WISDOM antennas have been specifically designed to meet the requirements of the ExoMars mission and deal with constraints posed by the rover structure and other systems. A compromised solution was found by designing two perpendicular oriented Vivaldi structures for each antenna, of about 20 cm x 20 cm x 20 cm in size and 200 g each (Plettmeier et al., 2009). The transmitting and receiving antennas are identical (fully-polarimetric GPR), it implies that for each single acquisition two antenna's elements are selected (one for transmission and the other for reception) and it is possible to record co-polarised or cross-polarised data. If the receiving antenna's radiating element is aligned with the transmitting antenna the configuration is co-polarised (0/0, 1/1), whereas if they are perpendicular it is on cross-polarisation mode (0/1, 1/0) (Dorizon et al., 2016) (see Figure 4.15.a). During the WISDOM Svalbard campaign 2022 single and full polarimetric measurements were retrieved. The latter meaning that all four possible combinations (0/0, 1/1, 0/1, 1/0) conform the totality of the data retrieved. This is considered different from signal *stacks* as they do not constitute only repeated GPR shots but have varying antenna configurations.

Table 4.4: WISDOM nominal parameters. Obtained from Table.2 in Dorizon et al., 2016

Central Frequency ( $f_0$ )	1.75 GHz
Frequency Bandwidth $B$	2.5 GHz
Step duration ( $\Delta t$ )	200 $\mu s$
Number of frequencies ( $N$ )	1001
Frequency step ( $\Delta f$ )	2.5 MHz
Radiated power ( $Pe$ )	16-19 dBm

Two versions of WISDOM have been tested during the field campaign: WISDOM prototype and WISDOM *FS2*, a flight spare model of the WISDOM on the ExoMars rover.

<sup>21</sup>The reader is referred to Dorizon et al., 2016 for a full description on the method depending on the roughness of the surface.

### WISDOM prototype

WISDOM prototype constitutes a copy that is representative in terms of size, mass, power and overall design to the WISDOM GPR. It consists of an electronic unit (EU), the antennas system and a laptop from which the GPR is commanded. During the fieldwork campaign the WISDOM prototype was operated on a cart specifically designed to host the EU and keep antennas at 37 cm above the ground. The cart has been either pulled manually or towed on a sledge by a snowmobile (see Figure 4.16). In the first case (manual), the WISDOM prototype has also been triggered manually using a trigger button. On the latter (snowmobile towing), the prototype has operated in *free run* mode or continuous recording.

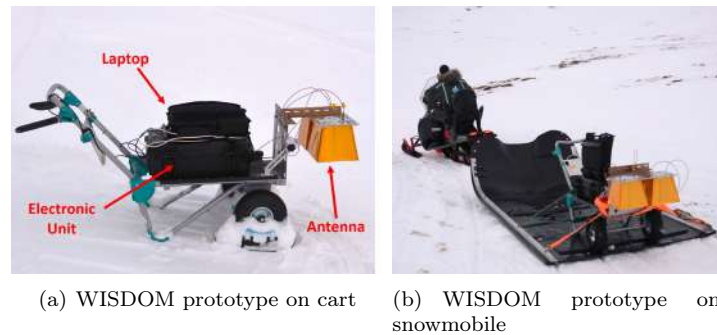


Figure 4.16: WISDOM prototype mobility configurations. Images credit: A.Le Gall, LATMOS.

### WISDOM FS2

WISDOM FS2 is a flight spare model of the WISDOM on the ExoMars rover. For the operations in Svalbard a special box was designed to protect the WEU from cold temperatures and harsh weather. The FS2 operations were carried out tossing the unit on a sledge with a snowmobile, on a rover-wheel frame and at an occasion, on the WISDOM prototype cart. As with the WISDOM prototype, antenna separation from the ground is always kept at 37 cm despite being far from optimal signal-wise, but emulating the same conditions as in the ExoMars rover.

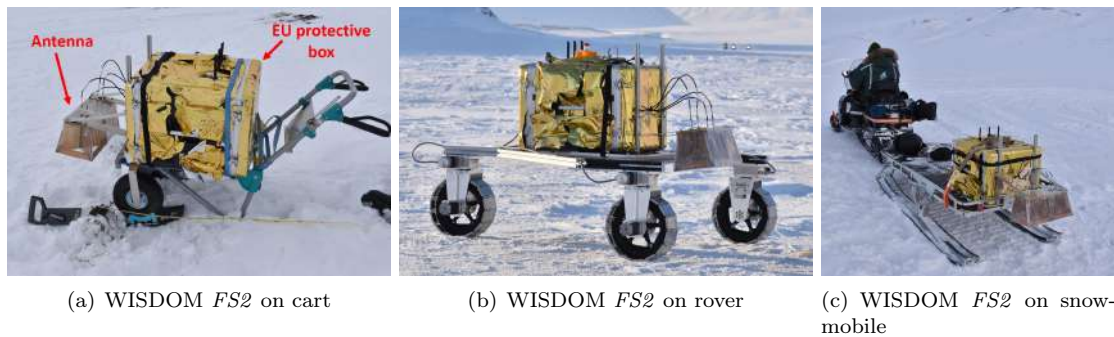


Figure 4.17: WISDOM FS2 mobility configurations. Images credit: W.S.Benedix, TU Dresden.

## 5. Results and Interpretation

This section presents the interpretation of the radar signatures given ground truth data (eg. environment contextualisation, snow conditions, ice cores, etc.) and aerial imagery as well as a 3D-GPR model to estimate wedge ice volume and distribution<sup>1</sup>. The pulseEKKO's profiles constitute the main radar survey whereas the WISDOM units provide complementary information. For the latter radargrams have only undergone preliminary processing and no topographic corrections.

The processing of B-scans has been implemented with *Sensors&Software Ekko Project V6* software while 3D maps and visualisations have relied on *GPRPy* (Plattner, 2021) and *Pyvista* (Sullivan and Kaszynski, 2019) Python Packages and *QGIS*. The calculation of the relative permittivity given salinity values was possible using *SMRT* (Picard and Sandells, 2022) Python package, a microwave radiative transfer model developed by ESA to investigate the representation of the snow microstructure<sup>2</sup>.

### 5.1 Site 1: Longyearbreen

#### 5.1.1 Glacier measurements

The first pulseEKKO measurements were taken on Longyearbreen during UNIS course AT-205. The glacier depth is being almost annually monitored with GPR recordings dating back to 2012<sup>3</sup>. A total of four parallel lines perpendicular to the axis of the glacier define the GPR profiles. Each line results in two profiles, one for the low frequency system and another for the high frequency one. The readings are carried out with the GPR towed by a bandwagon in a zig-zag fashion, in which the next starting point is separated 200 m from the previous endpoint.

The low frequency system (LF, 50MHz) is able to display the whole depth of the glacier, ca. 87 m calculated for a velocity of 0.168 m/ns, delineating the V-shaped boundary between the ice and the bedrock (see [Figure 5.2](#) from *a* to *d*). Profiles 1-3 show a reflection on the right hand side of the glacier that eventually absorbs the GPR energy and prevents from seeing below. It is not clear if this reflection originates from the presence of boulders and sediments (perhaps accumulated by a meltwater channel) or are the product of scattering of the signal due to irregularities on the bottom terrain.

The high frequency system (HF, 900MHz) gives a penetration of ca. 2 m and shows the boundary between the upper layer of snow and the ice. From historical data of the area, we know that in previous years two boundary layers were clearly identified: one between the newly accumulated snow and firn<sup>4</sup> and another one between firn and the glacier ice. No snow investigation was performed during the pulseEKKO survey but a first hypothesis is that the GPR detects the boundary layer between new snow and ice and that no firn is found. This would explain the rather quick loss of ice (around 10 m during one decade<sup>5</sup>) in Longyearbreen.

For each of the frequency systems a velocity in the media is deduced. For the LF system, a Kirchoff Migration gives best results of collapsed hyperbolas at 0.168 m/ns, which is in accordance with literature values<sup>6</sup>. The velocity on the HF system is assumed to be 0.21 m/ns based on previous investigations and literature values for polar snow. The actual velocity has been investigated from WISDOM *prototype* radargrams shown in the section below.

---

<sup>1</sup>Note: for consistency, profiles are displayed with the same color palette. However, in specific cases when other color combinations provide better contrast to visualise features the palette has been changed for clarity.

<sup>2</sup>More information can be found on <https://www.smrt-model.science/>

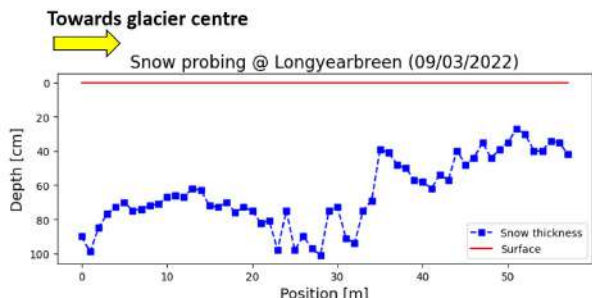
<sup>3</sup>Historical GPR data retrieved at former UNIS course AT-329 led by prof.J.S. Rønning.

<sup>4</sup>Intermediate state between snow and glacial ice. It forms after snow accumulates and compresses during several seasons eventually turning into compact ice.

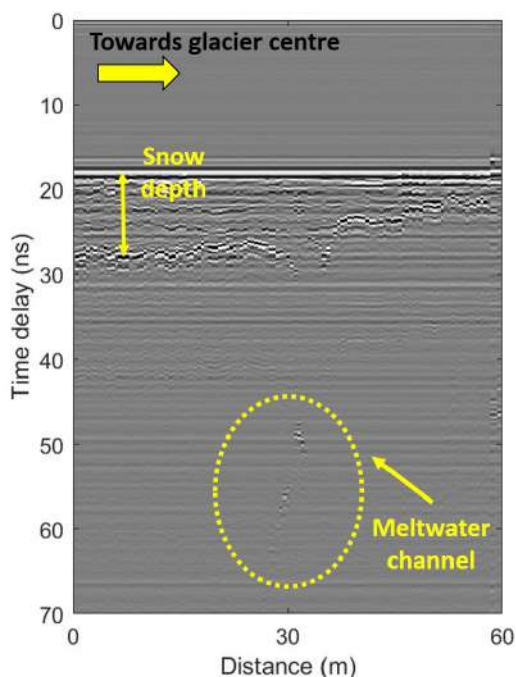
<sup>5</sup>From unpublished data courtesy of Prof.J.S. Rønning

<sup>6</sup>Eg. Reynolds, 2011

## 5.1.1.1 Snow investigation



(a) Snow probe measurements. Squares indicate the actual measurement while dashed lines a linear interpolation.



(b) Line 5 (WISDOMprototype). Spacing: 20 cm. Processing: free space removal. Single polarisation (0/0)

Figure 5.1: Snow-ice interface layer measurements by GPR and snow-probing. Note the correlation between the ground truth profile (a) and the GPR readings (b).

Figure 5.1.b shows the radargram recorded by the WISDOMprototype at the eastern side of Line 4, just at the edge of the glacier. The two main features detected are the snow-ice interface and a meltwater channel. The snow-ice interface was cross-checked in-situ with snow probe measurements at 1 m intervals and can be seen on Figure 5.1.a.

One feature that can be observed is that both GPR readings and ground truth measurements indicate the snow depth decreases as one approaches towards the center of the glacier (at least locally on the glacier edges). This behaviour cannot be appreciated on pulseEKKO profiles as they start about 50 m from the edges of the glacier (due to safety reasons as it was towed by a bandwagon) but agree with the general knowledge that the glacier surface is not flat but slightly convex. Another feature is the presence of a crevasse or most likely, a meltwater channel. Aerial imagery indicates the presence (in summer) of a meltwater channel in the boundary between the glacier and the rock. By observing the discontinuity on the snow-ice interface it is highly likely this corresponds to the deep reflection detected at 30 m distance.

Ground truth information combined with the radargram makes possible to estimate the actual velocity of signal propagation on the snow by simply dividing the depth by the travel time just as shown in Table 5.1 (it must be noted that the time is the TWTT, so to obtain the velocity one must divide it by a factor of 2),

$$v = \frac{d}{(t_f - t_i)/2}$$

where  $d$  is the depth and  $t_f, t_i$  the final and initial times respectively. One disadvantage is that the choice of initial time and final time is done manually (by observation of the radargram) and unavoidably, this has errors associated. For example, the velocity at position 12 m is extremely low while the one at position 57 m is above threshold values. The more measurements the more outliers can be flattened out. Nevertheless, the average velocity

obtained for the snow investigations of Longyearbreen is of 0.219 m/ns, which is in accordance with the values for polar snow (Table 4.2.) and confirms the value proposed in the previous section.

Table 5.1: Snow depth and travel times for WISDOM<sub>prototype</sub> Line 4 (selected every 5 m). The initial time corresponds to the starting of the snow surface. The final time is the time at which the snow-ice interface is seen. Note that between positions 32 m and 37 m has been not possible to associate any time as it is not possible to see the snow-ice interface layer.

Pos. [m]	Snow Depth [cm]	Initial Time [ns]	Final Time [ns]	Time diff. [ns]	Calc Vel [m/ns]
2	85	18.700	27.300	8.600	0.1977
7	74	19.100	27.500	8.400	0.1762
12	67	19.200	27.500	8.300	0.1614
17	70	18.900	26.630	7.730	0.1811
22	81	19.100	27.030	7.930	0.2043
27	97	18.500	26.833	8.333	0.2328
32	94	-	-	-	-
37	48	-	-	-	-
42	54	19.200	23.600	4.400	0.2455
47	35	19.100	21.933	2.833	0.2471
52	30	19.000	21.333	2.333	0.2572
57	42	18.500	21.433	2.933	0.2864
<b>Average</b>					0.2190
<b>Std. Dev</b>					0.0407

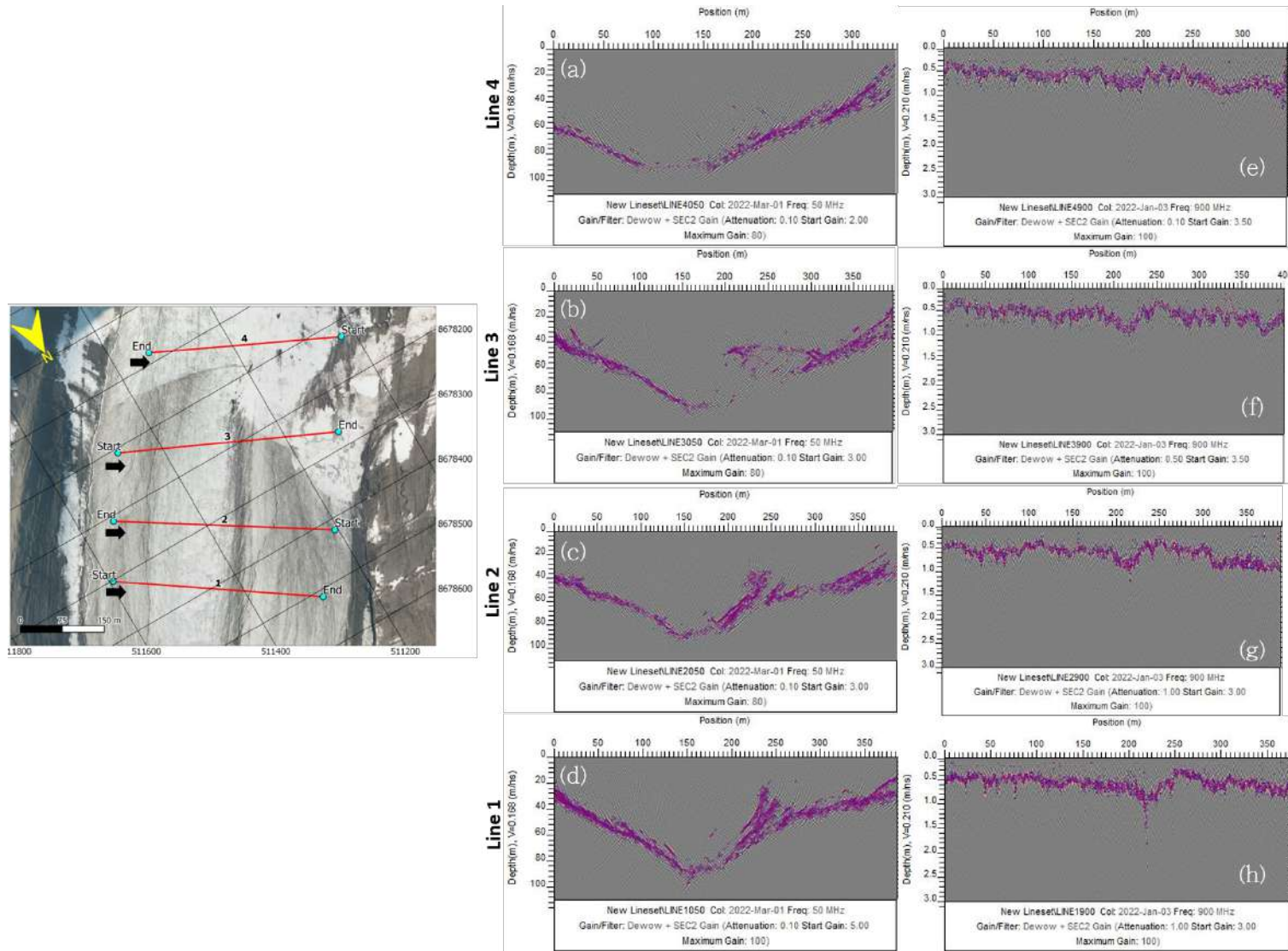


Figure 5.2: Location and GPR profiles on Longyearbreen. The map on the left shows how profiles 1 and 3 have been retrieved from left to right while 2 and 4 from right to left. The latter ones have been flipped so all can be compared. Images from (a) to (d) show the 50 MHz profiles (config. 1). Processing: Dewow + Trace reposition + Background Subtraction + Kirchoff Migration according to hyperbola fitting;  $0.168 \text{ m/ns}$  + SEC2Gain. Images from (e) to (h) show the 900 MHz profiles (config. 2). Processing: Dewow + Trace reposition + Background Subtraction + SEC2Gain. Note in image (d) at position ca. 210 m a reflection penetrates deeper than the rest. It could be an indication of a crack in the ice filled with snow. Furthermore, it is found approximately at the same position that the reflector on image (d). Background map: © Norwegian Polar Institute/CC BY 4.0



### 5.1.2 Ice Cave

A total of 3 lines profiled by pulseEKKO have been selected. The WISDOM*prototype* recorded a small grid of three 15 m-parallel lines (spaced by 3 m) and one perpendicular. However, GPS tracks had very low accuracy and the exact locations could not be recovered. Approximately, the first line of WISDOM*prototype* is contained within *Line 1* of pulseEKKO, starting about 8 m from the origin. As [Figure 5.3](#), also several points belonging to the "ice cave" (rather walkable meltwater channel) were marked on the surface. At two of the recorded points a metal plate was left on the cave-bottom<sup>7</sup> in order to see the reflectors on the radargram and be able to recognise the exact location.

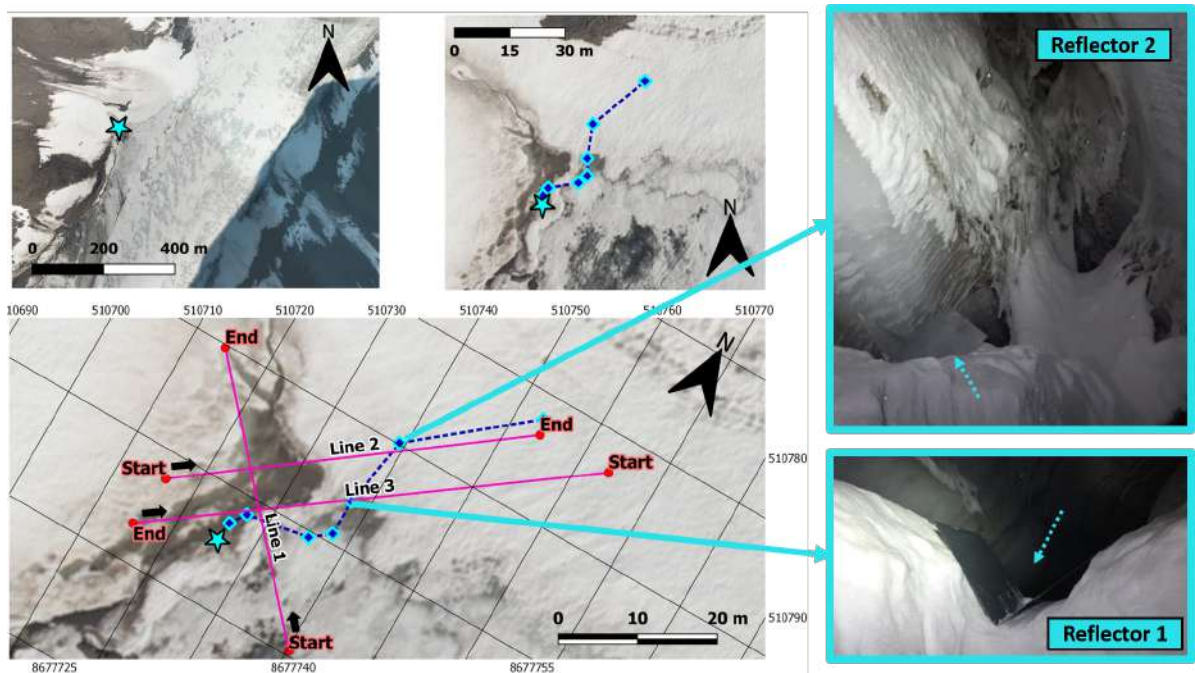


Figure 5.3: Ice Cave profile lines. The dark blue dashed line indicates the cave meandering. As the figure indicates, at two of these points metal reflectors (metal plates of 30 cm by 60 cm bend in half) were positioned to trigger the GPR signal. Background map: © Norwegian Polar Institute/CC BY 4.0

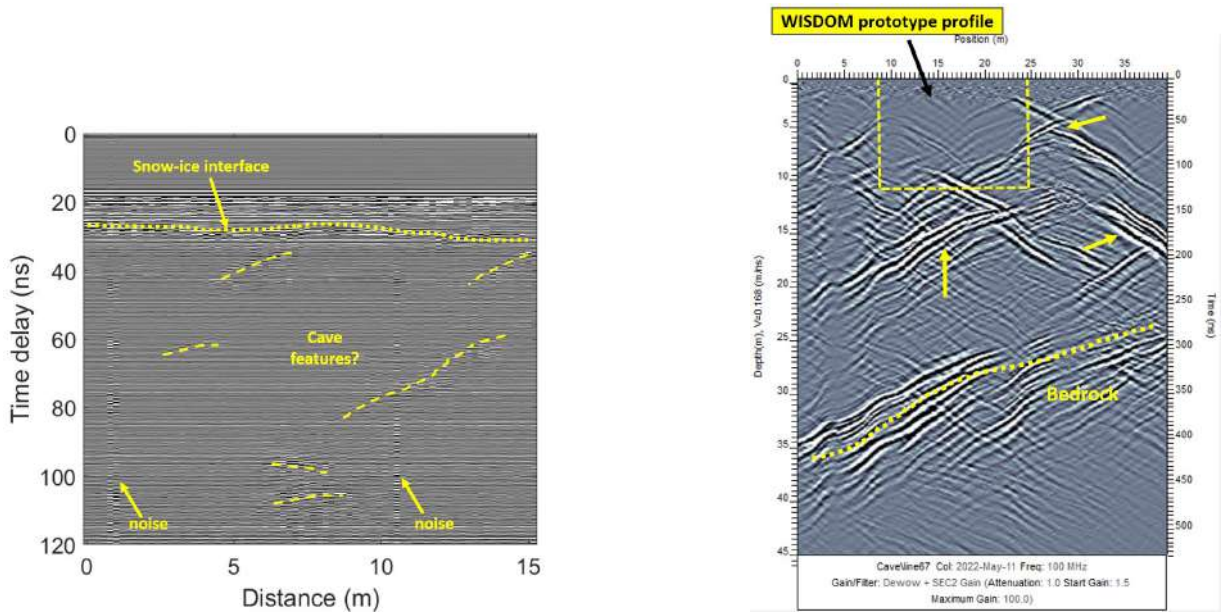
The results on the ice cave have been quite surprising, as cave features have proven to be much more difficult to interpret than expected and reflectors could not be identified. The most clear and unequivocal feature detected by pulseEKKO is the interface between the glacier ice and the bedrock bottom. Aside that the GPR does not detect any features beyond that depth -meaning to have reached the bottom of the glacier- the ice-rock interface is flat for lines parallel to the axis of the glacier (*Line 2* and *Line 3*) and shows an uphill slope when approaching the edge of the glacier (*Line 1*). The many hyperbolic reflections between depths 10-15 m ([Figure 5.4](#) from *b* to *d*, marked with yellow arrows), most probably belong to the cave. The depth seems reasonable, being at least 10 m below the surface level. However, there are many features of the cave that can trigger a strong GPR response, such as boulders trapped in the ice that may act as point reflectors, the change of media when signal enters the cave (from ice to air) and leaving the cave (from air to ice), sharp edged-ice formations, making it difficult to attribute to which one. The long reflectors suggest the change in media while clusters of hyperbolas seem more plausible to correlate with boulders trapped in the ice (see [Figure 5.4.c](#)).

WISDOM*prototype* line shows a more detailed of the first meters. Assuming the profile has been well adjusted relative to pulseEKKO's line, WISDOM unit would be detecting the roof features of the ice

<sup>7</sup>They were left about 3 m above the actual bottom of the cave as there were visitors and the path is very narrow.

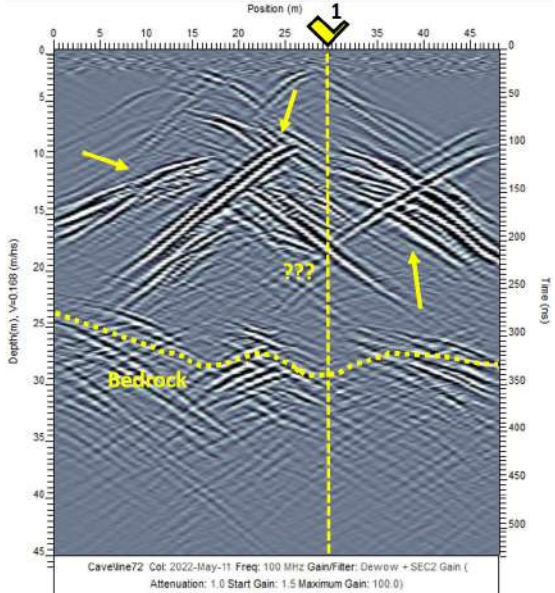
cave. The lack of hyperbolic reflections and the direct observation of the first meters of cave suggest these reflections would be caused by the ice walls or ice shapes. It must be added that the depth at which the pulseEKKO unit finds the cave features should be about 1 m lower as there was an extra meter of snow accumulated between surveys.

On the other hand, [Figure 5.4.c](#) and [Figure 5.4.d](#) show how there is no correlation with the location of the reflector and the radargram signal. The most probable explanation for this is the following: the locations for the reflectors on the map might be not exactly the true reflector positions. To locate the reflectors inside the cave, we followed this strategy: one person entered the cave with an avalanche beacon in transmitter mode while the person above used their own beacon as receiver and searched for the person inside the cave until constant target distance was achieved. The different points on the cave in [Figure 5.3](#) were obtained in this fashion. Needless to say, these methodology is far from accurate and errors of a few meters are expected. So, despite the GPR profile surveying above the cave points according the to GPS, the actual reflectors might have been a few meters off and hence out of range.

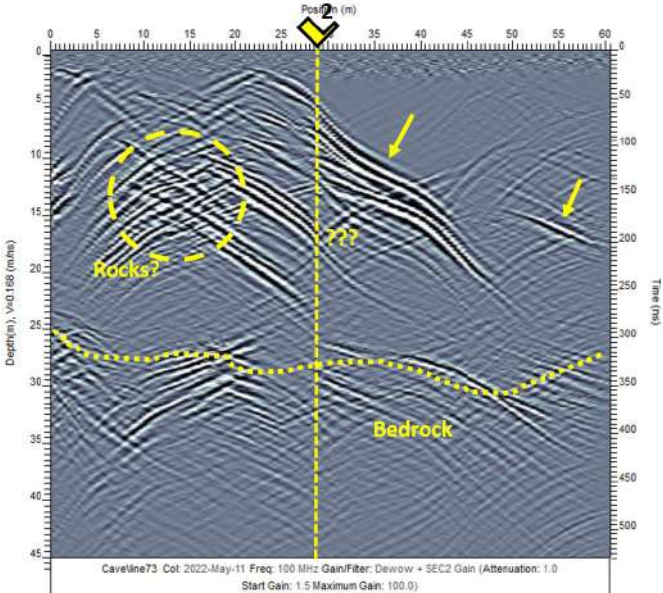


(a) First profile line from WISDOM *prototype* grid (same direction as *Line 1*). Processing: Free Space removal

(b) *Line 1* profile by pulseEKKO (config. 5). Processing: Dewow + Trace reposition (GPS) + Background subtraction + SEC2Gain



(c) *Line 2* profile by pulseEKKO (config. 5). Processing: Dewow + Trace reposition (GPS) + Background subtraction + SEC2Gain



(d) *Line 3* profile by pulseEKKO (note this profile has been flipped and it is presented in the direction of the black arrow of Figure 5.3 (config. 5). Processing: Dewow + Trace reposition (GPS) + Background subtraction + SEC2Gain

Figure 5.4: Ice cave radargrams. Note that the pulseEKKO reflections have a wobbling effect. This is due to changes in velocity of the snowmobile that deform the hyperbolas. This effect provokes Kirchoff Migration to not collapse properly hyperbolas into points, for this reason, this processing step has avoided.

## 5.2 Site 2: Innerhytta Pingo

A total of four GPR profiles are analysed at Innerhytta pingo: *Line 1*, *Line 2*, *Line 3* and *Line 4*. *Line 1* has been made by WISDOMfs2 and traverses Innerhytta northern flank from the North-East to the South-West, with a total length of 520 m. *Line 2* was recorded by pulseEKKo and shares the same path with *Line 1* up to about 350 m. At that point, due to difficulties in following the original path of WISDOMfs2 with the snowmobile-sledge system, the path diverges to eventually reunite at its ending point. *Line 3* presents a loop starting approximately at 350 m from the starting point with a total length of 130 m. *Line 4* is located on a hilly region on the southern flank of Innerhytta. It has been profiled by only WISDOMproto on the cart due to difficult terrain.

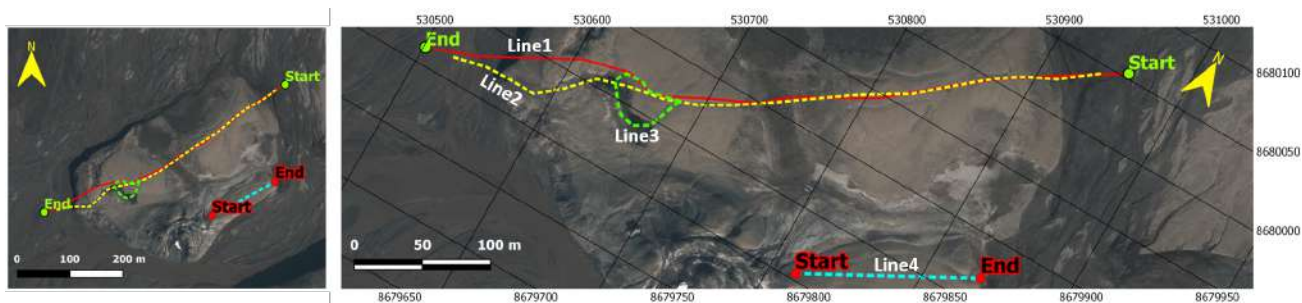


Figure 5.5: Profile lines at Innerhytta Pingo. *Line 1* by WISDOMfs2, *Lines 2* and *3* by pulseEkko and *Line 4* by WISDOMprototype. Background map: © Norwegian Polar Institute/CC BY 4.0

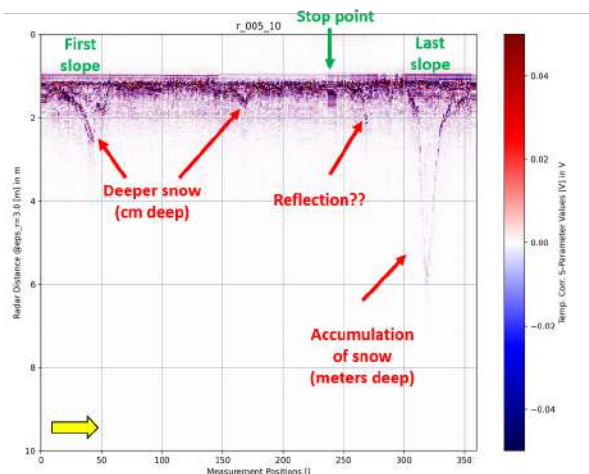
Figure 5.7.a corresponds to *Line 2* with a total length of 490 m. The line is characterised by 4 different features which have been marked in yellow. The first and last reflections (at 35 m and 480 m, respectively) are artificially created when climbing up or down prominent slopes of the pingo. In particular, the last slope had not only several meters of accumulated snow but also is located on a steep area with the presence of snow cornices which causes stronger reflections (see Section 5.3.1 for a detailed explanation). Between 35 m until 310 m no features are appreciated except for the spontaneous appearance of hyperbolas very close to the surface (eg. at 190 m). These correspond to several-cm sized stones exposed on the pingo surface that triggered the GPR response. The lack of signal penetration is attributed to the abundance of shales and sediments present, at least on the upper layers, which cause a strong signal attenuation and prevent the GPR from reaching further depths. The remaining features are condensed between the positions 310 m and 410 m. The clearest feature is comprised between 360 m and 410 m reaching a depth of 15 m. The region presents very strong reflectors while showing layered structures. For this reason a loop around this area of interest was performed (*Line 3*) in the search of deeper GPR penetration.

Figure 5.8.b shows two distinctive features with reflections up to 15 m depth that present a rather uneven layering and display partial hyperbolic shapes. An hyperbolic shape on the region labelled as 2 has been used to determine the propagation velocity, obtaining  $v = 0.143 \text{ m/ns}$ . This velocity has been used across all the profile but in fact, it is only valid for the high-penetration regions and not the shale-sediments ones. Notice that targets marked with 1 and 2 completely correlate with the darker regions in the aerial image (Figure 5.8.a). In fact, the aerial image has been taken on summer time and this dark areas correspond to small ponds of liquid water which would match with our findings, as it would be frozen by the time of our survey. By the difference in penetration depth the presence of ice-rich structures is certain. However, to establish the cause of this uneven layering is quite more difficult. Comparing these GPR responses to the ice crust investigations at River Bed Pingo (see Section 5.4.2) seems plausible to assume this ice-rich structures are not massive ice with defined layering, but rather a mix of ice and sediments, thus, supporting the ice-shale alternations hypotheses.

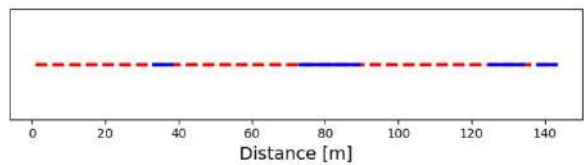
At 310 m (Figure 5.7) the GPR reflections are divided into two distinctive features, one about 10 m depth and a bigger cluster closer to the surface up to 5 m depth. Looking into the aerial photographs it is possible to establish a correlation between the location of these reflections and a stream-like carving on the surface. Nevertheless, the GPR profile goes through other stream-like features that produce no reflection so it might be more relevant the fact of being close to the small ponds area. Unlike targets 1 and 2 in *Line 3*, the feature layering at 310 m is discontinuous with depth. This might suggest homogeneity on the ice composition until a depth of 10 m but cannot explain why it is an isolated feature with no continuity backwards or forwards along the *Line 2* profile. The close proximity of all GPR strong reflections combined with the presence of liquid water according to aerial imagery strongly suggests the detection of Innerhytta’s ice core. However, any statement regarding the nature of the ice layering or changes in its composition cannot be ascertained without ground truth data.

Figure 5.6.a displays *Line 1*. At WISDOM high frequencies no relevant feature can be appreciated. The initial and final slopes are seen in detail, in particular the GPR is able to distinguish a snow-soil interface. About the measurement position 270 (approximately 405 m) there is a faint reflection which could correspond to the ice layered features registered by the pulseEkko unit.

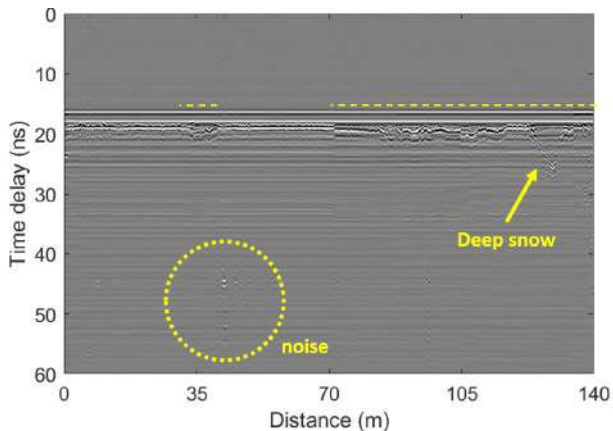
Figure 5.6.c shows *Line 4*. WISDOMprototype unit is not able to see any feature related to the pingo below the surface as the presence of shales attenuate the signal too greatly. What it can be seen is the snow-soil interface and also the surface echo signature. At position 130 m it is possible to see a deep plunge of the snow-soil interface. This was measured to be around 80 cm verifying the sudden, local increase in snow depth indicated by the GPR unit. Information about the soil conditions was gathered in order to understand the system responses caused by different media on the surface. The diagram on Figure 5.6.b shows two different types of features on the surface: snow or exposed soil. For the first half of the profile, it can be observed that the exposed soil (no snow or ice) causes a steady reflection while going over snow results in a noisier response. On the second half of the profile this noisy effect on the surface appears on both snow and exposed soil regions, indicating that both media might trigger similar reflections. An hypothesis is that a region with exposed soil but with medium-sized pebbles will cause the signal to reflect irregularly, imitating the response of the GPR when it goes over a snow-covered area.



(a) *Line 1* profile by WISDOMfs2 unit, single polarisation (0/0). Note the x-axis is on measurement positions, not distance. The positions have been triggered at 1.5 m spacings. The y-axis (depth) is indicated in meters assuming  $\epsilon_r = 3$ , which according to equation 4.8 corresponds to a  $v = 0.173$  m/ns.

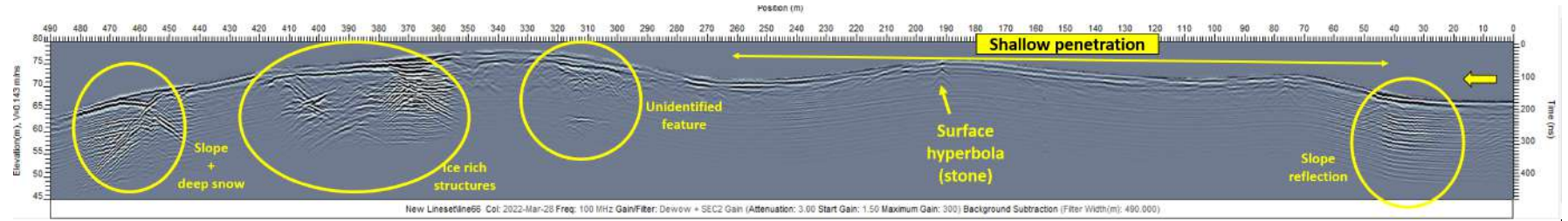


(b) Surface features on *Line 4*. Blue for snow and red for exposed soil



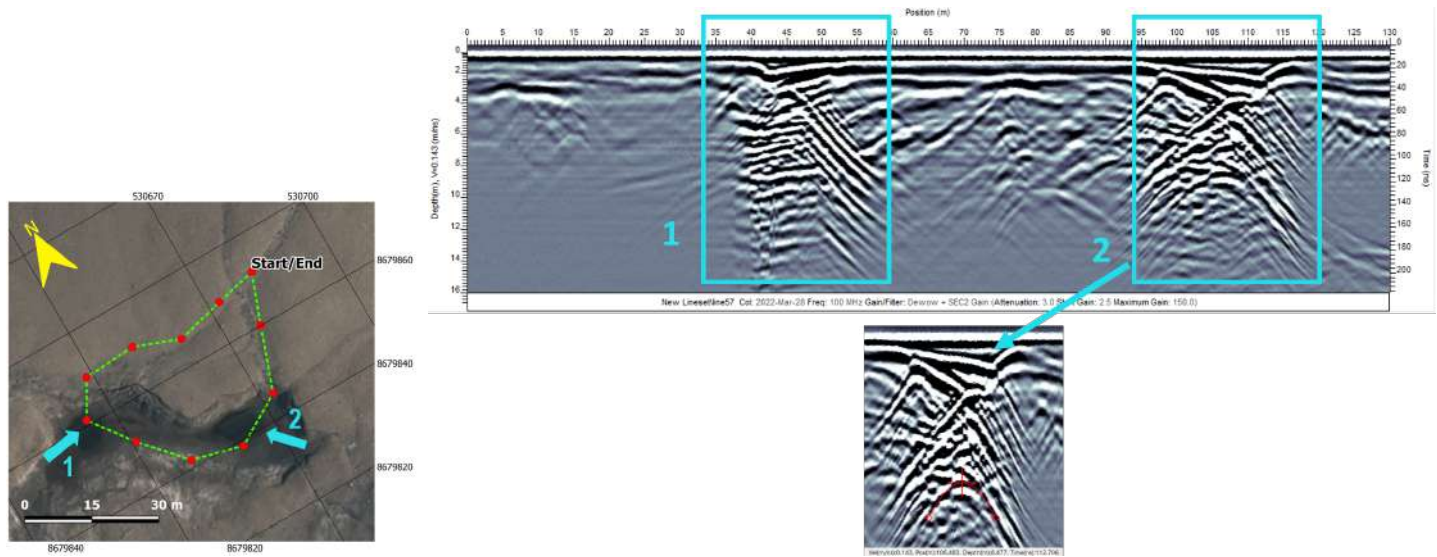
(c) *Line 4* profile by WISDOMprototype unit (single polarisation, 0/0). Dashed lines mark a different type of response on the surface. Spacing: 20 cm. Processing: FreeSpace removal

Figure 5.6



(a) Line 2 profile (pulseEKKO, config. 3). Processing: Dewow + Background Subtraction + SEC2 Gain + Topography correction. Depth adjusted for propagation velocity of 0.143 m/ns (hyperbola fitting). The yellow arrow indicates the direction of GPR data retrieval. Background map: © Norwegian Polar Institute/CC BY 4.0

Figure 5.7



(a) Line 3 close-up

(b) Line 3 profile (config. 3). Processing: Dewow + SEC2 Gain. On the bottom: close-up of target 2 for hyperbola fitting ( $v = 0.143 \text{ m/ns}$ )

Figure 5.8: Loop profile targeting pingo features. Note the correlation between the features marked on the aerial image (a) and the GPR response (b).

## 5.3 Site 3: Helvetidalen

### 5.3.1 Alluvial Fan

A total of one line has been analysed in the alluvial fan located at the entrance of Adventdalen-Helvetidalen. The same line generates two different profiles, Profile 1 (from East to West) and Profile 2 (from West to East). The repetition of the same line in both directions helps to distinguish between real and artificial features on the radargram.

Figure 5.11.a and Figure 5.11.b show the GPR profiles of the alluvial fan forth and back respectively. It can be seen that both profiles show the same features at the same locations (a few meter variation is due to the fact that the profiles do not have exactly the same length). Observing the profile from left to right, first there is a gentle slope that starts at an elevation of 110 m and concludes at 85 m. The penetration is rather shallow (5 m) but it is possible to observe soil layering which is associated to the layer deposition of a smaller alluvial fan that feeds the main one. At the end of the slope there is a strong reflector caused by the slope itself. A flat area of approximately 70 m in length corresponds to the mouth of the main alluvial fan. The GPR unit detects different layering and also the bottom sediment layer that as an open U-shape characteristic of river beds. The last feature is found at the beginning of the slope and it is distinguished by strong reflectors. These reflectors are not only caused artificially by the reflection of the signal on the slope but also a snow cornice formation buried on the snow. Figure 5.10.a shows a conceptual diagram compared to the actual snow formation at the slope of the alluvial fan. It can be seen that the regions with a greater height difference a snow cornice is formed, clearly displaying a cavity and a snow pillow below. As the height decreases and the slope is more gentle the two snow layers eventually touch each other and if any cavity remains, it is buried under a layer of new snow. Figure 5.10.b and Figure 5.10.c show more in detail the strong reflection at the slope and hint a connection point between the upper and lower snow layers that form the snow cornice.

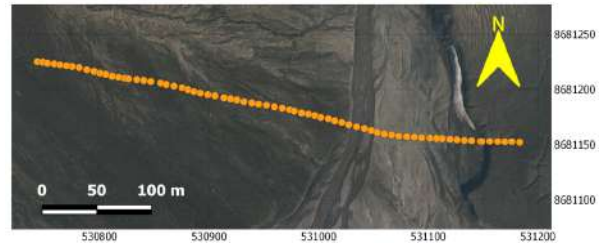


Figure 5.9: Profile line at Alluvial Fan. Background map: © Norwegian Polar Institute/CC BY 4.0

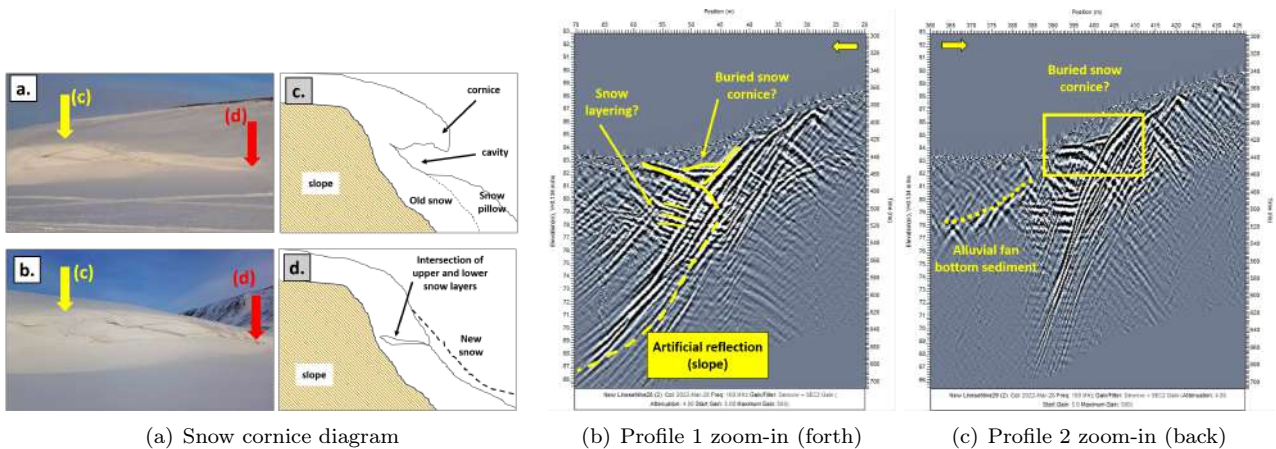
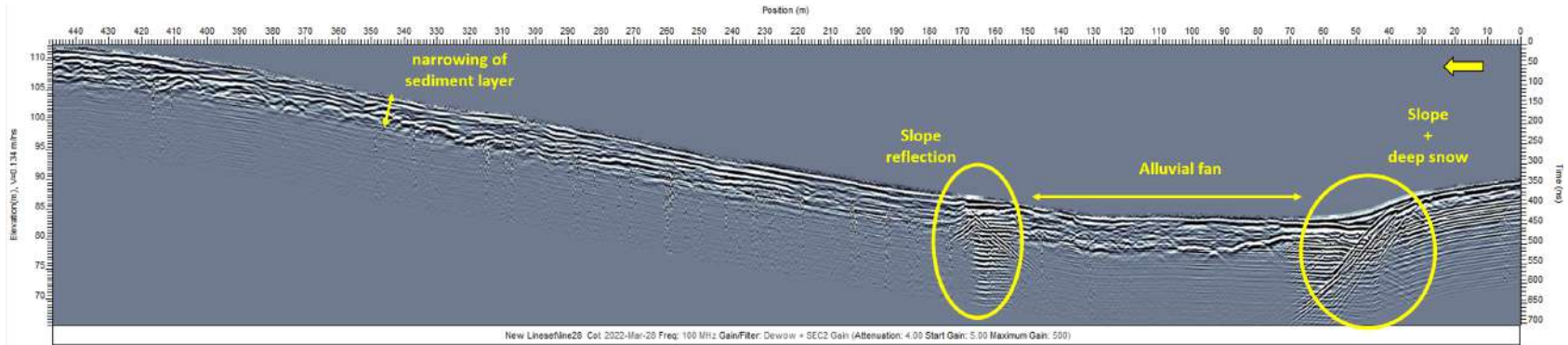
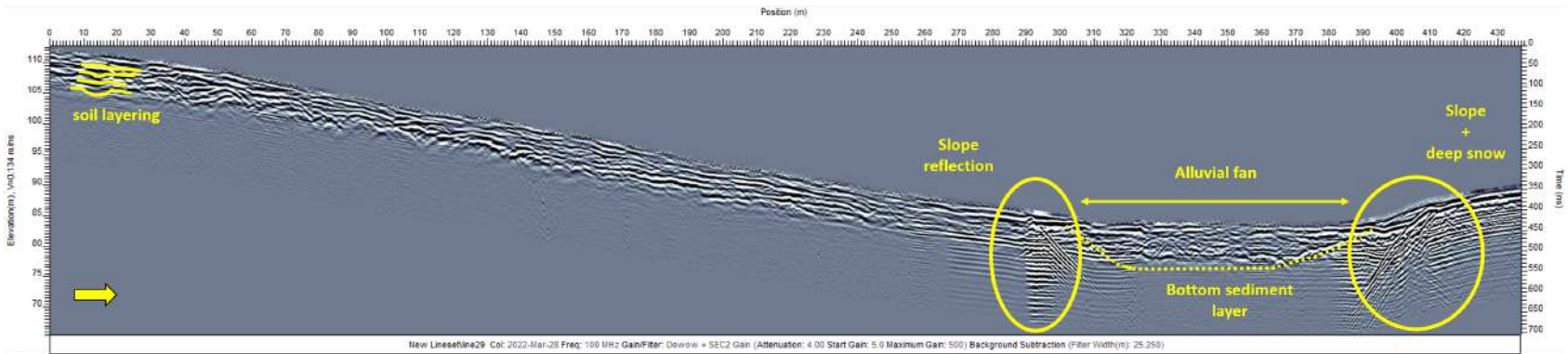


Figure 5.10: GPR visualisation of deep snow accumulation



(a) Profile 1. Forward direction (pulseEKKO, config. 3). Processing: Dewow + Background Substraction + SEC2Gain + Topography Correction. Velocity propagation at 0.134 m/ns



(b) Profile 2. Backwards direction (pulseEKKO, config. 3). Processing: Dewow + Background Substraction + SEC2Gain + Topography Correction. Velocity propagation at 0.134 m/ns

Figure 5.11: Alluvial fan GPR profiles. Note the yellow arrow indicates the direction in which data was retrieved.



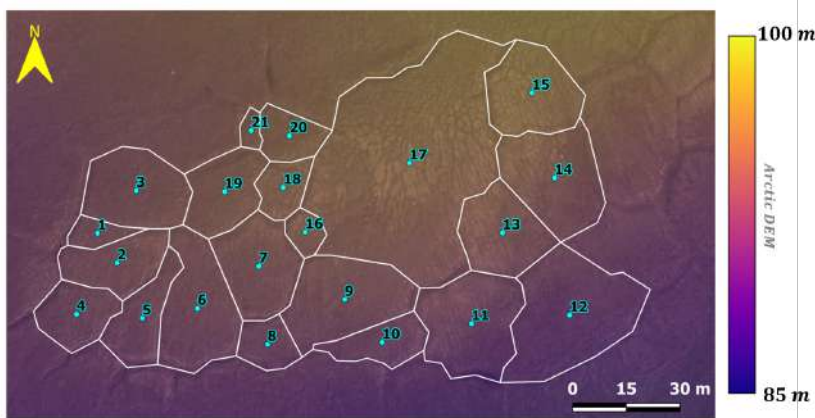
## 5.3.2 Ice Wedge Polygons

### 5.3.2.1 Geomorphology of polygons

The polygon network studied at Site 3 is located on an elevated terrain at the entrance of Helvetidalen connecting to Adventdalen valley. It consists of a subset of a total of 21 polygons (see Figure 5.12), characterised by irregular shapes and variability on polygon size covering an area of  $19.8 \cdot 10^3 m^2$ . A detailed description of the polygon parameters is given on Table 5.3 following the criteria of Section 4.2.1. Variation in polygon size is clearly depicted by observing the polygon area, the minimum being at  $55.4 m^2$  while the maximum up to  $2627.2 m^2$  and a standard deviation around 10 times the minimum value. The irregularity in shape (elongated vs. circular) is less accentuated despite still showing relevant differences in values, such as a minimum aspect ratio of 0.32 while the average being 0.61, twice the minimum.



(a) Ice Wedge polygons, aerial image



(b) Manually delineated polygons with enumerated centroids. The color palette shows the DEM.

Figure 5.12: Ice wedge polygons at Site 3. Background map: © Norwegian Polar Institute/CC BY 4.0

polygons with sharp, *unpolished* edges. The extremely concave polygons are non-existent in Site 3 sample (and seldomly found in polygon networks, if found at all) but the latter are fairly common, eg. polygons 1, 4, 6 and 10. Taking polygon 10 for further analysis, Table 5.2 presents the results by calculating the polygon axis by the two approaches. Just as Figure 5.13 illustrates, the long axis resulting values are

As the subset constitutes a small subsample of region AD 2 from Ulrich, 2011, results from both studies have been compared to each other. Size parameters ( $A$ ,  $P$  and  $D$  and  $L$ ) indicate that Site 3 polygon network is a slightly smaller subsample of AD 2, with average values being the most dissimilar amongst them. This indicates that Site 3 smallest and largest polygons approach to represent the minimum and maximum values for AD 2 but not so accurately the rest of the polygon sample.

On the other hand, shape parameters ( $C$ ,  $AR$ ) as well as short axis ( $S$ ) show the opposite behaviour in which either the minimum or maximum values are more inconsistent with AD 2 than the average. In particular,  $S$  shows the highest discrepancies of all parameters. In fact, results from  $S$  do not correctly describe how the subsample compares to the AD 2 region because a bias is introduced as the axis lengths are not calculated with the same criteria (see Section 4.2.1). The problem originates when calculating the axis for extremely concave polygons and elongated poly-

virtually the same by either method but the bounding rectangle overestimates the short axis. Thus, the combination of an already smaller-sized sample with a method that computes a smaller  $S$  triggers the discrepancies on this parameter.

$C$  and  $AR$  are derived-parameters, so, they are more difficult to interpret in terms of relative error. Observing the results directly on Table 5.3, one can see that  $AR$  relative error drops respect to  $S$  eventually being similar to those of  $L$  and virtually having the same error for minimum, maximum and average values. Seems it can be concluded that despite the differences in methodologies and larger discrepancies in  $S$ , the errors compensate for the shape parameter. In addition,  $AD \approx AR$  is the value with more extremes while  $C$  is more conservative. In the current study, the lowest minimum value corresponds to the  $AR$  but the maximum to the  $C$ . These lower upper bound of the  $AR$  might be as well linked to the methodology to calculate the polygon axis.

Overall, Site 3 polygon network has similar shape to AD2 and is slightly smaller.

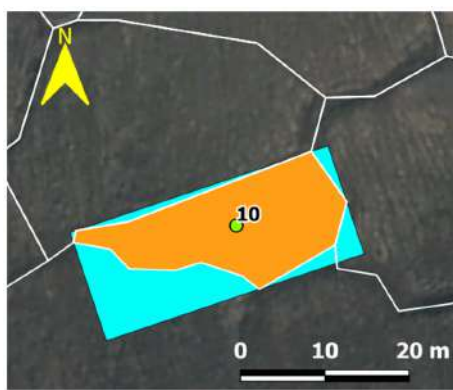


Figure 5.13: Polygon 10 inside minimum bounding polygon. Background map: © Norwegian Polar Institute/CC BY 4.0

	Polygon 10	
	Long Axis [m]	Short Axis [m]
<b>True polygon axis</b>	32.2	11.1
<b>Minimum Bounding Rectangle</b>	32.3	13.5
<b>Rel. Error</b>	0.41%	18.12%

Table 5.2: Axis values for polygon 10 applying different methods.

Figure 5.14 shows the correlation matrix between two polygon geomorphometric parameters, diameter (size) and aspect ratio (shape) and the geographical data of the polygon's centroids. The aim of this plot is to unveil correlations, if any, between apparently independent variables. For example, if the size of the polygon changes with elevation or if northern polygons display a more elongated shape than the southern counterparts. The correlation matrix shows that there is no relation between the geomorphometric parameters and the geographical ones. This is within the expected results as the subset of the study only comprises polygons in a space of roughly 180 m from East to West and 100 m from North to South, a fairly small area to observe any geographical trend. The only correlation found, as expected due to the north-south slope, is between two geographical variables, the centroid Northings ( $Y$ ) and the elevation. This result can be also observed directly on Figure 5.12.b in which clearly, centroids of higher latitudes have a shade of yellow while those to the South a rather blueish one, marking the higher and lower elevations respectively.

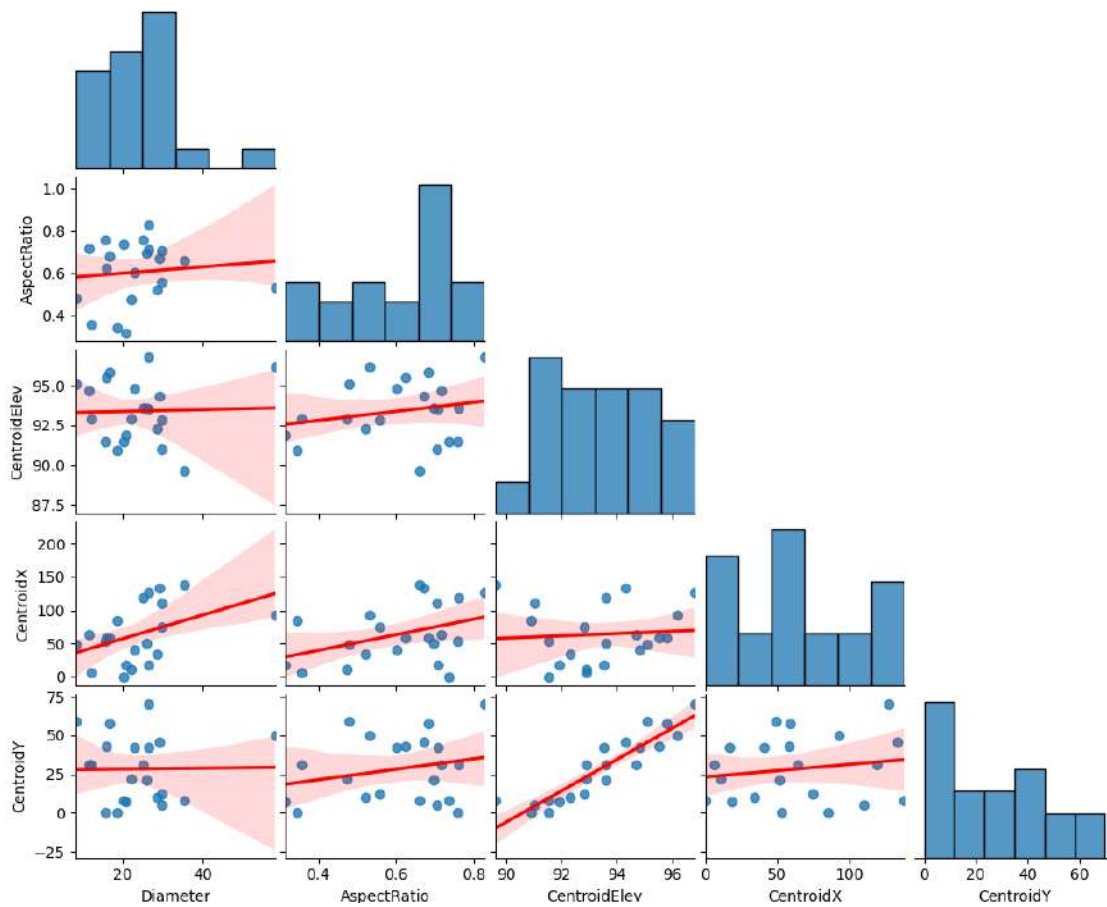


Figure 5.14: Correlation matrix of ice-wedge polygons geometrical parameters. Plotted with *Python Seaborn* module. Note that *Centroid X* and *Centroid Y* variables have been recalculated by subtracting the minimum X and Y coordinates, respectively. This has been done to avoid large numbers on the plot's axis.

Table 5.3: Geometrical and statistical parameters of ice-wedge polygons in Site 3. The second box corresponds to the values obtained in Ulrich, 2011 (Table 3.2) for region *AD 2* and third box is the relative error between each statistical parameter result (min., max., average) of this project using *AD 2* as reference

Polygon ID	Area (A) [ $m^2$ ]	Perimeter (P) [ $m$ ]	Diameter (D) [ $m$ ]	Long Axis (L) [ $m$ ]	Short Axis (S) [ $m$ ]	Circularity (C)	Aspect Ratio (AR)	Centroid Elev. [ $m$ ]	Centroid X (UTM 33) [ $m$ ]	Centroid Y (UTM 33) [ $m$ ]
1	115.0	52.8	12.1	22.7	8.1	0.52	0.36	92.9	531211	8681136
2	383.5	85.0	22.1	31.2	14.8	0.67	0.47	92.9	531216	8681127
3	553.1	88.8	26.5	31.2	22.1	0.88	0.71	93.5	531222	8681147
4	321.6	69.1	20.2	24.6	18.1	0.85	0.74	91.5	531205	8681113
5	341.4	90.8	20.8	35.8	11.3	0.52	0.32	91.9	531223	8681112
6	648.9	111.6	28.7	39.7	20.6	0.65	0.52	92.3	531239	8681115
7	529.0	90.2	26.0	31.0	21.6	0.82	0.70	93.6	531256	8681126
8	195.1	54.6	15.8	18.3	13.9	0.82	0.76	91.5	531258	8681105
9	686.2	107.4	29.6	39.7	22.1	0.75	0.56	92.8	531280	8681117
10	269.7	78.1	18.5	32.2	11.1	0.56	0.34	90.9	531290	8681105
11	694.4	107.0	29.7	34.4	24.3	0.76	0.71	91.0	531315	8681110
12	977.6	131.7	35.3	45.0	29.7	0.71	0.66	89.6	531343	8681113
13	492.9	86.3	25.1	28.9	22.0	0.83	0.76	93.6	531324	8681136
14	669.7	104.1	29.2	35.6	23.9	0.78	0.67	94.3	531338	8681151
15	547.1	88.7	26.4	29.3	24.3	0.87	0.83	96.8	531332	8681175
16	107.9	39.1	11.7	14.0	10.0	0.89	0.72	94.7	531269	8681136
17	2627.2	233.7	57.8	80.5	42.8	0.60	0.53	96.2	531298	8681155
18	196.7	57.3	15.8	21.7	13.5	0.75	0.62	95.5	531263	8681148
19	411.4	82.5	22.9	30.0	18.0	0.76	0.60	94.8	531246	8681147
20	222.4	59.5	16.8	19.9	13.6	0.79	0.68	95.8	531264	8681163
21	55.4	30.9	8.4	11.4	5.5	0.73	0.48	95.1	531254	8681164
<b>Min.</b>	55.4	30.9	8.4	11.4	5.5	0.52	0.32	89.642		
<b>Max.</b>	2627.2	233.7	57.8	80.5	42.8	0.89	0.83	96.813		
<b>Average</b>	526.0	88.1	23.8	31.3	18.6	0.74	0.61	93.398		
<b>Std. Dev</b>	536.7	41.8	10.4	14.2	8.4	0.11	0.15	1.928		
<b>Ulrich 2011 (AD2)</b>										
<b>Min.</b>	69.7	35.2	9.4	13.3	10.2	0.47	0.37			
<b>Max.</b>	3328.6	245.5	65.1	96.2	79.4	0.91	0.99			
<b>Average</b>	771.1	108.3	29.7	40.9	28.7	0.75	0.72			
<b>Std. Dev</b>	534.7	38.3	10	14.9	10.3	0.08	0.14			
<b>Relative Error (Current study vs. AD 2 data)</b>										
<b>Min.</b>	20.56%	12.10%	10.68%	13.94%	46.24%	10.10%	14.57%			
<b>Max.</b>	21.07%	4.80%	11.16%	16.37%	46.04%	2.65%	16.38%			
<b>Average</b>	31.78%	18.68%	19.91%	23.49%	35.04%	1.60%	15.80%			

### 5.3.2.2 B-Scans

The ice wedge polygons site is of special interest as all the GPR units performed measurements on the same location. In Figure 5.15.a two profile lines are perpendicular to each other with the aim of studying the GPR response with varying relative position respect to the polygon troughs. *Line 1* crosses perpendicularly two pronounced troughs while *Line 2* remains semiparallel to the through. These profile lines have been recorded by WISDOM*prototype* and pulseEKKO. Figure 5.15.b the four parallel tracks of WISDOM*fs2* are presented. Tracks 1-3 have been recorded in single polarisation while Track 4 in full polarisation to evaluate the difference between the visualisation of features depending on the antenna configuration.

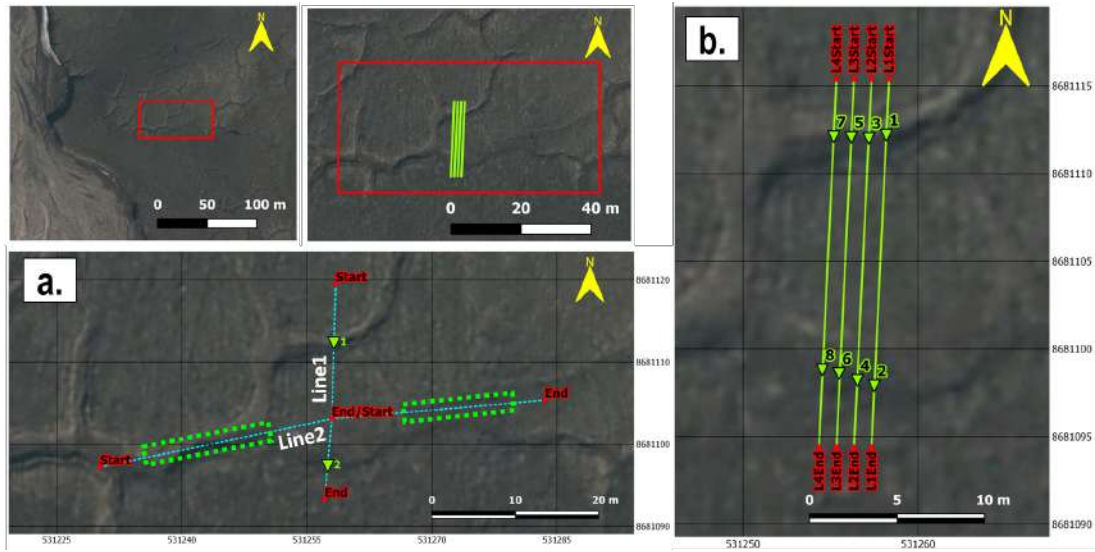


Figure 5.15: Profile lines at ice wedge polygons site. On (a) *Line 1* (from North to South) and *Line 2* (from West to East), both lines recorded by WISDOM*prototype* and pulseEKKO. On (b), four tracks by WISDOM*fs2* from North to South.

Figure 5.16 shows both lines recorded by pulseEKKO perpendicular and parallel to the polygon troughs. The first thing that can be observed is the better performance of the radar when crossing perpendicularly the troughs. The hyperbolas in Figure 5.16.a are clear and neat and have served as benchmark to calculate the propagation velocity (via hyperbola fitting) and migrating the data (Figure 5.16.b). The obtained velocity matches with previous investigations performed at the Old Aurora Station (see Section A.1.1) making results reliable. For all these reasons, the propagation velocity obtained at *Line 1* has been assumed to be the same for the rest of the profiles taken at the ice wedge polygons, even in the case of disagreement with the hyperbola fitting results on a specific profile. A detailed description of this choice is given below, in Section 5.3.2.3.

Figure 5.16.c shows the reflections when the GPR moves mostly parallel to the troughs. These reflections are characterised by being more chaotic (the hyperbolas are superimposed, thus making it challenging to distinguish unequivocally one) and spread over a longer region. Note that without ground-truth information it is not possible to distinguish the reflections at the polygon centre caused by stones, changes in soil grain size, etc. from those when the GPR is parallel to the through. In fact, the response is only clear at the transition from trough to polygon centre.

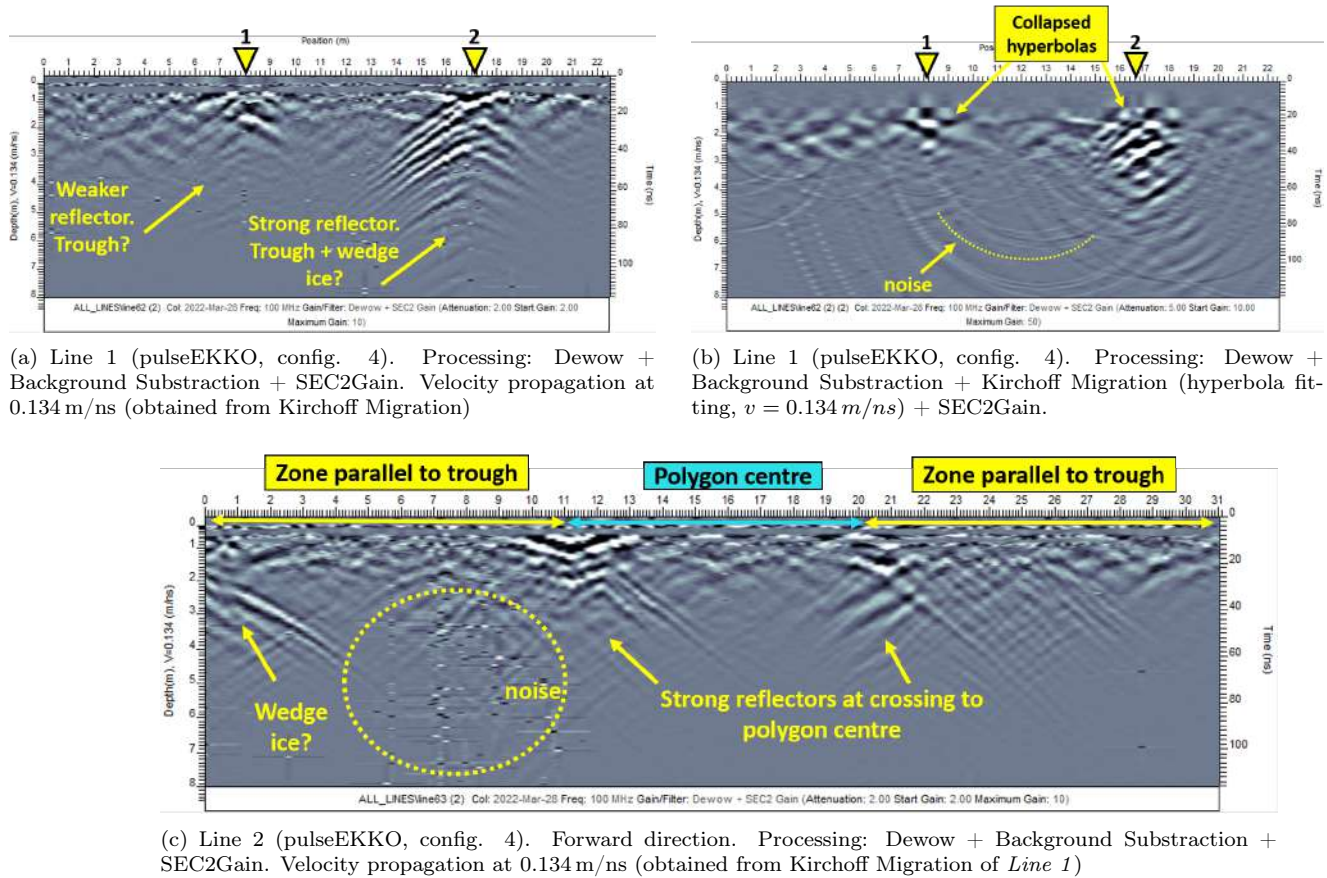
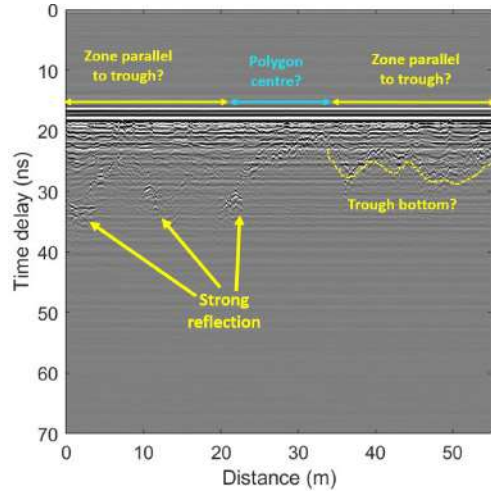


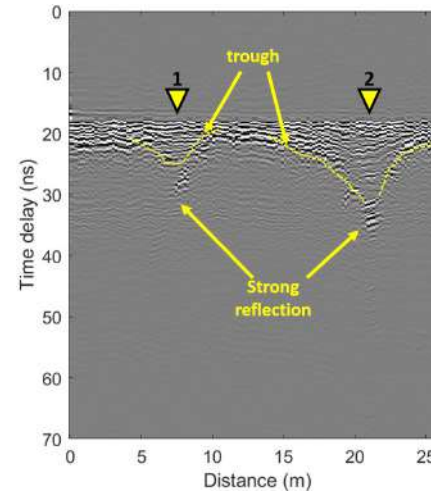
Figure 5.16: Perpendicular lines over ice wedge polygons. (a) and (c) show the unmigrated profiles. (b) shows *Line 1* after Kirchoff Migration. Note the appearance of semicircular geometries on the lower half of the radargram. This is induced noise as result of the migration.

WISDOM radargrams display very similar features to those recorded by pulseEkko. Figure 5.17.c and Figure 5.17.d present *Track 2* and *Track 4* at single and full polarisation, respectively. At full polarisation both deep reflectors at the bottom of the trough are weaker but for the second trough, the surface slope rising to the polygon centre is more visible. In the WISDOM *prototype* profile the troughs are clearly visible (see Figure 5.17.b) as well as the bottom reflection. The second one, just as for the pulseEKKO, is stronger and comes from deeper.

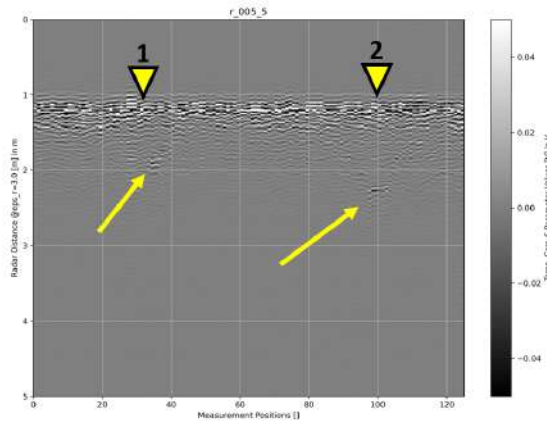
WISDOM *prototype Line 2* shows the reflection when parallel to the troughs. As previously, reflections are more scattered and is required to use the aerial imagery to establish which signals originate from the trough and which from the polygon centre. Comparing Figure 5.17.a to pulseEKKO's *Line 2* some reflectors seem to match while others do not. Figure 5.16.c first reflector starting from the left seems to correspond to also the first reflector in Figure 5.17.a, and possibly indicates wedge ice. The third one in Figure 5.17.a (from left to right) is followed by a gentle slope (note the axis are deformed and despite seeing a steep angle it corresponds to a rather flat one) which highly likely is equivalent to the strong reflector when crossing the trough to the polygon centre in Figure 5.16.c, thus, caused by the geometry of the terrain. On the other hand, the second reflector in WISDOM's *Line 2* does not have any equivalent on pulseEKKO's and is also weaker than the neighbours, indicating might be a stone. Figure 5.17.a second parallel zone to trough (right hand side of image) seems more consistent with initial expectations, continuous reflections from the bottom of the trough once the GPR has crossed the polygon centre.



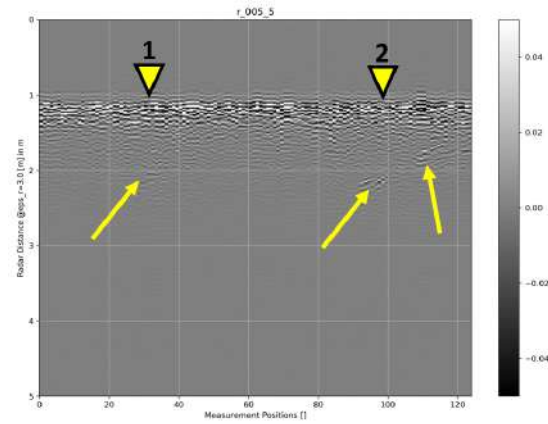
(a) Line 2 (WISDOMprototype, full polarisation). Spacing of 20 cm. Processing: FreeSpace removal



(b) Line 1 (WISDOMprototype, full polarisation). Spacing of 20 cm. Processing: FreeSpace removal + background subtraction



(c) Track 2 (WISDOMfs2, single polarisation 0/0). X-axis in measurement positions of 20 cm spacing. Y-axis indicated in meters assuming  $\epsilon_r = 3$ , ( $v = 0.173 \text{ m/ns}$ ).



(d) Track 4 (WISDOMfs2, full polarisation). X-axis in measurement positions of 20 cm spacing. Y-axis indicated in meters assuming  $\epsilon_r = 3$ , ( $v = 0.173 \text{ m/ns}$ ).

Figure 5.17: Profile lines by WISDOM units

### 5.3.2.3 Grid and 3D-radargrams

Two grids of different sizes were done by driving a snowmobile in a zig-zag fashion, towing the GPR sledge. The small grid consists of 11 lines in North-South direction of 30 m length and 7 lines in the East-West direction of 50 m length. The large grid is defined by 17 lines of 70 m length in the North-South direction and 8 lines of 70 m in the East-West direction. The grids were firstly elaborated in *QGIS*, then the tracking lines were transferred to a GPS unit and they were followed by snowmobile. As it is shown in Figure 5.18, some lines deviate from being parallel, altering the spacing of the grid. Aside from human error, the main cause was terrain unevenness needing to avoid some areas due to exposed soil and stones.

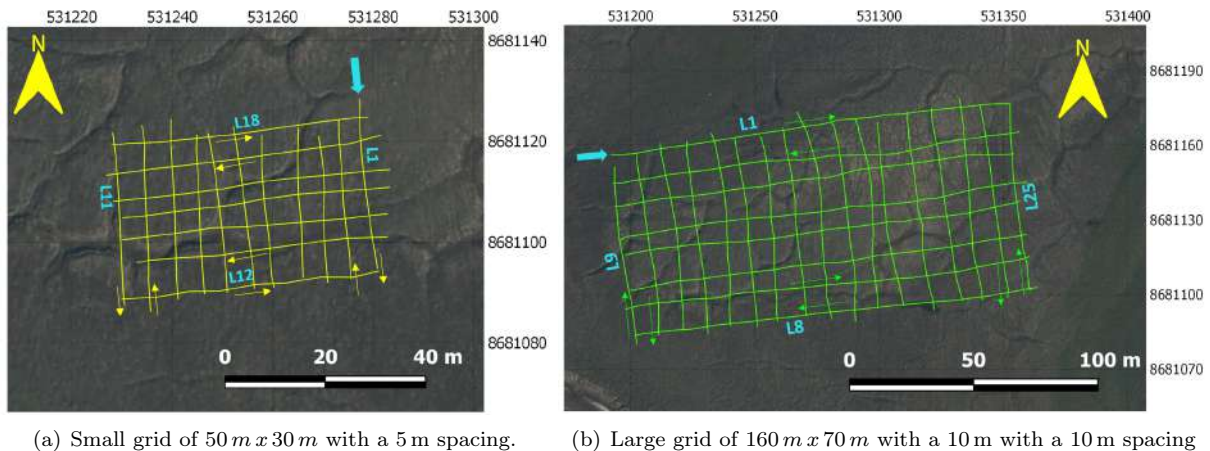


Figure 5.18: GPR grids. The blue arrow indicates the starting point of each grid. From there each line has been done in zig-zag, meaning that consecutive lines have been retrieved at opposite directions. Background map: © Norwegian Polar Institute/CC BY 4.0

#### *Data processing*

On Section 5.3.2.2 single GPR lines show the system response to targeted troughs. The goal was understanding the difference in GPR response depending on the direction of crossing the trough. On this one, the lines constituting the GPR grid are joined with the aim of elaborating map of the wedge ice buried under the polygon troughs. The main goal is to actually see the GPR response superposed on the aerial images where the polygon features are visible for different depths (depth slices).

For doing so, it has been necessary to combine different software in order to maximise the flexibility of analysis and control over the data. As shown in Figure 5.19, first the data has been processed by the *Sensors&Software* software, *Ekko Project V6*. All lines belonging to the same grid have the same processing steps with same values, except for the Kirchoff Migration. The Kirchoff migration requires from a velocity of propagation in order to collapse hyperbolas to single points (which for this project the migration velocity has been obtained by hyperbola fitting). A problem encountered has been that the migration velocity varies from line to line, when in principle the media is sufficiently similar to remain the same. This variation has been attributed to the fact that the snowmobile velocity (despite efforts) has not been constant throughout the recording. The consequences of this velocity variations during GPR retrieval cause differences in migration velocity among lines but also *deformations* of the hyperbolas. If the retrieval velocity presents variations within the same GPR line hyperbolas will result asymmetric, for instance, the branch of the hyperbola going at lower speed will be more open than the other. The latter is even more challenging as no Kirchoff migration will fully collapse the hyperbolas unless each trace is repositioned with the corresponding velocity at each of the traces. This would require the triggering of the GPS synchronised with the GPR which was not possible for this pulseEkko unit<sup>8</sup> All in all, the

<sup>8</sup>The pulseEkko unit has an internal GPS but cannot be used on free-run mode. An external GPS was only available at



best solution found was to migrate each line individually by using the velocity obtained from manual hyperbola fitting regardless of the value obtained<sup>9</sup>. Hence, the purpose of migrating has been exclusively to best collapse to points the hyperbolas, without binding the migration velocity to the actual medium's propagation velocity. On the other hand, a medium velocity has been calculated via hyperbola fitting from *Line 1* (see Figure 5.16) and has been assumed to be the media velocity for all the grid profiles, being  $0.134\text{ m/ns}$ . This velocity is the one that has determined the depth at which features are detected.

The processed lines are read with open-source GPR software *GPRPy* (Plattner, 2021) to access the data in the *DT1*<sup>10</sup> files. For each grid, data is normalised with the maximum absolute value of the grid lineset and data is divided into two different categories. A normalised raw data set were values are comprised between -1 and 1 and an *enveloped* dataset were values are the absolute of the normalised raw data set, varying between 0 and 1. The choice of transforming the normalised raw data to normalised *enveloped* data is a better interpretation of the depth slices. Normalised raw data is visualised in 3D with the *PyVista* (Sullivan and Kaszynski, 2019) package, a VTK visualisation toolkit. As the grid density is rather low, it has been decided to avoid a 3D interpolation and simply show the B-scans spatially instead of creating a volume. On the other hand, normalised *enveloped* data is further processed in *QGIS*. A IDW (Inverse Distance Weight) interpolation is applied, which applies a weighting coefficient that drops off as the distance from the reference point increases. As data is not evenly distributed it is prone to create a *bull's-eye effect* on the interpolation which is smoothed out by a Gaussian-filter. The last step is clipping the data, only displaying it within the region of influence of the grid (4m width for the small grid and 6m width for the large grid).

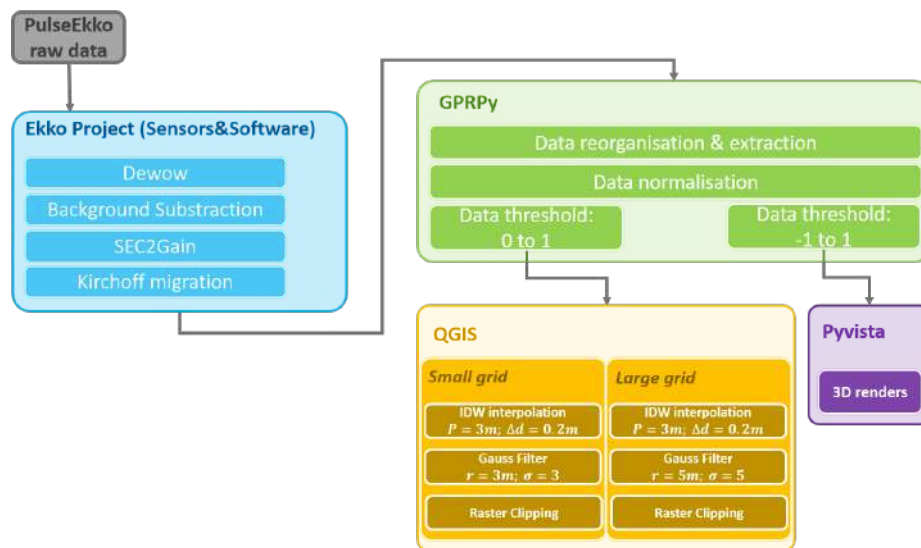


Figure 5.19: Data processing diagram

### *GPR mapping and 3D images*

Figure 5.23 and Figure 5.22 show different depth slices of the small and large grid, respectively. The depth slices have been projected on top of the aerial images of the polygons as well as with background grid lines and trough contour lines of 3 m width. The latter is shown to facilitate the visualisation of GPR response on the different polygon regions. The slices presented start at 0.5 m depth and reach 8.5 m depth by 1 m intervals. First of all, it must be noted that the relevant GPR response starts at 1.5 m deep and the last survey on 11-05-2022.

<sup>9</sup>This statement is partially true. While the numerical value has not been taken as the media's velocity, its value still has been evaluated to ensure hyperbolas were not caused by other interferences. In other words, to ensure the hyperbola fitting resulted in a propagation velocity below  $0.3\text{ m/ns}$ . Results from manual hyperbola fitting range from  $0.18\text{ m/ns}$  to  $0.13\text{ m/ns}$

<sup>10</sup>*Sensors&Software* GPR files format.

fades away at 6.5 m depth. In the case of the small grid, there is still visible signal on the trough area up to 7.5 m depth.

At 1.5 m most of the GPR signals are still faint and scattered and there is no distinction in their intensity between those on a trough from those on the polygon centre. On the large grid (Figure 5.22.b) several moderate intensity spots appear in and out the polygon buffer-boundaries alike. However, two high intensity spots are displayed on the southern corners of polygon num.11<sup>11</sup>. The one on the left is consistent with a response created by potential wedge ice as the signal is present in further depth slices, whereas the one on the right is unclear if might be caused by a stone as it fades for all depth slices except for reappearing at depth 3.5 m. The small grid (Figure 5.23.b) shows a very similar pattern in which moderate intensity GPR responses are scattered across the grid independently of polygon features at depth 1.5 m. At this depth, two intense responses that eventually blur out at a depth of 3.5 m are found on the south-western corner of polygon 6 seemingly related to the signal reflection when crossing the trough.

Depth slice at 2.5 m is the one displaying generalised GPR reflections all over the grid. At this specific depth slice, multiple reflections triggered by the polygon patterned ground and by other terrain features such as a deeper layer of snow, surface ice, vegetation, stones are both of a similar intensity. In fact, both Figure 5.22.c and Figure 5.23.c show slightly more intense reflections when lines cross perpendicularly the polygon's troughs than when passing over the polygon's center. However, it is not possible to distinguish by the intensity the cause of the GPR reflection without relying on the aerial imagery.

In depth slices from 3.5 m to 5.5 m one can see the contrast between the strong reflectors almost exclusively at the troughs and the rest of the grid. Focusing on the large grid, there is one characteristic that stands out: the central and North-Eastern polygons produce barely no response when the GPR records over the troughs. Observing Figure 5.12.a it can be seen that the troughs of this area seem less prominent than their southern counterparts. For example, the boundaries between polygon pairs 16-17, 9-17, 13-17 are hardly visible on the map. Indeed, if polygon troughs are narrow and to a similar elevation than the polygon centre the GPR reflections will be weak or non-existent. In contrast, polygon 3's top and right troughs can barely be seen on the aerial image and nonetheless, the GPR reflections are strong. While lighting may affect the perception of how deep the trough is, repeated GPR reflections seem to point to the presence of wedge ice. The lack of intense reflections even at 2.5 m depth at the central and North-Eastern polygon boundaries seem to support not only small shallow troughs but a lack of wedge ice beneath. As depth increases only stronger reflections remain and they tend to concentrate only at the troughs crossings.

Turning to the small grid, from a depth slice of 3.5 m to 6.5 m reflectors concentrate at the trough crossings, particularly, around polygon 8 boundary. The results obtained are not as expected. It can be noted that the top and bottom troughs of polygon 8 accumulate most GPR reflections while the Eastern and Western troughs are passed undetected. First, this behaviour is not explained by the relative positioning of the line and the trough (parallel vs. perpendicular) as the grid spacing is small enough to slice polygon's 8 boundaries at at least three different points. Second, the strong reflectors do not correlate with the most visible troughs on the aerial image (being the left and top one as shown by Figure 5.12). In fact, the GPR response is stronger at the top and bottom ones. The most plausible explanation is that the top and bottom troughs present wedge ice beneath them which causes strong GPR reflections, while lateral ones do not host any ice or very little. After normalising the data, the more superficial and weaker GPR responses are only visible at shallow depths (up to 2.5 m) and they fade out as slices go deeper where only multiple reflections caused by wedge ice are visible.

The final depth slices (from 7.5 m to 8.5 m) show, for both grids, that most of the signal has attenuated and it is not possible to distinguish any more features. The higher intensity regions correspond to the vanishing multiple reflectors caused by the wedge ice.

Figure 5.20 shows two depth slices, one for each grid, at which GPR response is mostly free of anomalous reflectors and has a higher response on the troughs. The small grid is characterised by a broader area of high intensity over the southern trough that goes well beyond the edges of the polygon perimeter

<sup>11</sup>The reader is referred to Figure 5.12 when polygon numbers are quoted.

buffer (see arrow on [Figure 5.20.a](#)). This is associated with an unfitting Kirchoff Migration that could not manage to collapse hyperbolas, thus, the resulting GPR response expands over the surroundings of the target (trough) rather than a continuation of the ice wedge. For a better illustration of this scattering effect, [Figure 5.21](#) depicts a 3D image of two single lines belonging to the small grid. A total of three reflectors are marked with an inverted yellow triangle number from 1 to 3. Reflector 1 is recorded in both lines, hence, when the interpolation is made the reflector will be displayed as strong and concentrated in the same region. Reflector 2 is an example of a far from ideal Kirchoff Migration. It can be observed that despite the line is migrated the reflector partially displays a hyperbolic shape which will translate in a extended highlighted area instead of small region reflector. Reflector 3 is noticeably weaker than its counterparts and will yield a mild intensity response on the depth slicing.

Another feature draws the attention, this time on the large grid. [Figure 5.20.b](#) illustrates how polygon 12 is splitted in half by a line of strong reflectors (marked with an arrow). If one takes a look to other depth slices ([Figure 5.22](#)) this reflector line is found very mild at 2.5 m, holds at 3.5 m and 4.5 m and is completely vanished at 5.5 m. These GPR responses could be caused by the shortcomings of the Kirchoff migration but it seems consistent actual wedge ice reflectors. By observing attentively [Figure 5.12](#), a trough is hinted exactly at the location where the strong GPR responses are found, dividing polygon 12 virtually by half. It is not possible without ground truth information to distinguish between the multiple reflection signals caused by the wedge ice beneath the soil.

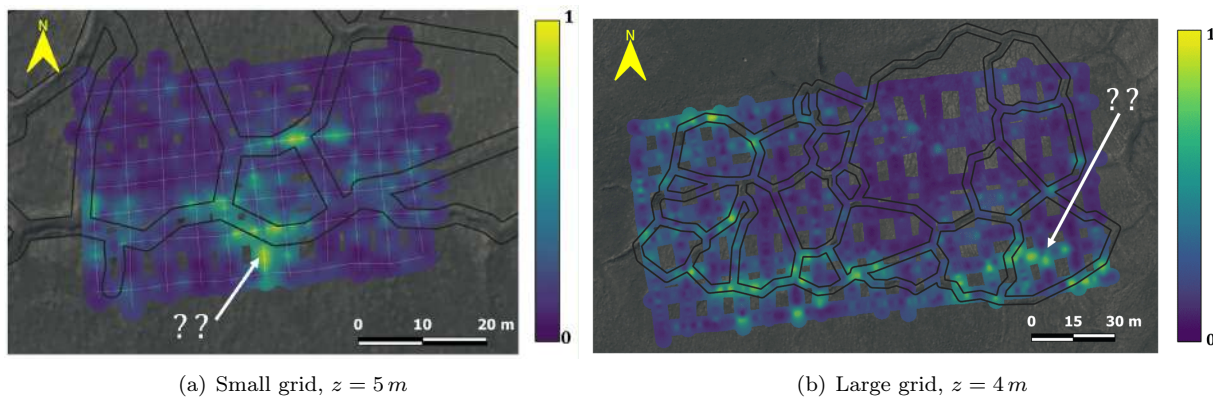


Figure 5.20: GPR depth slices. Both slices have been chosen when the trough response is maximum. Background map: © Norwegian Polar Institute/CC BY 4.0

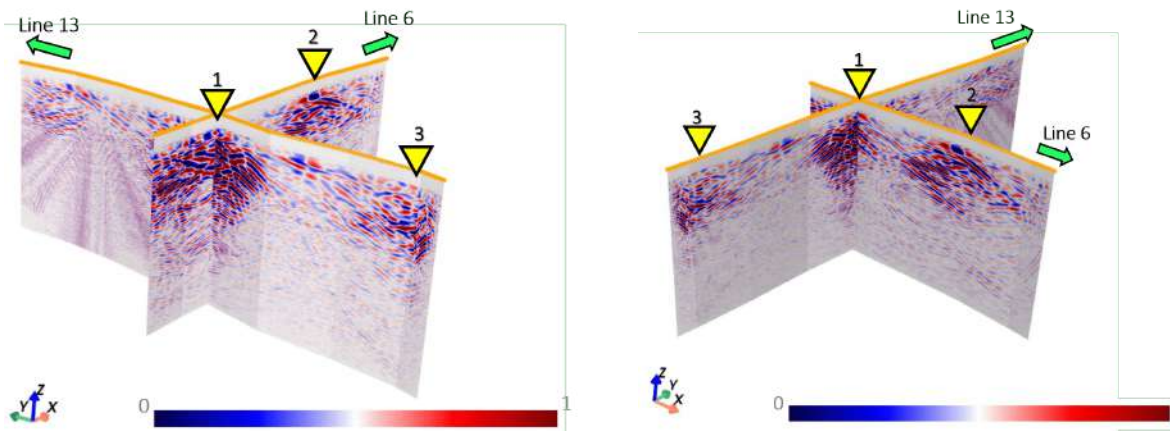


Figure 5.21: 3D rendered images

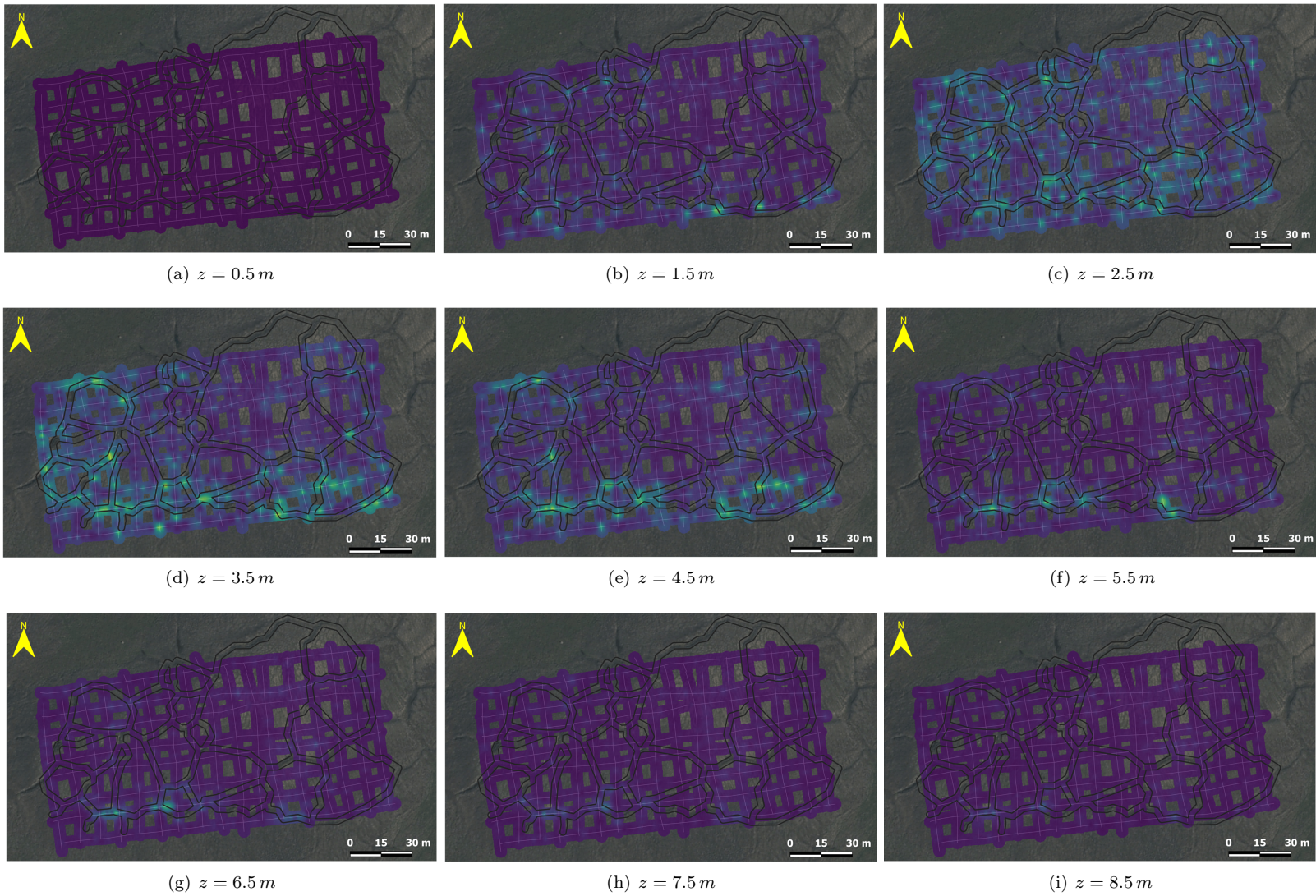


Figure 5.22: Large grid depth slices. Background map: © Norwegian Polar Institute/CC BY 4.0

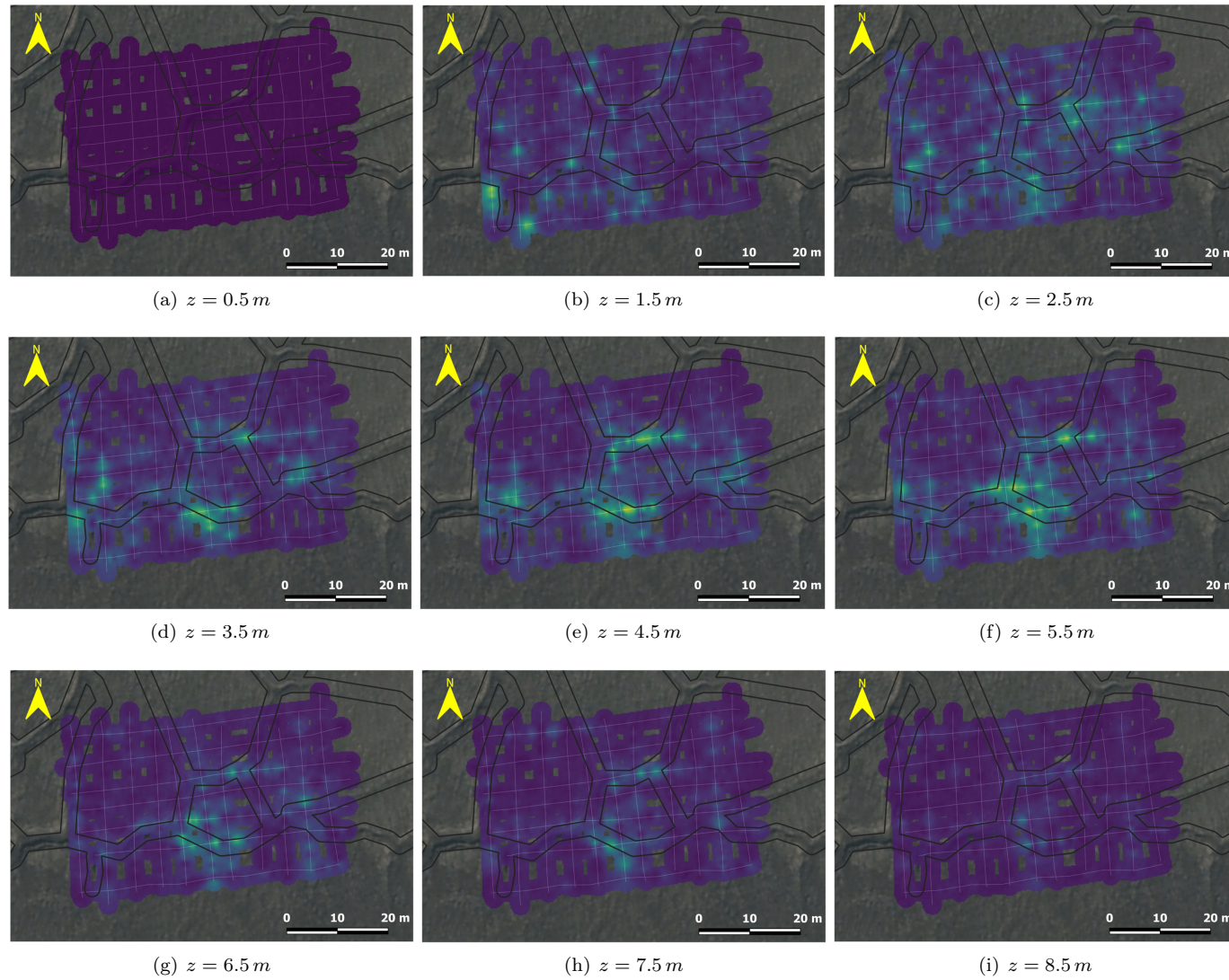


Figure 5.23: Small grid depth slices. Background map: © Norwegian Polar Institute/CC BY 4.0

## 5.3.2.4 Ice Wedge Volume estimation

Table 5.4: Polygon network parameters

Parameters	
Trough width [m]	3
Ice Wedge depth [m]	6
Ice Wedge shape	Inverted isosceles triangle

The GPR mapping results of the large grid have been used to estimate the wedge ice volume (WIV) beneath the polygon troughs. These results are combined with characteristic parameters of the polygon network that are summarised in Table 5.4 and which are modelled as constant for the wedge ice volume calculation. The choice of these values is a combination between literature values and direct observation from aerial imagery. Trough width was possible to determine directly from the *QGIS* polygon delineations, finding a 3 m buffer as a good fit. This parameter alongside ice wedge depth and shape are in agreement with previous research. The reader is referred to Section 3.2.1.1 and Section 6.3.3 where the implications of considering a different shapes and depths are discussed. Figure 5.24.a shows the buffer area that covers the polygon troughs and that is referred as  $V_{ice}$  on Table 5.5. It is important to note that both methods, despite the second one having several more steps, result in very similar values that just differ by approximately  $225 m^3$ . This value is corrected to adjust the actual boundaries of the GPR grid. Figure 5.24.b shows three buffered lines in yellow and a green buffered line with a bifurcation that represent missing and extra trough areas, respectively. In other words, the large grid includes three troughs that are not linked to any polygon (shown in yellow) whereas the grid does not cover the northernmost part of the polygon network (shown in green). So, the troughs marked in yellow are added and those marked in green are removed to the initial WIV ( $V_{ice}$ ), resulting in the corrected WIV ( $V'_{ice}$ ). The same reasoning is applied for obtaining the corrected volume of sediments ( $V'_{total sed.}$ ). Then, the corrected WIV is divided by the total volume (corrected sediments+ice) in the polygon network obtaining the WIV in volumetric percentage: 14.84% (Method 1) and 15.14% (Method 2).

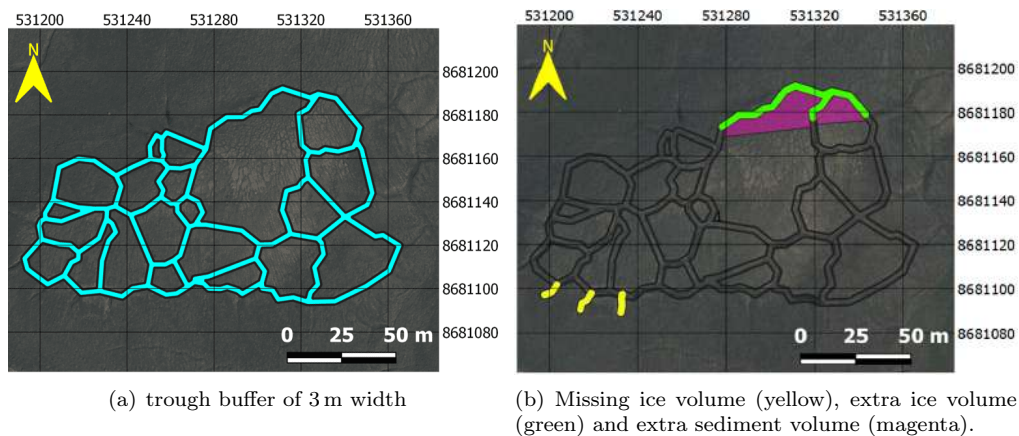


Figure 5.24: Trough buffer for the estimation of wedge ice volume. Background map: © Norwegian Polar Institute/CC BY 4.0

The same estimation is made taking into account the GPR readings of the depth slice at  $z = 4 m$ , shown in Figure 5.20.b. As discussed in the previous section, it is not clear what might constitute an ice wedge reflection or a trough reflection, as well as reflections caused by other objects such point structures (stone), change in soil composition, etc. Depth slice at  $z = 4 m$  is chosen as it offers a maximum contrast of signal between trough and polygon center's region. The next step is deciding which part of the signal corresponds to wedge ice and which does not. This choice is arbitrary, resulting from trial and error of which areas end up selected when given a certain threshold. Due to the uncertainty introduced by choosing the threshold, three different values are analysed to see how they affect results (see on Table 5.6 *Normalised GPR response threshold* of values 0.3, 0.4 and 0.5). Note that the total volume used in the

calculations is that obtained with Method 1.

Table 5.5: WIV estimation on GIS

	Method 1	Method 2
<b>WIV</b> ( $V_{ice}$ ) [ $m^3$ ]	10059.39	10283.89
<b>Corrected WIV</b> ( $V'_{ice}$ ) [ $m^3$ ]	9514.34	9738.83
<b>Total volume sediments</b> ( $V_{total\ sed.}$ ) [ $m^3$ ]	58362.54	
<b>Corrected total volume sediments</b> ( $V'_{total\ sed.}$ ) [ $m^3$ ]	54596.42	
<b>Total volume</b> ( $V_{total}$ ) [ $m^3$ ]	64110.75	64335.25
<b>WIV vol. %</b>	14.84%	15.14%

Table 5.6: WIV estimation according to GPR data, depth slice  $z = 4\ m$

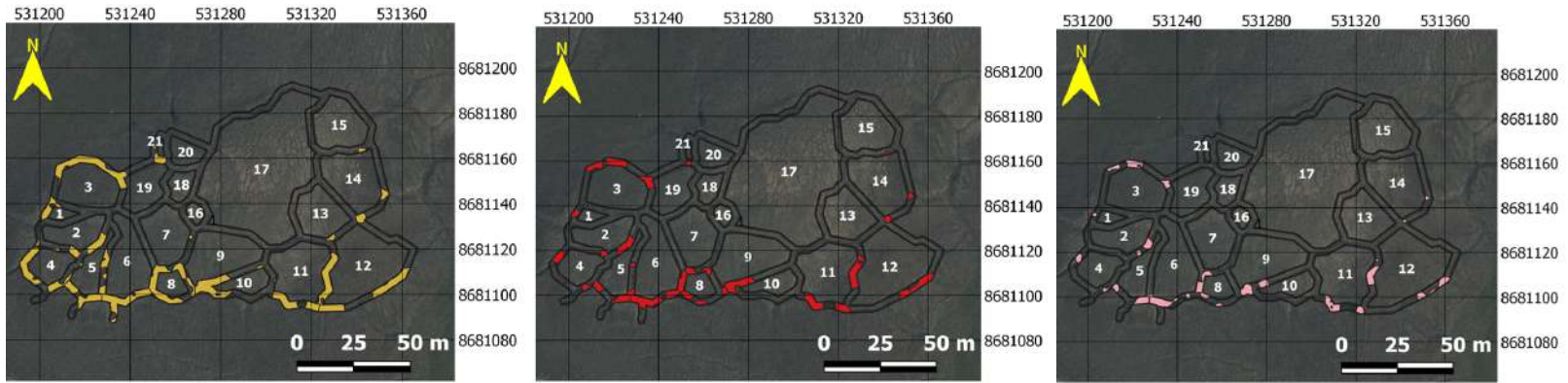
	Normalised GPR response threshold		
	> 0.3	> 0.4	> 0.5
<b>WIV</b> ( $V_{ice}$ ) [ $m^3$ ]	2877.85	1624.52	954.08
<b>Total volume</b> ( $V_{total}$ ) [ $m^3$ ]	64110.75		
<b>WIV vol. %</b>	4.49%	2.53%	1.49%

Figure 5.25 from (a) to (c) show the areas corresponding to wedge ice presence for the different given thresholds. It can be observed that GPR-derived WIV is considerably lower than GIS-derived WIV. For a threshold value of 0.3 the estimated amount of ice is about 3.5 times less than that predicted by GIS<sup>12</sup>, while for a threshold value of 0.5 is approximately 11 times less. It must be noted that the GPR-derived WIV does not include the WIV detected outside the trough buffer boundaries. Figure 5.20.b shows a clear strong reflector crossing polygon 12's centre and this might as well be included for the estimation of wedge ice. As it is only a preliminary estimation of the GPR-derived WIV and there is only a unique case in which the GPR response suggests wedge ice outside the trough region, only the signals within the trough's buffer have been considered.

In addition, a correlation between the ice wedge area (IWA) and the corresponding elevation is presented in Figure 5.25 from (d) to (f). The plots x-axis shows the ratio (in percentage) between buffer area covered by wedge ice and the polygon area calculated for each polygon. For example, polygon 8 has an area of  $A_{pol.8}$  and its buffer zone has a total ice wedge coverage area of  $A_{IW}$ , then the ratio will be expressed as  $A_{IW}/A_{pol.8}$  %<sup>13</sup>. For IWAs shared by  $N$  polygons, then the value is divided by  $N$  and assigned to both polygons (in most cases being  $N = 2$ ). The plots obtained show a trend in which the presence of wedge ice increases down-slope.

<sup>12</sup>The statement is valid for both Method 1 and Method 2

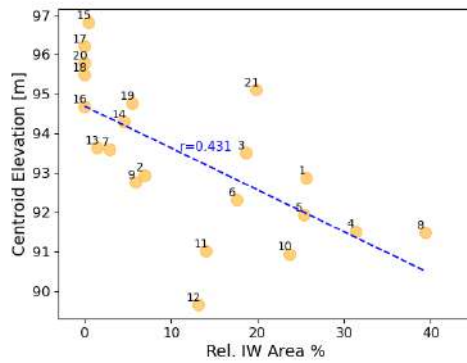
<sup>13</sup>Using area or volume (calculated by Method 1) is equivalent as they relate to one another by a factor of  $d/2$ , where  $d$  is the depth of the inverted isosceles triangle:  $A * d/2 = V$



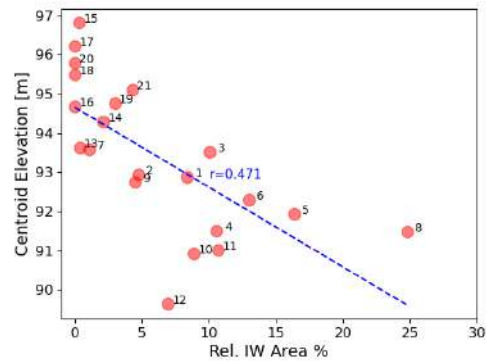
(a) Regions with GPR values above 0.3

(b) Regions with GPR values above 0.4

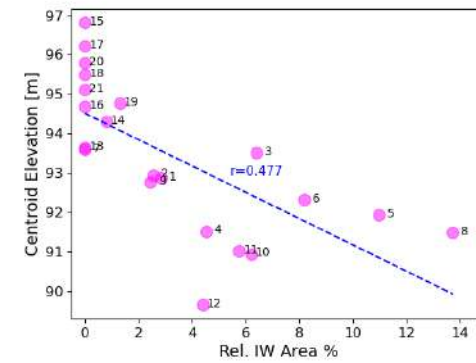
(c) Regions with GPR values above 0.5



(d) Elevation vs. WIA for &gt; 0.3



(e) Elevation vs. WIA for &gt; 0.4



(f) Elevation vs. WIA for &gt; 0.5

Figure 5.25: Ice Wedge coverage area for different thresholds. Images a) to c) show the GPR ice wedge coverage on the map. Images d) to f) show correlation between ice wedge areas and elevation of the polygon centroid. The label on the points corresponds to the polygon's number. Note that the limits of the x-axis vary for each plot to make data readable. Background map: © Norwegian Polar Institute/CC BY 4.0



## 5.4 Site 4: River Bed Pingo

A total of four different lines have been investigated at River Bed Pingo. *Line 1* and *Line 2* have been both profiled by WISDOM<sub>prototype</sub> and pulseEKKO units. *Line 1* is characterised by being short (12 m) and targeting the southern crest of the pingo. *Line 2* profiles the southern slope of River Bed Pingo, a very steep slope that has not been previously investigated with GPR due to its challenging terrain. On the other hand, *Line 3* has only been profiled by WISDOM<sub>prototype</sub> and it is of special interest as a total of 4 equally spaced ice cores were drilled with the aim of better understanding the radargrams. *Line 4* became an alternative path to *Line 3* caused by changing environmental conditions that made the original line impassable. This line was recorded by pulseEKKO unit. Figure 5.26 gives a geographical context of the profile lines.

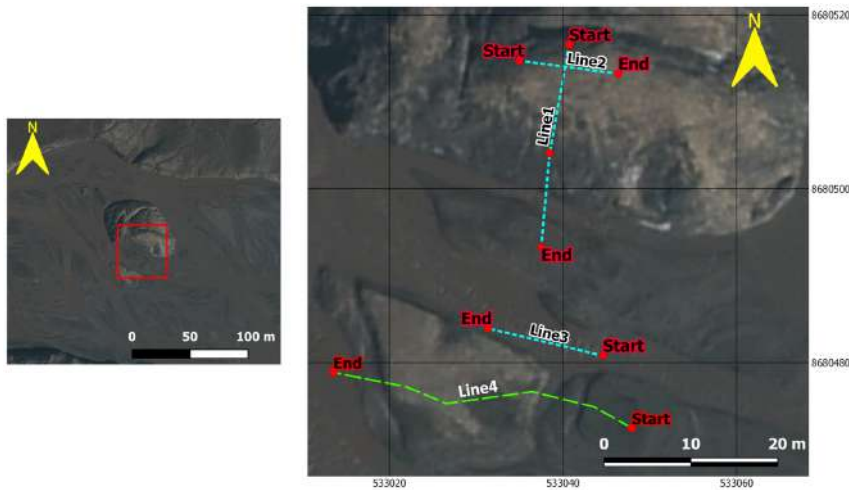
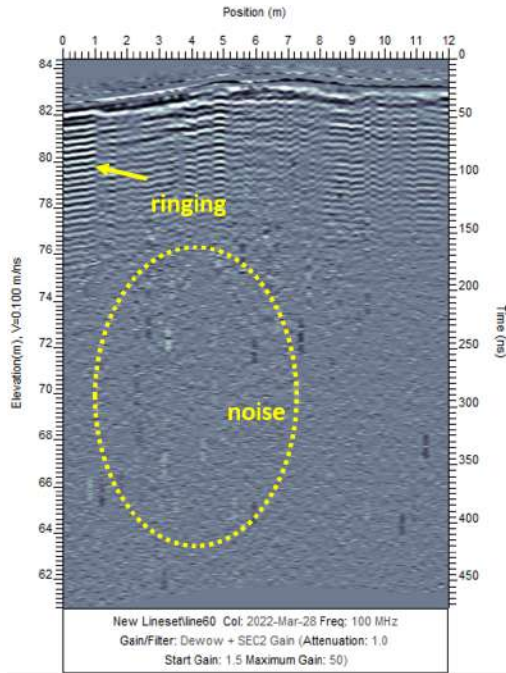


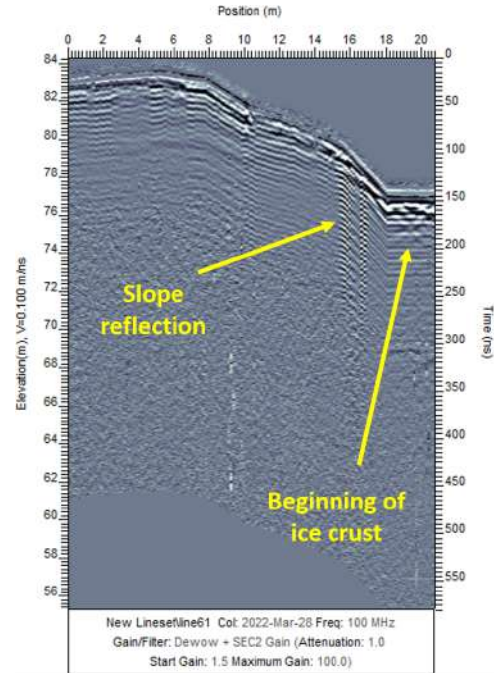
Figure 5.26: Profile lines at River Bed Pingo. Background map: © Norwegian Polar Institute/CC BY 4.0

### 5.4.1 Pingo crest and slope

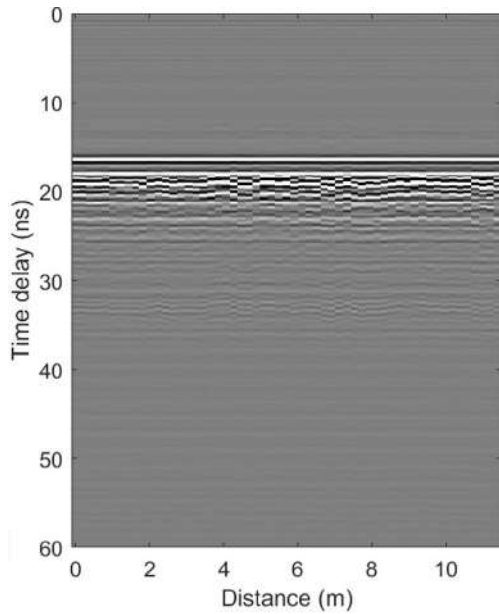
Figure 5.27 shows the different profile lines recorded by pulseEKKO and WISDOM<sub>prototype</sub> on the crest and southern slope of the pingo. Overall both GPRs -despite their frequency difference- experience the same clutter on the surface with no sign of an ice lens buried beneath the surface. This signal attenuation is attributed to the shales present on the pingo's surface, but the generalised ringing effects came as a surprise. In our survey, the only reflections registered are those corresponding to the reflection of the steep slope itself and some ice layering once the GPR has completely descended the slope entering in the ice crust region. *Line 1* was expected to produce the best results and even potentially map the ice lens of the pingo. In fact, it was chosen thinking that its pronounced steepness might translate to a thinner layer of sediments over the pingo's core and hence a better performance of all GPR units. A trade off between deeper penetration on the terrain for a more challenging terrain. Nevertheless, not even pulseEKKO's 100 MHz antennas could distinguish any feature at all.



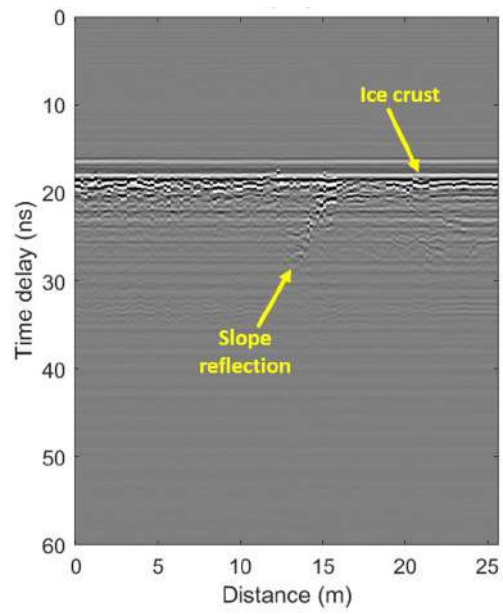
(a) Line 2 (pulseEKKO, config. 4). Processing: Dewow + Background Substraction + SEC2Gain + Topography Correction



(b) Line 1 (pulseEKKO, config. 4). Processing: Dewow + Background Substraction + SEC2Gain + Topography Correction



(c) Line 2 (WISDOMprototype, full polarisation). Spacing: 20 cm. Processing: FreeSpace removal



(d) Line 1 (WISDOMprototype, full polarisation). Spacing: 20 cm. Processing: FreeSpace removal

Figure 5.27: Pingo crest and slope radargrams

### 5.4.2 Ice crust region

The conditions during our survey were evident that underground water was flowing out to the surface on all the southern and south-western area of the River Bed Pingo. Owing to the cold conditions, the groundwater on the surface had frozen and had formed a layer of ice. In some regions several centimeters thick and others not thick enough to sustain a person walking (less than 5 cm thickness). This icy formation draws particular attention because of its orange-brownish colour and iron-like smell. The aforementioned properties point to a high concentration of iron oxides minerals, but samples need a chemical analysis before drawing any conclusions.

Despite not being the same profile line, both pulseEKKO and WISDOM<sub>prototype</sub> detect the ice crust layering as well as the water-ice interface in their radargrams. For PulseEKKO's *Line 4*, a velocity of 0.16 m/ns was deduced from hyperbola fitting, resulting in an ice crust thickness of 4 m. *Line 3* from WISDOM<sub>prototype</sub> has been compared to ground truth data in order to estimate the propagation velocity as well as cross-checking the ice thickness obtained from the GPR measurements. A total of four ice cores (*A*, *B*, *C* and *D*) were drilled at each of the sides of an ice crack found at 7 m, with a spacing of 50 cm between each other. The ice core depths vary between approximately 55 cm and 80 cm depth and present layers alternating different shades of orange with pure ice with a thickness that oscillates between between 10 cm to 20 cm at most (see [Figure 5.29](#)). Ice cores *C* and *D* have a dark layer at 55 cm depth which could correspond to a high concentration of shale sediments.

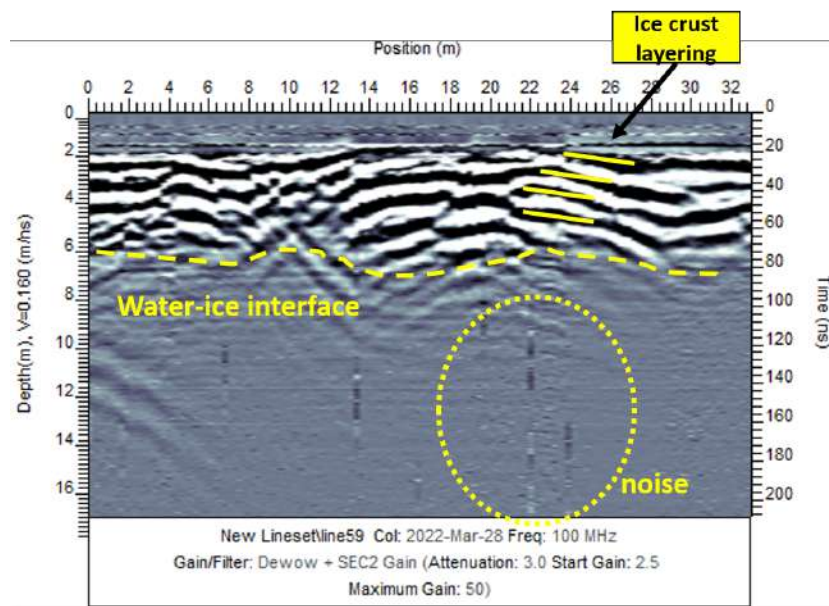
According to the salinity analysis (see [Section 5.4.2.1](#) below) the velocity of propagation on the ice crust is of 0.169 m/ns. This ground-truth-derived velocity has been used on the WISDOM<sub>prototype</sub> radargram to determine the thickness between ice layers and the ice crust. The chosen points are those corresponding to the actual ice cores drilled in order to have a direct comparison between measured in-situ depth and GPR-derived depth. Results are summarised on [Table 5.7](#).

Table 5.7: In-situ measurements vs. GPR estimated values

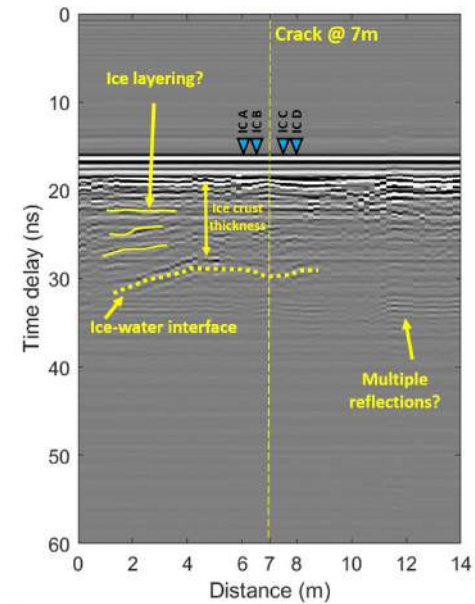
Pos. [m]	Feature	Initial Time [ns]	Final Time [ns]	Thickness [m] @ $v = 0.169 \text{ m/ns}$	Ice core depth [m]
2.4	Ice Layering	24.266	26.133	16	
6	IC A	18.866	28.766	84	62
6.5	IC B	18.466	29.166	90	54
7	(crack)				
7.5	IC C	18.866	29.766	92	56
8	IC D	18.966	29.466	89	81

One can see that GPR calculated thickness and the actual ice core depth vary considerably, being only the ice core *D* the one matching with ground-truth data. It must be noted that when the drilled reached the bottom of the ice cores it encountered water. It is possible that the splashing could have washed out the last 5 cm to 10 cm of ice, but this explanation does not seem to hold for variations greater than these values. Also, the points to calculate the thickness on the radargram have been chosen manually, which entails errors. The ice cores also support the region marked on [Figure 5.28.b](#) as ice layering, as the calculated thickness ([Table 5.7](#)) matches with the distance between different ice layers. Overall, GPR-estimated thickness and in-situ measurements have the same order of magnitude and confirm the interpretations made on the radargram.

After the ice crust dept study on *Line 3* the radargram results on *Line 4* seem higher than one would expect. While the profile line is not the same and environment conditions were much colder (during pulseEKKO campaign the temperature was  $-20^{\circ}\text{C}$ ) the ice crust of *Line 4* is 3 m thicker than *Line 3*. So far, these results are taken as valid and associated to a dipping of the ice crust, as the propagation velocity estimated at *Line 4* via hyperbola fitting is close to that of *Line 3*.

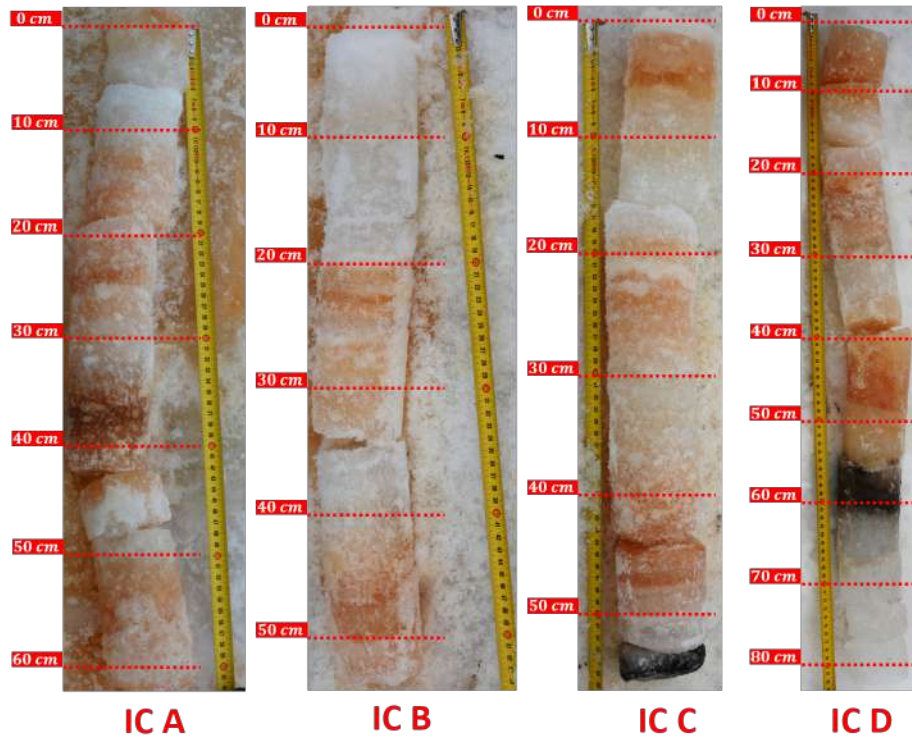


(a) Line 4 (pulseEKKO, config. 4). Processing: Dewow + Background Substraction + SEC2Gain

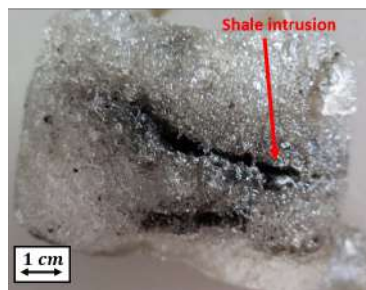


(b) Line 3 (WISDOMprototype, full polarisation). Spacing: 20 cm. Processing: FreeSpace removal

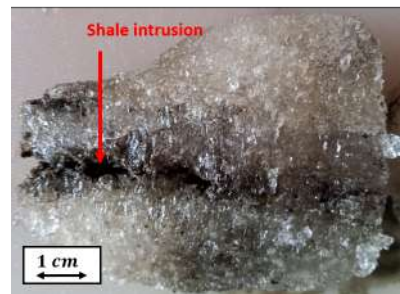
Figure 5.28: Ice crust radargrams. Note that the water-ice interface is expected to be rather flat. However, the unevenness of terrain creates an artificial wobbling line. It has not been possible to correct the topography as the Arctic DEM models do not contemplate the variations of the icy formations and the GPS used during the survey are not accurate enough for less than 1 m height variations.



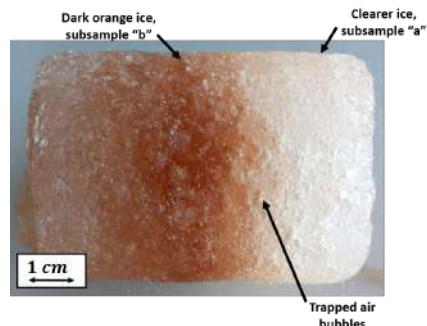
(a) Retrieved ice cores of River Bed Pingo



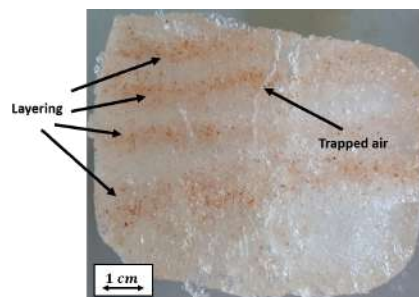
(b)



(c)



(d)



(e)

Figure 5.29: Ice core drills. (a) Ice cores at River Bed Pingo; (b) Ice core *D* sample, dark ice. (c) Ice core *D* sample, dark ice, open section after axial cut. (d) Ice core *A* sample. Clear ice subsample *Aa* and dark orange ice subsample *Ab*; (e) Ice core *C* sample

### 5.4.2.1 Salinity analysis

To shed some light on the characteristics of the ice crust of River Bed Pingo, the salinity at three representative sections of the ice cores was calculated. For this purpose, the Seven2Go™ conductivity meter was used. Table 5.8 presents the values of the different samples. At the top, one can see the conductivity and salinity values from the melted samples. In the middle of the table, the values of the corresponding relative permittivity and propagation velocity given the environment temperature at the time of the survey ( $-10^{\circ}\text{C}$  during WISDOM*prototype* survey). On the bottom the average values and standard deviation of the relative permittivity. The propagation velocity has been obtained applying the formula in eq.4.8.

The ice permittivity *SMRT* module has been used to calculate the ice permittivities, in particular three different models have been used. Mätzler and Wegmüller, 19871 and Tiuri, 1984<sup>14</sup> which only take into account the frequency at which ice is investigated and the temperature of the ice for calculating the complex permittivity of pure ice, and Mätzler et al., 2006<sup>14</sup> for saline ice calculations. The latter has a limitation for temperatures ranging between  $-5^{\circ}\text{C}$  and  $-15^{\circ}\text{C}$  while salinity is expected to be around  $0.013\text{ PSU}$ , meaning that the current ice core samples are being extrapolated with data outside the database. As expected, clearer ice samples (*IC C* and *IC A - a*) have a lower conductivity as the concentration of impurities is lower while coloured-ice samples (*IC A - b* and *IC D*) have around twofold the values of conductivity. However, these do not have an impact on  $\epsilon_r$  values which yields the same in all samples. The average and std. dev. of  $\epsilon_r$  show is that there is very little difference between the results of pure-ice permittivity models (Mätzler and Wegmüller, 19871 and Tiuri, 1984) and saline-ice models (Mätzler et al., 2006) simply because salinity is very low to make any relevant contribution.

The estimated  $\epsilon_r$  is 3.168 which results into a propagation velocity of  $0.169\text{ m/ns}$ . Note that these values are not taking into account the variations in the concentrations of mineral impurities nor the presence of trapped air bubbles or any other factor that might alter the  $\epsilon_r$  of the ice crust.

Table 5.8: Salinity values of ice core samples. The top table presents the results of the conductivity-meter. The table in the middle presents  $\epsilon_r$  and  $v$  results according to different models given the temperature at the time of the WISDOM survey ( $-10^{\circ}\text{C}$ ). On the bottom, average and std. deviation values.

	IC A-a	IC A-b	IC B	IC D
<b>conductivity</b> [ $\mu\text{S}/\text{cm}$ ]	1258	2035	1338	2406
<b>Temperature</b> (melted sample) [ $^{\circ}\text{C}$ ]	21	22.4	21.7	22
<b>salinity</b> [PSU, ppt, ‰, g/kg]	0.7	1.1	0.7	1.3
$T = -10^{\circ}\text{C}$				
$\epsilon_r$ <b>Maetzler87</b>	3.17917	3.17917	3.17917	3.17917
$v$ <b>Maetzler87</b>	0.16825	0.16825	0.16825	0.16825
$\epsilon_r$ <b>Tuiri84</b>	3.14665	3.14665	3.14665	3.14665
$v$ <b>Tuiri84</b>	0.16912	0.16912	0.16912	0.16912
$\epsilon_r$ <b>Maetzler06</b>	3.17925	3.17937	3.17925	3.17944
$v$ <b>Maetzler06</b>	0.16825	0.16825	0.16825	0.16825
<b>Average</b> $\epsilon_r$	3.16836	3.16839	3.16836	3.16842
<b>Std Dev.</b> $\epsilon_r$	0.01880	0.01883	0.01880	0.01885

<sup>14</sup>As cited in SMRT (Picard and Sandells, 2022)

## 5.5 Site 5: Sandstone Outcrop

A total of two profile lines have been recorded on the sandstone outcrop. *Line 1* is a traverse of the outcrop while *Line 2* is perpendicular to it and extends to the neighbouring soil (Figure 5.30).



Figure 5.30: Site 5, sandstone outcrop. Background map: © Norwegian Polar Institute/CC BY 4.0

merges into the sandstone blocks. More on the right-hand-side of the image an intermediate layer has been marked. In fact, it looks like a layer of soil that divides the sandstone and that disappears as it moves to the left eventually being lost under the snow. It can be observed that the upper half of the sandstone is highly weathered with very narrow foliation layers while the lower half has a more massive structure and is less weathered. This holds true as one moves to the left but it is unclear as snow covers the rest of the outcrop. If indeed the sandstone can be divided in an upper more-weathered unit and a lower less-weathered unit, this could explain why the in radargram more reflections are detected above the intermediate layer (red-dashed line) than beneath it. As it can be seen, the sandstone foliation is seen as relatively consistent semi-parallel lines. A feature not appreciated on the photograph but observed on the B-scan is the (hypothesised) sideways dipping of the sandstone (yellow dashed line).

Figure 5.31 shows the GPR line perpendicular to the traverse line. It is possible to appreciate a reflection close to the surface which has been associated to the transition between the soil layer and the sandstone. This reflection in particular was expected as it was possible to appreciate by naked eye the sandstone unit emerging from beneath the soil. Hence, the question was if the GPR will be able to detect the layer interface.

At the right-end of the radargram is possible to see the sandstone foliation and a line that seems to split once more the sandstone in two halves (intermediate layer). In fact, foliation direction differs between the upper and bottom halves. Despite not being so clear in this radargram, this line could matches in depth with the previously marked as intermediate layer for profile *Line 1*. The radargrams shows a series of very strong reflections between 10 m and 15 m depth and 7 m inward of the sandstone. Unfortunately, their separation from the exposed surface is too high to extract any substantial information.

Figure 5.32 shows the comparison between the radargram (a) and a frontal photography of the outcrop (b). In both images, certain features have been manually delineated to highlight their relevance among the rest. Starting by Figure 5.32, the blue arrows indicate the horizontal position which corresponds to the above radargram. Between position 0 m and 11 m there is a highly laminated unit that differs from the surrounding block-like rock by its long isolated horizontal layers. It seems to be a correlation with this unit and a V-shape structure detected by the GPR. Its interpretation is challenging as the feature of the radargram is in fact hidden behind the exposed rock on the image and it is not possible to see how the laminated unit

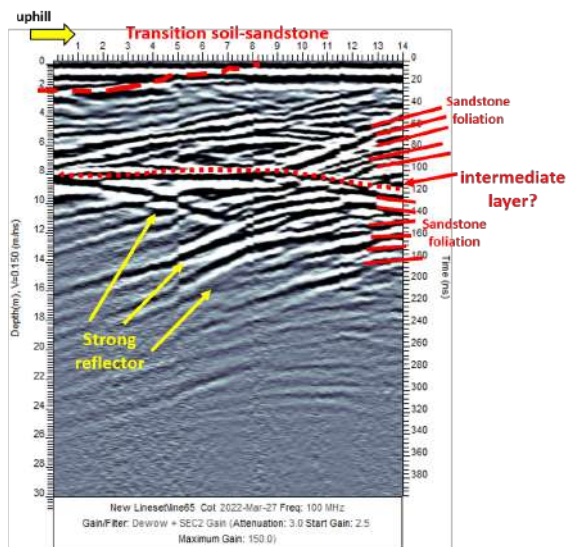
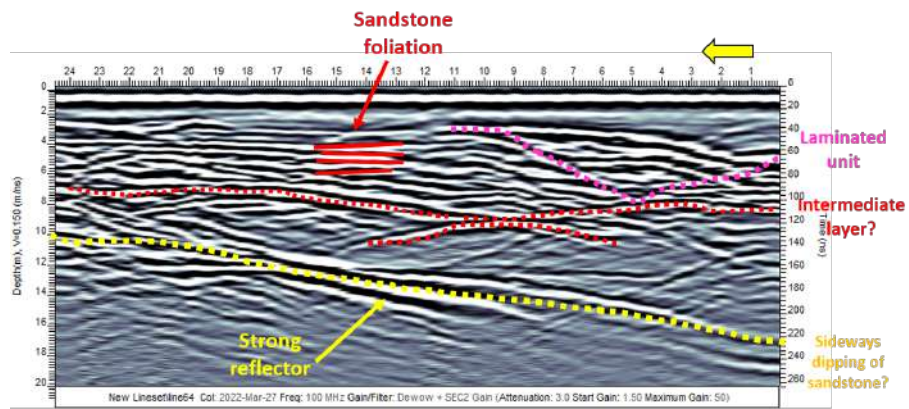
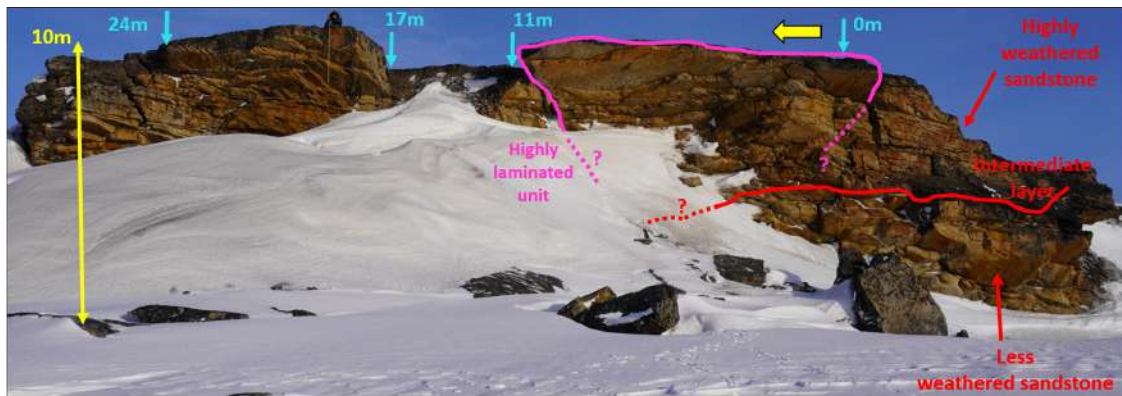


Figure 5.31: *Line 2* (pulseEKKO, config. 4). Processing: Dewow + Background Substraction + SEC2Gain



(a) Line 1 (pulseEKKO, config. 4), traverse profile of outcrop. Processing: Dewow + Background Substraction + SEC2Gain



(b) Front image of the outcrop

Figure 5.32



## 6. Discussion

### 6.1 Decrease in Longyearbreen's thickness

Historical GPR data from Longyearbreen has been recorded on an annual basis on the same locations (*Line 1* to *Line 4* on [Figure 5.2](#)) on the context of UNIS bachelor course *Cold Region Field Investigations*. These data, recorded by students themselves and although yet unpublished<sup>1</sup>, provides key information to comprehend the current trend on glacier mass loss on the Arctic, particularly Svalbard. *Line 1* was surveyed on the end of February 2012 and, exactly the same profile, 10 years later on the 1st of March 2022. The original line (2012) had 70 m extra at the start and 40 m extra at the end respect to 2022's *Line 1*. The profile length of 2022 had reduced the distance close to the edges of the glacier, first, because of a heavier bandwagon being used with respect to 2012 and second, due to a considerable thinning of the ice mass which compromised safety of the operations. Indeed, the radargrams indicate a rather quick thinning of Longyearbreen; being the ice-rock interface on 2022 closer to the glacier surface by 13 m to 16 m than it was back on 2012. This marks a loss of 1.3 to 1.6 m of ice thickness per year since UNIS recordings started.

It must be noted that calculating the mean mass balance rate of Longyearbreen is out of the scope of this project. For doing so would have been necessary a higher density of profiles at Longyearbreen consistently taken throughout the years. Nevertheless, the results obtained at *Line 1* between 2012 and 2022 agree with other GPR investigations of Svalbard glaciers. For example, Lapazaran et al., [2013](#) studied Ariebreen changes for two periods (1936-1990 and 1990-2007) concluding that the thinning rate increased from the second to the first period from  $-0.5 \pm 0.22$  to  $-0.95 \pm 0.17$  m/year leading to a 73 % loss of the glacier volume by the end of 2007.

### 6.2 Near-surface ice on South-Western flank of Innerhytta Pingo

Investigations in Innerhytta's pingo date back to more than 50 years ago, when ground ice was recorded beneath the pingo apex (Piper and Porrit, 1966 as cited by Ross et al., [2005](#)). The same investigation reported no ice on the more gentle northern slope of Innerhytta. In the more recent study of Ross et al., [2005](#), a total of two GPR profiles were retrieved, one on Innerhytta's apex and the other similar to *Line 1* recorded by WISDOM *fs2* (see [Figure 5.5](#)). The authors found strong reflectors at the south-western flank of the pingo which they describe as ice-shale alternating units or layering due to changes in the chemistry, air content or ice crystal properties of the core ice. Very similar GPR responses were recorded by pulseEKKO: the features marked at ice-rich structures on [Figure 5.7](#) are of the same type as reported by Ross et al., [2005](#) and on equivalent positions. The loop profile (*Line 3* in [Figure 5.8.b](#)) provides solid proof these reflections are caused by pingo's ground ice as they correlate with small surface ponds captured in aerial imagery. Furthermore, Ross et al., [2005](#) also describe the small ponds associating them with thermokarst processes occurring on this ground ice area of Innerhytta, presumably inactive. So, there is no reason to think the features detected during the survey are different from those described in the aforementioned study. In contrast, the north-eastern flank of Innerhytta lacks any visible GPR reflectors. The main cause attributed to the shallow penetration is the abundance of shale sediments on the first layers of soil that attenuate the signal. Considering the orientation of the pingo with respect to the mouth of Helevtidalen and the flattening of its slope towards the alluvial fan, it can be seen that this region suffers from sediment and debris accumulation washed out by the river, thus, contributing to a thick layer above the pingo's ice. Piper and Porrit, 1966 (cited by Ross et al., [2005](#)) question the presence of any massive ice and propose instead a bedrock remnant.

---

<sup>1</sup>Data on Longyearbreen's thickness is to be published on a research paper by prof.J.S.Rønning. For avoiding conflicting information (eg. radargrams with different processing steps), historical data cannot be shown in this Msc.Thesis, but only commented.

## 6.3 Ice Wedge Polygons

### 6.3.1 Geomorphometric analysis

The importance of geomorphometric statistical analysis is noting any particular pattern in the polygon geomorphology and its spatial manifestation that might later be linked to the corresponding wedge ice distribution according to the GPR survey. While results might lack statistical relevance, that is to say, unable to be extrapolated for a random-sized polygon sample, they still describe a localised behaviour. Secondly, it is also relevant to characterise the area in order to evaluate its divergence from a broader, well-studied region. Thus, it can be established if the subsample itself is an outlier or is representative of the whole region. The ice wedge polygons at Site 3 constitute a small subsample (approximately 10 times less in extension and number of polygons) from region AD 2 Ulrich, 2011 which consists of 214 polygons in an area of  $186 \cdot 10^3 m^2$ . The same study reports correlations between the slope angle and either the polygon shape or dimension, for example, polygon elongation being parallel to gentle slope contours. In contrast, results on Site 3 show polygons are smaller but with a similar shape than AD 2 and indicate no correlation between geotopographical features and polygon geometrical characteristics.

Nevertheless, lack of correlations might also indicate inadequacy in the choice of parameters. While gravitational effects due to steep sloped terrain has direct effects on the orientation of polygons as it affects the direction of primary thermal contraction cracking (Mackay and Burn, 2002), this might as well be caused by other factors also affected by the slope such as grain-size distribution, moisture content, vegetation cover, etc (Ulrich, 2011). Another example of differences in choice of parameters is in Andres, 2020, where the trough depth is included in the statistical analysis and a LiDAR was used to retrieve accurate and cm-scale high-resolution of the local topography.

In summary, the geomorphometric analysis of Site 3 should be taken as a rather simplified description of the polygon network with results that apply locally.

### 6.3.2 Correlation between GPR reflections and ice wedge polygon features

One of the most challenging problems during the GPR survey on ice wedge polygons is to actually ensure troughs and/or wedge ice is detected, and not misinterpreting the signal with other structures such as stones. In addition, the relative position between the trough and the GPR is also relevant to understand the visualisation on the radargrams. While it is technically possible to change the antenna configuration in order to optimise the detection of underground features, pulseEKKO's was restricted by the sledge to operate exclusively on PR-BD. The WISDOM units, being more versatile on this regard (as they can choose antenna polarisation without changing their physical configuration) show that, indeed, the single polarisation recognises clearer the bottom of the troughs. Still linked to antenna configuration and the detection of target features underneath, all GPR units struggle to distinguish the polygon features when surveying parallel to the troughs whereas crossing them perpendicularly proves to be the most favourable. This is by no means unexpected, GPR response is triggered by changes in the dielectric constant of the media. Once the GPR unit is surveying inside the trough, if there is no sufficient contrast between the trough filling material and the soil beneath (eg. snow vs. shale) it will hardly be observed. The WISDOM unit has proven the best performance to detect the trough bottom interface. The high-frequency system penetrates enough to neatly show the trough interface, nonetheless and rather curiously, no reflectors are hyperbolic. PulseEKKO's radargrams are coarser but allow to estimate the propagation velocity by hyperbola fitting.

The dilemma of whether a reflector is caused by the trough or the wedge ice cannot be solved without ground truth information. So far, it can be summarised that:

- i The sources of hyperbolic reflections in the study area are mostly caused by stones, troughs and ice wedges (usually beneath visible troughs). Other sources might be localised changes in soil composition, buried structures and even vegetation. The stronger GPR responses correlate directly

with the presence of troughs while the rest cause single hyperbolic reflections.

- ii Some troughs present stronger reflections than others. An obvious answer would be more prominent troughs vs. shallower ones, but this does not explain cases of similar-sized troughs (according to aerial imagery) where one has distinctively multiple reflections. In some cases, even in the absence of a visible trough on aerial images there are strong secondary hyperbolic reflections that are either provoked by a buried boulder, or most probably, by ice wedges.
- iii Multiple hyperbolic reflectors are associated with higher chances of wedge ice beneath the trough. Actually, the ice would be responsible for the repeated signal echos, being detected up to depths of approximately 7 m with the 100 MHz system. This is because the GPR response relies on the dielectric contrast between the frozen ground and the wedge ice, which results in multiple reflections from the wedge acting as point source (Bode et al., 2007).
- iv The wedge ice depth cannot be estimated by the GPR readings. The depth distribution of the reflectors is actually due to time delay of the multiple reflections and not necessarily corresponding at different stratifications of the ice wedge. Furthermore, hyperbolas are mainly centered at the top of the ice wedge rather than at the bottom (Bode et al., 2007). In other words, multiple reflectors reaching up to 7 m do not indicate a 7 m deep ice wedge, these reflections represent the multiple echos mainly caused at the interface between the soil and upper region of the ice wedge.

### 6.3.3 Estimation and Distribution of wedge ice

According to the findings for single GPR lines commented on Section 6.3.2 it has been possible to map the distribution and estimate the amount of wedge ice on Site 3 and compare it with estimations based on only-aerial imagery data.

The role of GPR data has been to determine the regions in which wedge ice is found. Radargrams *per se* do not provide the necessary information to estimate the quantity, this must be complemented by ground truth or findings from other studies. For instance, Ulrich et al., 2014 Table.1. recompiles different ice wedges dimensions in which depth can range from barely 1 m to 20 m depending on the type of deposit. The study of Watanabe et al., 2013 in Kapp Linné reports relatively small polygons (ca. 5-15 m in diameter) with troughs between 0.2 cm and 0.6 cm and in which ice wedges reach up to 270 cm. These literature values have been plotted in Figure 6.1 in which can be seen that there is a correlation between the width of the trough and the depth of the ice wedge. In particular, the depth of the ice wedge is approximately 2.7 times its width. Taking into account that some depths might reference the depth at which the bottom of the ice wedge was found without accounting for the active layer thickness, it has been followed a conservative approach assuming that the ice wedge depth is 2 times that of its width. So, with the trough width obtained in GIS is 3 m and knowing that the trough width is very close to ice wedge width (Matsuoka et al., 2018), then an ice wedge depth of 6 m is estimated. In addition, two different shapes best model an ice wedge: an inverted isosceles trapezoid for syngenetic wedges (Ulrich et al., 2014) and a V-shape inverted isosceles triangle for epigenetic wedges (Mackay, 1990). Cable et al., 2018 investigated the cryostructure as well as soil characteristics (desposit type, silt and clay content, total carbon, gravimetric moisture content and excess ice content) and drilling cores on solifluction lobe S7 (a location 500 m to the North-East of the Site 3 polygon network) show cryostructures compatible with syngenetic and quasi-syngenetic permafrost formation. Therefore, the shape that most likely describes the ice wedges in the target polygon network is the inverted trapezoid. Nonetheless, an inverted isosceles triangle shape is chosen for simplicity -as the trapezoidal shape introduces an additional degree of freedom to determine (the bottom width of the ice wedge)- and lack of ground truth data.

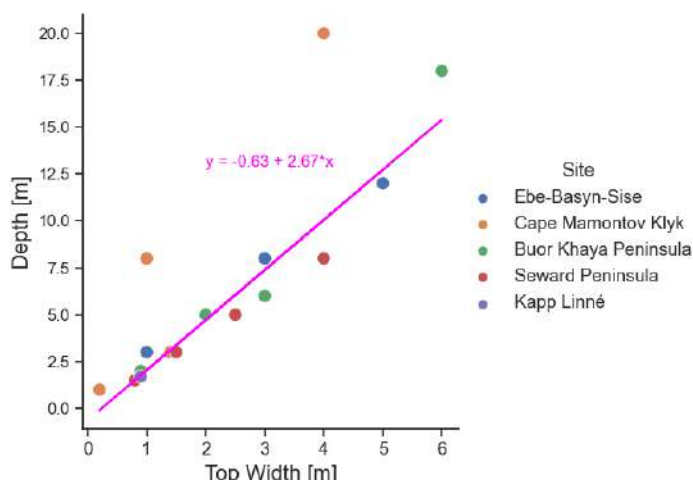


Figure 6.1: Ice Wedge width vs. depth. Data from Ulrich, 2011 except for Kapp Linné (Watanabe et al., 2013). Plot own elaboration. Note that the two outliers of *Cape Mamontov Klyk* have not been included in the interpolation. Also for Kapp Linné depths the active layer has been subtracted.

wedge ice is discontinuous across the trough with gaps narrower than the grid spacing after interpolation it will be either under or overestimated. Despite this, data retrieved is not considered unrealistic as both grids show similar GPR patterns in same areas despite halving the grid spacing. Polygon 8 is located at the centre of the small grid (see Figure 5.23) with 4 lines crossing it on the North-South direction and 4 on the East-West direction, clearly displaying strong reflectors on the top and bottom troughs only. With half the lines crossing it, the large grid records the strongest reflectors also at top and bottom troughs, overestimating the western trough (see Figure 5.23).

The approach to estimate wedge ice has been choosing a maximum contrast depth slice and masking it within the limits of the troughs as Figure 5.25 (a), (b) and (c) show. The depth of the slice is not that meaningful on its own, rather being an approximate depth at which ice wedge signals can be better distinguished from the rest of near-surface objects detected by the GPR. In fact, it must be noted that after migrating data there is a subtle shift downwards of 0.5 m (see Figure 5.16.a for unmigrated data and Figure 5.16.b for the same profile migrated). On the other hand, masking the interpolation is chosen due to the limitations of the Kirchoff Migration already commented on Section 5.3.2.3 which result in a scattered reflection. By doing the masking, some GPR reflections that suggest wedge ice despite not occurring within trough limits are discarded; Figure 5.20.b marks such a region. As these events are exceptional and very localised, their contribution to the total wedge ice is negligible.

Wedge ice volume (WIV) is estimated by GIS and GPR maps. As there are no previous investigations on wedge ice done in Site 3, results obtained are compared to Ulrich et al., 2014 Table 1. GIS-derived WIV vol.% are in accordance to estimations with minimum values obtained for Yedoma<sup>2</sup> deposits, whereas GPR-derived WIV vol.% are considerably lower but matching also with minimum results for thermokarst deposits. The latter seem rather low values taking into account that Site 3 polygons are approximately 100 m a.s.l and the further they are from the sea level, the older they are supposed to be, dating back to the Weichselian Period (Sørbel and Tolgensbakk, 2002) thus, apparently being more similar (at least period-wise) to the Yedoma deposits .

The distribution of wedge ice is the most unexpected as no correlations between geomorphometric and topographic parameters were found. Nevertheless, maps show there is an obvious lack of GPR reflections on the northern flank of the polygon network corresponding to those polygons at higher elevations, barely

<sup>2</sup>Pleistocene ice-rich permafrost with syngenetic ice-wedges.

7 m above the southern flank counterparts. One possibility might be that narrower troughs causing weaker signals have been misinterpreted to be stones or other point reflectors but this does not explain the general trend of stronger reflectors downhill (Figure 5.25 (d), (e) and (f)). Furthermore, it can be observed on aerial imagery that in the northern flank there are prominent, wide troughs.

On a final note, this project's approach and (to the best of knowledge) other studies that estimate the wedge ice volume and distribution assume constant trough width and ice wedge depth. This is far from accurate. Troughs vary in not only width but also shallowness, ice wedges also might present irregularities on their shape and their vertical extent, etc. Hence, results should be taken as preliminary and an approximate order of magnitude. In Andres et al., 2020 ice wedge volumes are calculated by isosurface generation using 3D-GPR, modelling individually size and shape of the ice wedge, which theoretically should yield closer-to-reality results. This approach is unfeasible for this project as it is not possible to separate reflections originating from the top vs. the bottom of the ice wedge (see Section 6.3.2).

## 6.4 Attenuation and Salinity at River Bed Pingo

River Bed Pingo has been the site at which results were most unexpected. In Ross et al., 2005 similar profiles were done on top of the pingo and the northern flank, with a gentler slope. In their study, some ice-shale injections could be distinguished in form of chaotic layers at the top of River Bed Pingo, at least, indicating the presence of ice structures. Their study did not include profiles on the southern slope due to its steep slope. Hence, this slope was marked as a region of great interest as it had not been profiled beforehand and promised to improve the already existing investigations. Moreover, according to Yoshikawa, 1993 the southern slope sediment layer could be as thin as 1 m thickness and core ice was to be found beneath. The results obtained in this fieldwork campaign, or rather, the lack of results, raise questions if investigations that date back to almost three decades ago do still accurately describe the River Bed Pingo ice core status. New ground truth information is paramount to obtain as the southern flank sediment layer might have become thicker or slowly the ice core has been retreating. Yoshikawa, 1993 already describes inactivity of the River Bed Pingo and the formation of a talik beneath the river bed, between 5 to 5.5 m depth. The latter is what we describe during the survey apparently with a larger extension: ponds most of them with a thick ice crust on top associated with groundwater surcharge.

Salinity results on the ice cores only show a low to mild salinity that does not seem to explain the large attenuation on the pingo itself. Groundwater salinity was not measured directly but values are not expected to be much higher than the ice crust. Thus, the strong attenuation is mainly attributed to the shale-rich sediments on top of the pingo.

## 6.5 Geological structure of the Sandstone Outcrop

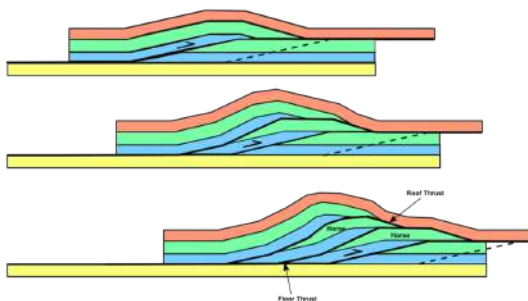


Figure 6.2: Example of simple duplex structure (thrust fault) showing different stacking of thrust faults. Image credit: Mike Norton/CC-BY-SA-3.0

The targeted sandstone outcrop is located in a region surrounded by sandstone mountains of the Advendalen Group (Carolinefjellet Formation and Helvetiafjellet Formation) also characterised by siltstone, shale and conglomerates (Major et al., 2000). The outcrop itself is marked in NPI's geological maps as a reverse fault, in particular the symbology indicates an overthrust fault. According to Gwinn, 2006 an overthrust fault is defined as a type of fault in which the rock mass moves over one another along a flat or slightly inclined plane, being the upper rock the active element of the process (hanging wall). Figure 6.2 illustrates a type of overthrust fault in which structures stack in slices, overlapping over one another and eventually displaying a lenticular shape.

By comparing this type of formation with the transversal line (*Line 2*, Figure 5.31) taken at the outcrop seems compatible to associate clusters with same foliation direction with different rock stackings.

Further observation of the geological maps as well as aerial imagery helps to better comprehend the rest of the GPR readings. Figure 5.32.a shows a strong, sideways reflector all across the profile that cannot be contrasted with ground truth information. It has been assumed to be a sideways dipping of the sandstone just as Figure 6.3.c depicts. For supporting this assumption one can look into Figure 6.3.a in which it is possible to see a slight tilt of the sandstone: it emerges on the North-West and sinks into the soil on the South-East. A series of question marks below what would correspond to the bottom reflector on the GPR profile have been added as it is not clear if it is caused by the sandstone-soil interface or a sandstone-sandstone discontinuity due to the fault.

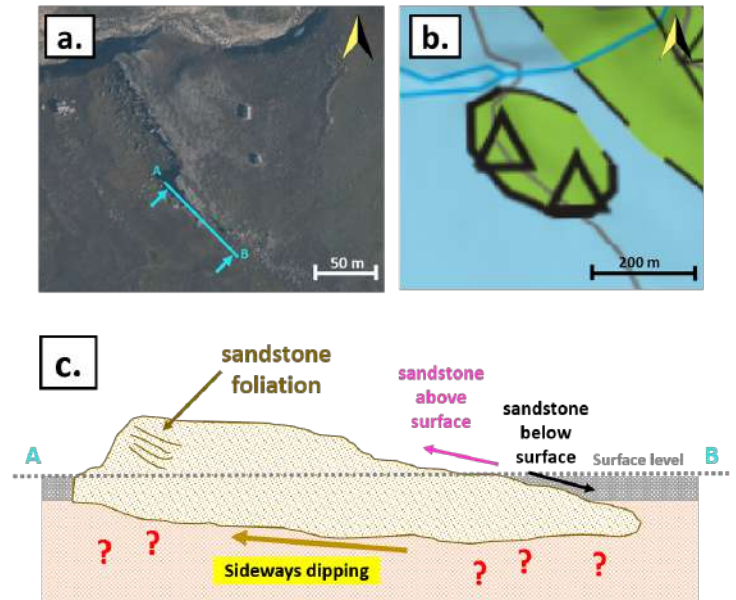


Figure 6.3: Sandstone fault. Image credit (a,b): © Norwegian Polar Institute/CC BY 4.0

## 6.6 Active Layer

### 6.6.1 Estimation of the active layer thickness

The permafrost table can be detected in radargrams as almost horizontal lines due to the ice-rich bottom of the active layer (Hinkel et al., 2001; Munroe et al., 2007). The dielectric contrast is expected to be more evident if the thermal transition occurs between a thawed active layer and the permafrost underneath. Nonetheless, Hinkel et al., 2001 investigations take place in winter and also show the lateral traces of the frost table. The radargrams for this project's campaign present several challenges to determine the active layer thickness (ALT) for distinct reasons:

- i Both pingo profiles present high attenuation and most importantly, as they are open-system pingos they have formed above the -discontinuous- layer of permafrost. So, the soil covering the pingo's ice core is the active layer only.
- ii The alluvial fan profiles have a penetration depth of ca. 5 m which should be well below the permafrost table. However, the GPR detects different soil layers from sediment accumulation displayed laterally. Thus, it is not possible to distinguish between soil layering and the frost table.
- iii Ice wedge profiles are the most suitable to estimate the ALT. According to Hinkel et al., 2001 the top of the ice wedge is usually coincident with the *long term* frost table. However, the same author warns of overlying horizontal reflections that might mask the true tops of the ice wedges, hence, making them unreliable to depth-scale radar profiles. Moreover, pulseEKKO's radargrams have far too low resolution to determine the exact depth at which the reflections occur. On the other hand, WISDOM profiles attenuate very rapidly only showing the snow-soil interface without revealing the

frost table. In (Cable et al., 2018) a ALT of 1.19m is reported but it cannot be assumed to be the same at the polygon network as significant differences might exist just above ice wedges compared to polygon centres (as shown in Watanabe et al., 2013). All in all, it is necessary to retrieve core samples to determine the ALT.

### 6.6.2 Shallow penetration with frozen active layer

One of the surprising things during the GPR campaign was the low GPR penetration despite taking place in the Arctic winter, with temperatures as low as  $-22^{\circ}\text{C}$ . Some of the GPR studies cited (eg. Andres, 2020; Watanabe et al., 2013) occur in summer months when the active layer has thawed. This conditions are not ideal for GPR investigations as there is an increase of moisture content on the soil that greatly attenuates the signal. Thus, it was expected that the cold conditions improved the penetration depth. In fact, it can be concluded that the shale-rich soil was the main driver for attenuation. The best pulseEKKO's performance depth-wise (excluding Longyearbreen) is on the ice-rich structures of Innerhytta's Pingo reaching up to ca.10-15 m depth, where sediment content is known to be much lower. On the opposite end, River Bed Pingo had such strong attenuation and surface clutter that no feature could be seen even for a frequency of 100 MHz.

From the perspective of future GPR investigations, a key parameter to investigate would be the soil's unfrozen water content, both in the active layer and the permafrost. In Watanabe et al., 2013 and Matsuoka et al., 2018 ground conditions at ice wedge polygons are studied throughout the seasons for several years and it is clear that water content diminishes in winter and increases summer; meaning that the voids filled with water during the warmer months become filled with air once the seasonal freezing starts. So, conditions are more favourable for GPR investigations as temperature drops and the remaining water freezes, but how much water remains unfrozen? Salinity and capillarity effects on fine grained soils will lower the freezing point of water, resulting in a part of the content not turning into ice. Coastal Adventdalen drillings have proven the presence of cryopegs<sup>3</sup> as far as 12 to 18 m deep (Gilbert et al., 2019). Hence, calibrating the unfrozen water content would provide a better understanding of the signal propagation when performing GPR surveys.

---

<sup>3</sup>Pockets of unfrozen ground.

## 7. Conclusions

This project analyses distinctive periglacial geomorphologies combining GPR soundings with aerial imagery as well as ground truth information such as snow probing, ice core drilling, soil sample collection, landscape observations and geological maps. The fieldwork campaign has demonstrated the versatility of GPR systems and the advantages this technique poses, collecting large amounts of data in relatively short time and without altering the surveyed environment. However, the study makes evident the imperative necessity of complementing the GPR gathered-data with as much as additional information as possible, from simple descriptions of the environment to actual samples to-be-analysed on a laboratory. The main limitation of the GPR systems has been soil attenuation which was thought to be, partially, balanced out by the low temperatures and a frozen active layer. In fact, depth penetration in shale-rich sediment soils does not show significant improvements from summer surveys, drawing attention to the actual content of unfrozen water in both active layer and permafrost.

The study on the ice wedge polygon network shows the difficulties of GPR soundings in these type of periglacial environments. While wedge ice triggers an hyperbolic response on the radargrams, without ground truth is challenging to distinguish it from point sources (such as stones) or to unequivocally determine that the response was caused by the ice wedge and not the trough itself. Precisely, changes in the terrain geometry (for eg. the steep slop from a deep trough to a polygon high-center) can provoke strong reflectors in GPR readings. Despite these sources of misinterpretation, GPR mapping indicates that reflectors at depth slice  $z = 3.5\text{ m}$  and beyond concentrate almost exclusively on polygon's troughs, suggesting that these are caused either by prominent troughs or wedge ice. Hence, a depth slice with a high contrast of GPR responses (instead of low-contrast scattered ones) is chosen to estimate the ice wedge volume, being  $z = 4\text{ m}$ <sup>1</sup>. An additional challenge is that the detected depth at which reflectors fade in the radargram does not necessarily correlate to the actual depth of the ice wedge. Indeed, the contrast between dielectric constants (soil and ice) at the top of the ice wedge triggers the hyperbolic signals, even multiples of it. Thus, it is necessary to know from an independent method the depth of the ice wedges.

The 21-polygon network has proven to be too small for any significant correlations between geomorphometric parameters and geographical ones. Surprisingly, despite the lack of such correlations there is an obvious southern-distribution of ice which would correspond to those polygons at lower elevations. That is to say, the GPR survey detects a predominance of wedge ice downslope. These results contrast with estimations purely based on remote sensing observations, that predict a WIV between 14.84% and 15.14% in volume, whereas GPR estimations range from 1.49% to 4.49%.

In this research, pulseEKKO's investigations do not only contribute on a better understanding of GPR performance in periglacial environments (specifically ice wedge polygons) but also hope to improve interpretation of WISDOM's radargrams. Glacier and ice wedge polygon measurements have yield the most promising results, having been able to detect the target features (eg. meltwater channel and top of ice wedge). As expected, WISDOM's high central frequency handicaps its penetration when the soil is not extremely dry. Despite a frozen AL, the presence of clay and shales and the high probability of unfrozen water content in the soil has limited most soundings to the first meter and meter and a half below the surface level. On the other hand, the GPR readings at Innerhytta surface show variations in the signal response according to differences on surface characteristics (peble size, snow covered terrain vs. bare rock). This requires further analysis as WISDOM is able to estimate the dielectric constant of the shallow subsurface according to the surface echo. Overall and from the point of view of the ExoMars GPR, the Svalbard campaign constitutes an essential training for data analysis and processing before the WISDOM unit deals with actual martian subsurface signatures.

---

<sup>1</sup>In the case of the large grid.



## 8. Further work

During the project, several areas of interest arose but could not be assessed due to time constraints. In the first place, given more time and resources, drillings and core drillings at different points of interest would have been done. For example, at least one core sample and different drillings at Innerhytta's ground ice region, a drilling investigation on the southern slope of River Bed Pingo to determine the depth of the massive core ice, some core samples at the alluvial fan to determine the layering and ALT, etc. In fact, some of the drillings were originally planned as well as a posterior index testing (grain size distribution, water content, density, salinity...), but simply all drilling attempts failed. Some of this work is undertaken by TU Dresden team, who will analyse several soil samples retrieved at different study sites and calculate the dielectric constant on pebbles and rocky material from the pingos and sandstone outcrop.

Nonetheless, the region of interest of most relevance are the ice wedge polygons. Further investigations should target the different GPR responses in combination with aerial imagery performing drillings to verify the existence of wedge ice and core sample retrievals to study the type of ice. In particular, for a given trough, three different scenarios have been identified after analysing the GPR grids: (1) the presence strong reflector on the radargram and an identifiable trough on aerial images; (2) the presence of a strong reflector without identifiable trough features; (3) weak or non-existent reflector with the presence of an identifiable trough. Cases 2 and 3 deserve special attention because pose situations in which remote sensing data and GPR soundings apparently disagree.

In addition, it would be of interest performing a GPR mapping in a vaster area to corroborate the findings in wedge ice distribution and analysing in a larger sample the correlations in geomorphometric parameters of polygon networks. In that case, it would be necessary a much faster algorithm to delineate the polygon network recorded in aerial imagery. For example, combining computer vision and machine learning would be possible to fully-automatise the polygon network making its extension no longer a constraint (current line of work).

Finally, this project opens the door to future UNIS collaborations with LATMOS (Le Laboratoire Atmosphères, Observations Spatiales), TU Dresden and other ESA collaborators -and even companies- in the framework of space exploration. Svalbard is a unique place in the Arctic by its climate, geology, flora and fauna, which despite its remoteness, gathers hundreds of world-wide scientists to conduct state-of-the-art research. Perhaps the next step for the small Arctic archipelago is becoming an innovation hub for space science and as analog for icy worlds in our Solar System.

# Bibliography

- ACGR (1988). “Glossary of permafrost and related ground ice terms”. In: *Permafrost Subcommittee, Associate Committee on Geotechnical Research*.
- Andres, C. N., G.R. Osinski, and E. Godin (2020). “3D-Modelling of Subsurface Ice using Ground Penetrating Radar on Axel Heiberg Island, Canadian High Arctic”. In: *Seventh Mars Polar Science Conf. 2020 (LPI)*. Vol. 2020. 2099, pp. 3–4.
- Andres, Chimira Nicole (Oct. 2020). “A Periglacial Landsystem Analysis in the Canadian High Arctic: A Tool for Planetary Geomorphology”. PhD thesis. URL: <https://ir.lib.uwo.ca/etd/7528>.
- Annan, A. Peter (Aug. 2005). “GPR Methods for Hydrogeological Studies”. In: *Hydrogeophysics*. Springer Netherlands, pp. 185–213. DOI: [10.1007/1-4020-3102-5](https://doi.org/10.1007/1-4020-3102-5). URL: [https://link.springer.com/chapter/10.1007/1-4020-3102-5\\_7](https://link.springer.com/chapter/10.1007/1-4020-3102-5_7).
- Archer P. D., Jr. et al. (2016). “Oxychlorine species on Mars: Implications from Gale Crater Samples”. In: *AGUFM*, P23B–2169. URL: <https://ui.adsabs.harvard.edu/abs/2016AGUFM.P23B2169A/abstract>.
- Bælum, K. and D. I. Benn (2011). “Thermal structure and drainage system of a small valley glacier (Tellbreen, Svalbard), investigated by ground penetrating radar”. In: *Cryosphere* 5.1, pp. 139–149. ISSN: 19940416. DOI: [10.5194/tc-5-139-2011](https://doi.org/10.5194/tc-5-139-2011).
- Balanis, Constantine A (2012). *Advanced engineering electromagnetics*. John Wiley & Sons.
- Benedix, Wolf Stefan et al. (2013). “Advance of WISDOM GPR antenna for ExoMars 2018 mission”. In: *IEEE International Conference on Wireless for Space and Extreme Environments, WiSEE 2013 - Conference Proceedings*. IEEE Computer Society. ISBN: 9781479929580. DOI: [10.1109/WiSEE.2013.6737553](https://doi.org/10.1109/WiSEE.2013.6737553).
- Bernard-Grand'Maison, C and W Pollard (2018). “An estimate of ice wedge volume for a High Arctic polar desert environment, Fosheim Peninsula, Ellesmere Island”. In: *The Cryosphere* 12.11, pp. 3589–3604. DOI: [10.5194/tc-12-3589-2018](https://doi.org/10.5194/tc-12-3589-2018). URL: <https://tc.copernicus.org/articles/12/3589/2018/>.
- Berthling, Ivar et al. (2000). “Rock glaciers on Prins Karls Forland. II: GPR soundings and the development of internal structures”. In: *Permafrost and Periglacial Processes* 11.4, pp. 357–369. ISSN: 10456740. DOI: [10.1002/1099-1530\(200012\)11:4<357::AID-PPP366>3.0.CO;2-6](https://doi.org/10.1002/1099-1530(200012)11:4<357::AID-PPP366>3.0.CO;2-6).
- Bibring, Jean Pierre et al. (Mar. 2005). “Mars surface diversity as revealed by the OMEGA/Mars express observations”. In: *Science* 307.5715, pp. 1576–1581. ISSN: 00368075. DOI: [10.1126/science.1108806](https://doi.org/10.1126/science.1108806). URL: <https://pubmed.ncbi.nlm.nih.gov/15718430/>.
- Bocco, Gerardo (1991). “Gully erosion: processes and models”. In: *Progress in Physical Geography* 15.4, pp. 392–406. ISSN: 07264801. DOI: [10.1007/978-3-642-41714-6](https://doi.org/10.1007/978-3-642-41714-6).
- Bode, Jenifer A et al. (2007). “Estimation of Ice Wedge Volume in the Big Lake Area , Mackenzie Delta , NWT , Canada Excess Ground Ice and Land Subsidence”. In: i.December, pp. 131–136.
- Cable, Stefanie, Bo Elberling, and Aart Kroon (2018). “Holocene permafrost history and cryostratigraphy in the High-Arctic Adventdalen Valley, central Svalbard”. In: *Boreas* 47.2, pp. 423–442. ISSN: 15023885. DOI: [10.1111/bor.12286](https://doi.org/10.1111/bor.12286).
- Cassidy, N. (2008). “Introduction to GPR”. In: *Workshop at the 12th International Conference on Ground Penetrating Radar*, pp. 10, 14, 19.
- Catto, N. R. (1993). “Morphology and development of an alluvial fan in a permafrost region, Aklavik Range, Canada”. In: *Geografiska Annaler, Series A* 75 A.3, pp. 83–93. ISSN: 0435-3676. DOI: [10.1080/04353676.1993.11880387](https://doi.org/10.1080/04353676.1993.11880387).
- Christiansen, H. H. et al. (Apr. 2010). “The thermal state of permafrost in the nordic area during the international polar year 2007-2009”. In: *Permafrost and Periglacial Processes* 21.2, pp. 156–181. ISSN: 10456740. DOI: [10.1002/ppp.687](https://doi.org/10.1002/ppp.687). URL: <https://onlinelibrary.wiley.com/doi/10.1002/ppp.687>.
- Christiansen, Hanne H. (2005). “Thermal regime of ice-wedge cracking in Adventdalen, Svalbard”. In: *Permafrost and Periglacial Processes* 16.1, pp. 87–98. ISSN: 10456740. DOI: [10.1002/ppp.523](https://doi.org/10.1002/ppp.523).
- Christiansen, Hanne H., Ole Humlum, and Markus Eckerstorfer (Feb. 2013). “Central Svalbard 2000–2011 Meteorological Dynamics and Periglacial Landscape Response”. In: *Arctic, Antarctic, and Alpine Research* 45.1, pp. 6–18. ISSN: 1523-0430. DOI: [10.1657/1938-4246-45.16](https://doi.org/10.1657/1938-4246-45.16). URL: <https://www.tandfonline.com/doi/full/10.1657/1938-4246-45.16>.
- Christiansen, Hanne H., Norikazu Matsuoka, and Tatsuya Watanabe (Oct. 2016). “Progress in Understanding the Dynamics, Internal Structure and Palaeoenvironmental Potential of Ice Wedges and Sand Wedges”. In: *Permafrost and Periglacial Processes* 27.4, pp. 365–376. ISSN: 10456740. DOI: [10.1002/ppp.1920](https://doi.org/10.1002/ppp.1920). URL: <https://onlinelibrary.wiley.com/doi/10.1002/ppp.1920>.
- Ciarletti, Valérie et al. (2011). “WISDOM GPR Designed for shallow and high-resolution sounding of the martian subsurface”. In: *Proceedings of the IEEE*. Vol. 99. 5. Institute of Electrical and Electronics Engineers Inc., pp. 824–836. DOI: [10.1109/JPROC.2010.2100790](https://doi.org/10.1109/JPROC.2010.2100790).
- Ciarletti, Valérie et al. (2015). “Modelling the performances of the WISDOM radar on the Oxia Planum potential landing site for ExoMars”. In: *EPSC Abstracts* 10.
- Ciarletti, Valérie et al. (June 2017). “The WISDOM Radar: Unveiling the Subsurface Beneath the ExoMars Rover and Identifying the Best Locations for Drilling”. In: *Astrobiology* 17.6-7, pp. 565–584. ISSN: 15311074. DOI: [10.1089/ast.2016.1532](https://doi.org/10.1089/ast.2016.1532). URL: <http://www.liebertpub.com/doi/10.1089/ast.2016.1532>.
- Daniels, Jeffrey J (2000). “Ground Penetrating Radar Fundamentals”. In: *USEPA Publication Appendix*, pp. 1–21. ISSN: <null>. URL: [papers2://publication/uuid/B797387B-354B-4A17-98D7-FBEB34EF590B](https://pubs2://publication/uuid/B797387B-354B-4A17-98D7-FBEB34EF590B).
- Davis, J. L. and A. P. Annan (July 1989). “Ground-Penetrating Radar For High-Resolution Mapping of Soil & Rock Stratigraphy”. In: *Geophysical Prospecting* 37.5, pp. 531–551. ISSN: 0016-8025. DOI: [10.1111/j.1365-2478.1989.tb02221.x](https://doi.org/10.1111/j.1365-2478.1989.tb02221.x). URL: <https://onlinelibrary.wiley.com/doi/10.1111/j.1365-2478.1989.tb02221.x>.

- Dobinski, Wojciech. 2011. *Permafrost. Earth-Science Reviews*. ISSN: 00128252. DOI: [10.1016/j.earscirev.2011.06.007](https://doi.org/10.1016/j.earscirev.2011.06.007).
- Dong, Y. and F. Ansari (2011). "Non-destructive testing and evaluation (NDT/NDE) of civil structures rehabilitated using fiber reinforced polymer (FRP) composites". In: *Service Life Estimation and Extension of Civil Engineering Structures*. Elsevier, pp. 193–222. DOI: [10.1533/9780857090928.2.193](https://doi.org/10.1533/9780857090928.2.193).
- Doolittle, James and Frederick Nelson (July 2009). "Characterising relict cryogenic macrostructures in mid-latitude areas of the USA with three-dimensional ground-penetrating radar". In: *Permafrost and Periglacial Processes* 20.3, pp. 257–268. ISSN: 10456740. DOI: [10.1002/ppp.644](https://doi.org/10.1002/ppp.644). URL: <https://onlinelibrary.wiley.com/doi/10.1002/ppp.644>.
- Horizon, S. et al. (2016). "Performance validation of the ExoMars 2018 WISDOM GPR in ice caves, Austria". In: *Planetary and Space Science* 120, pp. 1–14. ISSN: 00320633. DOI: [10.1016/j.pss.2015.10.008](https://doi.org/10.1016/j.pss.2015.10.008). URL: <http://dx.doi.org/10.1016/j.pss.2015.10.008>.
- Dundas, Colin M. and Alfred S. McEwen (Jan. 2010). "An assessment of evidence for pingos on Mars using HiRISE". In: *Icarus* 205.1, pp. 244–258. ISSN: 00191035. DOI: [10.1016/j.icarus.2009.02.020](https://doi.org/10.1016/j.icarus.2009.02.020).
- ESA. 2020. *ESA - Robotic Exploration of Mars - ExoMars Rover Rosalind Franklin*. URL: <https://exploration.esa.int/web/mars/-/45084-exomars-rover>. Accessed: 2022-01-13.
- Etzelmüller, Bernd et al. (2000). "Glacier characteristics and sediment transfer system of Longyearbreen and Larsbreen, western Spitsbergen". In: *Norsk Geografisk Tidsskrift* 54.4, pp. 157–168. ISSN: 00291951. DOI: [10.1080/002919500448530](https://doi.org/10.1080/002919500448530).
- Fitterman, D V (2015). *Tools and Techniques: Active-Source Electromagnetic Methods*. Vol. 11. Elsevier B.V., pp. 295–333. ISBN: 9780444538031. DOI: [10.1016/B978-0-444-53802-4.00193-7](https://doi.org/10.1016/B978-0-444-53802-4.00193-7). URL: <http://dx.doi.org/10.1016/B978-0-444-53802-4.00193-7>.
- Fortier, Daniel and Michel Allard (2004). "Late Holocene syngenetic ice-wedge polygons development, Bylot Island, Canadian Arctic Archipelago". In: *Canadian Journal of Earth Sciences* 41.8, pp. 997–1012. ISSN: 00084077. DOI: [10.1139/E04-031](https://doi.org/10.1139/E04-031).
- Frederick, J.M. et al. (2016). "The Arctic Coastal Erosion Problem". In: *Sandia Report SAND2016-9*, p. 122.
- French, Hugh M. 2015. "Periglacial Landform". *The Canadian Encyclopedia - Historica Canada*. URL: [www.thecanadianencyclopedia.ca/en/article/periglacial-landform](http://www.thecanadianencyclopedia.ca/en/article/periglacial-landform). Accessed: 2021-12-07.
- French, Hugh M (2017). *The periglacial environment*. 4th Editio. John Wiley & Sons, Ltd.
- Gacitúa, Guisella et al. (2012). "Estimations of moisture content in the active layer in an Arctic ecosystem by using ground-penetrating radar profiling". In: *Journal of Applied Geophysics* 79, pp. 100–106. ISSN: 09269851. DOI: [10.1016/j.jappgeo.2011.12.003](https://doi.org/10.1016/j.jappgeo.2011.12.003). URL: <http://dx.doi.org/10.1016/j.jappgeo.2011.12.003>.
- Gilbert, Graham et al. (2019). "Characterization of two sites for geotechnical testing in permafrost: Longyearbyen, Svalbard". In: *AIMS Geosciences* 5.4, pp. 868–885. ISSN: 2471-2132. DOI: [10.3934/geosci.2019.4.868](https://doi.org/10.3934/geosci.2019.4.868).
- Gilbert, Graham L. et al. (2018). "Late Quaternary sedimentation and permafrost development in a Svalbard fjord-valley, Norwegian high Arctic". In: *Sedimentology* 65.7, pp. 2531–2558. ISSN: 13653091. DOI: [10.1111/sed.12476](https://doi.org/10.1111/sed.12476).
- Grima, C. et al. (Jan. 2022). "The Basal Detectability of an Ice-Covered Mars by MARSIS". In: *Geophysical Research Letters* 49.2, e2021GL096518. ISSN: 0094-8276. DOI: [10.1029/2021GL096518](https://doi.org/10.1029/2021GL096518). URL: <https://onlinelibrary.wiley.com/doi/10.1029/2021GL096518>.
- Gwinn, V. E. (Feb. 2006). "Thrust faulting, low-angle". In: *Structural Geology and Tectonics*. Kluwer Academic Publishers, pp. 800–805. DOI: [10.1007/3-540-31080-0\\_119](https://doi.org/10.1007/3-540-31080-0_119). URL: [https://link.springer.com/referenceworkentry/10.1007/3-540-31080-0\\_119](https://link.springer.com/referenceworkentry/10.1007/3-540-31080-0_119).
- Hanssen-Bauer, I., M. Kristensen Solas, and E. L. Steffensen (1990). *The climate of Spitsbergen*. Tech. rep., pp. 39/90.
- Harvey, Adrian M., Anne E. Mather, and Martin Stokes (2005). "Alluvial fans: Geomorphology, sedimentology, dynamics - Introduction. A review of alluvial-fan research". In: *Geological Society Special Publication* 251, pp. 1–7. ISSN: 03058719. DOI: [10.1144/GSL.SP.2005.251.01.01](https://doi.org/10.1144/GSL.SP.2005.251.01.01).
- Hauber, E. et al. (2011). "Landscape evolution in Martian mid-latitude regions: Insights from analogous periglacial landforms in Svalbard". In: *Geological Society Special Publication* 356, pp. 111–131. ISSN: 03058719. DOI: [10.1144/SP356.7](https://doi.org/10.1144/SP356.7).
- Hervé, Y. et al. (Sept. 2020). "The WISDOM radar on board the ExoMars 2022 Rover: Characterization and calibration of the flight model". In: *Planetary and Space Science* 189, p. 104939. ISSN: 00320633. DOI: [10.1016/j.pss.2020.104939](https://doi.org/10.1016/j.pss.2020.104939).
- Hinkel, K. M. et al. (2001). "Detection of subsurface permafrost features with ground-penetrating radar, Barrow, Alaska". In: *Permafrost and Periglacial Processes* 12.2, pp. 179–190. ISSN: 10456740. DOI: [10.1002/ppp.369](https://doi.org/10.1002/ppp.369).
- Hornum, Mikkel Toft et al. (2020). "Numerical modelling of permafrost spring discharge and open-system pingo formation induced by basal permafrost aggradation". In: *Cryosphere* 14.12, pp. 4627–4651. ISSN: 19940424. DOI: [10.5194/tc-14-4627-2020](https://doi.org/10.5194/tc-14-4627-2020).
- Huber, Emanuel and Guillaume Hans (2018). "RGPR — An open-source package to process and visualize GPR data". In: *2018 17th International Conference on Ground Penetrating Radar (GPR)*, pp. 1–4. DOI: [10.1109/ICGPR.2018.8441658](https://doi.org/10.1109/ICGPR.2018.8441658).
- Humlum, Ole, Arne Instanes, and Johan Ludvig Sollid (Dec. 2003). "Permafrost in Svalbard: a review of research history, climatic background and engineering challenges". In: *Polar Research* 22.2, pp. 191–215. ISSN: 0800-0395. DOI: [10.1111/j.1751-8369.2003.tb00107.x](https://doi.org/10.1111/j.1751-8369.2003.tb00107.x). URL: <http://www.polarresearch.net/index.php/polar/article/view/6455>.
- Janocha, Julian et al. (2021). "Seeing beyond the outcrop: Integration of ground-penetrating radar with digital outcrop models of a paleokarst system". In: *Marine and Petroleum Geology* 125, June 2020, p. 104833. ISSN: 02648172. DOI: [10.1016/j.marpetgeo.2020.104833](https://doi.org/10.1016/j.marpetgeo.2020.104833). URL: <https://doi.org/10.1016/j.marpetgeo.2020.104833>.
- Jeppesen, J.W. (2001). "Palæoklimatiske indikatorer for central Spitsbergen, Svalbard. Eksemplificeret vedstudier af iskiler og deres værtssediment". PhD thesis. University of Copenhagen, p. 101.
- Jol, Harry (2009). *Ground Penetrating Radar*. Elsevier. ISBN: 9780444533487. DOI: [10.1016/B978-0-444-53348-7.X0001-4](https://doi.org/10.1016/B978-0-444-53348-7.X0001-4).
- Kartozzi, Andrei (July 2019). "Assessment of the Ice Wedge Polygon Current State by Means of UAV Imagery Analysis (Samoylov Island, the Lena Delta)". In: *Remote Sensing* 11.13, p. 1627. ISSN: 2072-4292. DOI: [10.3390/rs11131627](https://doi.org/10.3390/rs11131627). URL: <https://www.mdpi.com/2072-4292/11/13/1627>.
- Kearey, Philip and Micheal Brooks (2002). *An Introduction to Geophysical Exploration*. 3rd. Oxford, UK: Blackwell Science Ltd. ISBN: 9780632049295.

- Kminek, Gerhard and Jeffrey L. Bada (May 2006). “The effect of ionizing radiation on the preservation of amino acids on Mars”. In: *Earth and Planetary Science Letters* 245.1-2, pp. 1–5. ISSN: 0012821X. DOI: [10.1016/j.epsl.2006.03.008](https://doi.org/10.1016/j.epsl.2006.03.008).
- Kreslavsky, Mikhail A, James W Head, and David R Marchant (2008). “Periods of active permafrost layer formation during the geological history of Mars: Implications for circum-polar and mid-latitude surface processes”. In: *Planetary and Space Science* 56.2, pp. 289–302.
- Lachenbruch, A H (1963). “Contraction theory of ice-wedge polygons: a qualitative discussion.” In: *Nat. Acad. Sci., Natl. Res. Counc. Publ.* 1287, pp. 63–71.
- Lapazaran, Javier et al. (2013). “Ice volume changes (1936-1990-2007) and ground-penetrating radar studies of ariebreun, hornsund, spitsbergen”. In: *Polar Research* 32.SUPPL. Pp. 1–10. ISSN: 17518369. DOI: [10.3402/polar.v32i0.11068](https://doi.org/10.3402/polar.v32i0.11068).
- Laskar, Jacques, Benjamin Levrard, and John F. Mustard (Sept. 2002). “Orbital forcing of the martian polar layered deposits”. In: *Nature* 419.6905, pp. 375–377. ISSN: 00280836. DOI: [10.1038/nature01066](https://doi.org/10.1038/nature01066). URL: <https://www.nature.com/articles/nature01066>.
- Lefort, A. et al. (Apr. 2009). “Observations of periglacial landforms in Utopia Planitia with the High Resolution Imaging Science Experiment (HiRISE)”. In: *Journal of Geophysical Research* 114.E4, E04005. ISSN: 0148-0227. DOI: [10.1029/2008JE003264](https://doi.org/10.1029/2008JE003264). URL: <http://doi.wiley.com/10.1029/2008JE003264>.
- Leucci, Giovanni (2008). “Ground Penetrating Radar: The Electromagnetic Signal Attenuation and Maximum Penetration Depth”. In: *Scholarly Research Exchange* 2008, pp. 1–7. ISSN: 1687-8299. DOI: [10.3814/2008/926091](https://doi.org/10.3814/2008/926091).
- Levrard, Benjamin et al. (Oct. 2004). “Recent ice-rich deposits formed at high latitudes on Mars by sublimation of unstable equatorial ice during low obliquity”. In: *Nature* 431.7012, pp. 1072–1075. ISSN: 00280836. DOI: [10.1038/nature03055](https://doi.org/10.1038/nature03055). URL: <http://arxiv.org/astro-ph/03036601>.
- Levy, J. S., J. W. Head, and D. R. Marchant (2011). “Gullies, polygons and mantles in Martian permafrost environments: Cold desert landforms and sedimentary processes during recent Martian geological history”. In: *Geological Society Special Publication* 354, pp. 167–182. ISSN: 03058719. DOI: [10.1144/SP354.10](https://doi.org/10.1144/SP354.10).
- Levy, Joseph, James Head, and David Marchant (Jan. 2009). “Thermal contraction crack polygons on Mars: Classification, distribution, and climate implications from HiRISE observations”. In: *Journal of Geophysical Research* 114.E1, E01007. ISSN: 0148-0227. DOI: [10.1029/2008JE003273](https://doi.org/10.1029/2008JE003273). URL: <http://doi.wiley.com/10.1029/2008JE003273>.
- Mackay, J. Ross (Jan. 1990). “Some observations on the growth and deformation of epigenetic, syngenetic and anti-syngenetic ice wedges”. In: *Permafrost and Periglacial Processes* 1.1, pp. 15–29. ISSN: 10456740. DOI: [10.1002/ppp.3430010104](https://doi.org/10.1002/ppp.3430010104). URL: <https://onlinelibrary.wiley.com/doi/10.1002/ppp.3430010104>.
- (1998). “Pingo growth and collapse, Tuktoyaktuk Peninsula area, western arctic coast, Canada: A long-term field study”. In: *Geographie Physique et Quaternaire* 52.3, pp. 271–323. ISSN: 07057199. DOI: [10.7202/004847ar](https://doi.org/10.7202/004847ar).
- Mackay, J Ross and C R Burn (Jan. 2002). “The first 20 years (1978-1979 to 1998–1999) of ice-wedge growth at the Illisarvik experimental drained lake site, western Arctic coast, Canada”. In: *Canadian Journal of Earth Sciences* 39.1, pp. 95–111. ISSN: 0008-4077. DOI: [10.1139/e01-048](https://doi.org/10.1139/e01-048). URL: <http://www.nrcresearchpress.com/doi/10.1139/e01-048>.
- Mackay, J.R. (1980). “Deformation of ice-wedge polygons, Garry Island, Northwest Territories”. In: *Geological Survey Canada* 80-1A, pp. 287–291.
- Major, H. et al. 2000. *Geological map of Svalbard 1:100,000 sheet C9G Adventdalen (revised after Major 1964)*.
- Matsuoka, Norikazu (Oct. 2001). “Solifluction rates, processes and landforms: A global review”. In: *Earth-Science Reviews* 55.1-2, pp. 107–134. ISSN: 00128252. DOI: [10.1016/S0012-8252\(01\)00057-5](https://doi.org/10.1016/S0012-8252(01)00057-5).
- Matsuoka, Norikazu, Hanne H. Christiansen, and Tatsuya Watanabe (2018). “Ice-wedge polygon dynamics in Svalbard: Lessons from a decade of automated multi-sensor monitoring”. In: *Permafrost and Periglacial Processes* 29.3, pp. 210–227. ISSN: 10991530. DOI: [10.1002/ppp.1985](https://doi.org/10.1002/ppp.1985).
- Morgan, R.P.C. (Mar. 1980). “Soil erosion and conservation in Britain”. In: *Progress in Physical Geography: Earth and Environment* 4.1, pp. 24–47. ISSN: 0309-1333. DOI: [10.1177/030913338000400102](https://doi.org/10.1177/030913338000400102). URL: <http://journals.sagepub.com/doi/10.1177/030913338000400102>.
- Munroe, Jeffrey S. et al. (Oct. 2007). “Application of ground-penetrating radar imagery for three-dimensional visualisation of near-surface structures in ice-rich permafrost, Barrow, Alaska”. In: *Permafrost and Periglacial Processes* 18.4, pp. 309–321. ISSN: 10456740. DOI: [10.1002/ppp.594](https://doi.org/10.1002/ppp.594). URL: <https://onlinelibrary.wiley.com/doi/10.1002/ppp.594>.
- Navarro, F. J. et al. (2016). “Estudios de georradar en Svalbard orientados al cálculo del volumen de hielo de sus glaciares”. In: *Cuadernos de Investigacion Geografica* 42.2, pp. 399–414. ISSN: 16979540. DOI: [10.18172/cig.2929](https://doi.org/10.18172/cig.2929).
- Neal, Adrian (Aug. 2004). “Ground-penetrating radar and its use in sedimentology: Principles, problems and progress”. In: *Earth-Science Reviews* 66.3-4, pp. 261–330. ISSN: 00128252. DOI: [10.1016/j.earscirev.2004.01.004](https://doi.org/10.1016/j.earscirev.2004.01.004).
- Oliva, M. et al. (2014). “Sedimentological characteristics of ice-wedge polygon terrain in adventdalen (Svalbard) environmental and climatic implications for the late Holocene”. In: *Solid Earth* 5.2, pp. 901–914. ISSN: 18699529. DOI: [10.5194/se-5-901-2014](https://doi.org/10.5194/se-5-901-2014).
- Orosei, R. et al. (Aug. 2018). “Radar evidence of subglacial liquid water on Mars”. In: *Science* 361.6401, pp. 490–493. ISSN: 10959203. DOI: [10.1126/science.aar7268](https://doi.org/10.1126/science.aar7268). URL: <https://www.science.org/doi/abs/10.1126/science.aar7268>.
- Patton, Peter C. and Stanley A. Schumm (Feb. 1975). “Gully erosion, Northwestern Colorado: A threshold phenomenon”. In: *Geology* 3.2, pp. 88–90. ISSN: 19432682. DOI: [10.1130/0091-7613\(1975\)3<88:GENCAT>2.0.CO;2](https://doi.org/10.1130/0091-7613(1975)3<88:GENCAT>2.0.CO;2). URL: <http://pubs.geoscienceworld.org/gsa/geology/article-pdf/3/2/88/3521842/i0091-7613-3-2-88.pdf>.
- Persico, Raffaele (May 2014). “Inverse scattering and GPR data processing: an Introduction”. In: *EGU General Assembly Conference Abstracts*. EGU General Assembly Conference Abstracts, p. 10417.
- Picard, G and M Sandells (2022). “SMRT Documentation”. In.
- Pidwirny, M.J. (2006). *Fundamentals of Physical Geography*. Tech. rep. Okanagan University College.
- Plattner, Alain (2021). “GPRPy: Open-source Ground Penetrating Radar processing and visualization software”. In: *GitHub Repository*. URL: <https://github.com/NSGeophysics/GPRPy>.

- Plettemeier, D et al. (2009). *Design and Performance of the WISDOM Antenna System aboard the ExoMars Rover*. Tech. rep., pp. 2009–11693.
- Poulet, F. et al. (2005). “Phyllosilicates on Mars and implications for early martian climate”. In: *Nature* 438.7068, pp. 623–627. ISSN: 14764687. DOI: [10.1038/nature04274](https://doi.org/10.1038/nature04274).
- Quantin-Nataf, Cathy et al. (Mar. 2021). “Oxia Planum: The Landing Site for the ExoMars “rosalind Franklin” Rover Mission: Geological Context and Prelanding Interpretation”. In: *Astrobiology* 21.3, pp. 345–366. ISSN: 15311074. DOI: [10.1089/ast.2019.2191](https://doi.org/10.1089/ast.2019.2191). URL: <https://www.liebertpub.com/doi/10.1089/ast.2019.2191>.
- Reynolds, John M (2011). *An introduction to applied and environmental geophysics*. John Wiley & Sons.
- Robinson, Enders A and Dean Clark (2017). *Basic geophysics*. Society of Exploration Geophysicists.
- Ross, Neil et al. (2005). “Ground penetrating radar investigations of open system pingos, Adventdalen, Svalbard”. In: *Norsk Geografisk Tidsskrift* 59.2, pp. 129–138. ISSN: 00291951. DOI: [10.1080/00291950510020600](https://doi.org/10.1080/00291950510020600).
- Ross, Neil et al. (2007). “Internal structure of open system pingos, adventdalen, svalbard: The use of resistivity tomography to assess ground-ice conditions”. In: *Journal of Environmental and Engineering Geophysics* 12.1, pp. 113–126. ISSN: 10831363. DOI: [10.2113/JEEG12.1.113](https://doi.org/10.2113/JEEG12.1.113).
- Rossi, Giuliana et al. (2018). “Seismic survey on an open pingo system in Adventdalen Valley, Spitsbergen, Svalbard”. In: *Near Surface Geophysics* 16.1, pp. 89–103. ISSN: 15694445. DOI: [10.3997/1873-0604.2017037](https://doi.org/10.3997/1873-0604.2017037).
- Schwamborn, Georg et al. (2006). “Ground ice and slope sediments archiving late Quaternary paleoenvironment and paleoclimate signals at the margins of El’gygytgyn Impact Crater, NE Siberia”. In: *Quaternary Research* 66.2, pp. 259–272. ISSN: 00335894. DOI: [10.1016/j.yqres.2006.06.007](https://doi.org/10.1016/j.yqres.2006.06.007).
- Senger, K. et al. (2014). “GPR characterization of a naturally fractured siliciclastic reservoir on Svalbard, Arctic Norway”. In: *Proceedings of the 15th International Conference on Ground Penetrating Radar, GPR 2014*, pp. 285–290. DOI: [10.1109/ICGPR.2014.6970430](https://doi.org/10.1109/ICGPR.2014.6970430).
- Sensors&Software (1996). *Technical Manual 21: PulseEKKO Basic Plotting and Editing*. Tech. rep. Ontario: Sensors and Software.
- Sidorchuk, Alexey Yu and Tatiana A. Matveeva (Apr. 2020). “Periglacial gully erosion on the east european plain and its recent analog at the Yamal Peninsula”. In: *Geography, Environment, Sustainability* 13.1, pp. 183–194. ISSN: 25421565. DOI: [10.24057/2071-9388-2019-01](https://doi.org/10.24057/2071-9388-2019-01). URL: <https://ges.rgo.ru/jour/article/view/1043>.
- Slaymaker, Olav (Jan. 2009). “Proglacial, periglacial or paraglacial?” In: *Geological Society Special Publication* 320.1, pp. 71–84. ISSN: 03058719. DOI: [10.1144/SP320.6](https://doi.org/10.1144/SP320.6). URL: <https://sp.lyellcollection.org/content/320/1/71https://sp.lyellcollection.org/content/320/1/71.abstract>.
- Smith, P. H. et al. (July 2009). “H<sub>2</sub>O at the phoenix landing site”. In: *Science* 325.5936, pp. 58–61. ISSN: 00368075. DOI: [10.1126/science.1172339](https://doi.org/10.1126/science.1172339). URL: <https://www.science.org/doi/abs/10.1126/science.1172339>.
- Soare, R. J. et al. (July 2014). “Possible open-system (hydraulic) pingos in and around the Argyre impact region of Mars”. In: *Earth and Planetary Science Letters* 398, pp. 25–36. ISSN: 0012821X. DOI: [10.1016/j.epsl.2014.04.044](https://doi.org/10.1016/j.epsl.2014.04.044).
- Sørbel, L. and J. Tolgensbakk (2002). “Ice-wedge polygons and solifluction in the Adventdalen area, Spitsbergen, Svalbard”. In: *Norsk Geografisk Tidsskrift* 56.2, pp. 62–66. ISSN: 00291951. DOI: [10.1080/002919502760056369](https://doi.org/10.1080/002919502760056369). URL: <https://www.tandfonline.com/doi/abs/10.1080/002919502760056369>.
- Sullivan, Bane and Alexander Kaszynski (May 2019). “PyVista: 3D plotting and mesh analysis through a streamlined interface for the Visualization Toolkit (VTK)”. In: *Journal of Open Source Software* 4.37, p. 1450. DOI: [10.21105/joss.01450](https://doi.org/10.21105/joss.01450). URL: <https://doi.org/10.21105/joss.01450>.
- Toulmin, Priestley et al. (Sept. 1977). “Geochemical and mineralogical interpretation of the Viking inorganic chemical results”. In: *Journal of Geophysical Research* 82.28, pp. 4625–4634. ISSN: 01480227. DOI: [10.1029/JS082i028p04625](https://doi.org/10.1029/JS082i028p04625). URL: <http://doi.wiley.com/10.1029/JS082i028p04625>.
- Ulrich, Mathias (2011). “Permafrost landform studies on Earth: Implications for periglacial landscape evolution and habitability on Mars”. PhD thesis. DOI: [10.13140/RG.2.1.2738.7929](https://doi.org/10.13140/RG.2.1.2738.7929).
- Ulrich, Mathias et al. (July 2014). “Quantifying Wedge-Ice Volumes in Yedoma and Thermokarst Basin Deposits”. In: *Permafrost and Periglacial Processes* 25.3, pp. 151–161. ISSN: 10456740. DOI: [10.1002/ppp.1810](https://doi.org/10.1002/ppp.1810). URL: <https://onlinelibrary.wiley.com/doi/10.1002/ppp.1810>.
- Vago, Jorge L. et al. 2017. *Habitability on Early Mars and the Search for Biosignatures with the ExoMars Rover*. URL: <https://www.liebertpub.com/doi/abs/10.1089/ast.2016.1533>. *Astrobiology*. ISSN: 15311074. DOI: [10.1089/ast.2016.1533](https://doi.org/10.1089/ast.2016.1533).
- Van Everdingen, Robert O. (1998). “Multi-language glossary of permafrost and related ground-ice terms (Rev. ed. 2005)”. In: *International Permafrost Association* 1998.revised, p. 159. URL: [https://globalcryospherewatch.org/reference/glossary\\_docs/Glossary\\_of\\_Permafrost\\_and\\_Ground-Ice\\_IPA\\_2005.pdf](https://globalcryospherewatch.org/reference/glossary_docs/Glossary_of_Permafrost_and_Ground-Ice_IPA_2005.pdf).
- Vaughn, Lydia J.S. and Margaret S. Torn (2018). “Radiocarbon measurements of ecosystem respiration and soil pore-space CO<sub>2</sub> in Utqiagvik (Barrow), Alaska”. In: *Earth System Science Data* 10.4, pp. 1943–1957. ISSN: 18663516. DOI: [10.5194/essd-10-1943-2018](https://doi.org/10.5194/essd-10-1943-2018).
- Wales, Nathan A. et al. (2020). “Understanding the relative importance of vertical and horizontal flow in ice-wedge polygons”. In: *Hydrology and Earth System Sciences* 24.3, pp. 1109–1129. ISSN: 16077938. DOI: [10.5194/hess-24-1109-2020](https://doi.org/10.5194/hess-24-1109-2020).
- Warren, Craig (2009). *Numerical modelling of high-frequency ground-penetrating radar antennas*. Tech. rep. URL: <https://era.ed.ac.uk/handle/1842/4074>.
- Washburn, A.L. (1979). *Geocryology - A Survey of Periglacial Processes and Environments*. Tech. rep. London: Arnold Ltd.
- Watanabe, T et al. (2008). “Sounding ice and soil wedge structures with ground-penetrating radar”. In: *Proceedings of the Ninth International Conference on Permafrost, Kane DL, Hinkel KM (eds). Institute of Northern Engineering University of Alaska Fairbanks: Fairbanks*. Vol. 1933-1938.
- Watanabe, Tatsuya, Norikazu Matsuoka, and Hanne H. Christiansen (Jan. 2013). “Ice- and Soil-Wedge Dynamics in the Kapp Linné Area, Svalbard, Investigated by Two- and Three-Dimensional GPR and Ground Thermal and Acceleration Regimes”. In: *Permafrost and Periglacial Processes* 24.1, pp. 39–55. ISSN: 10456740. DOI: [10.1002/ppp.1767](https://doi.org/10.1002/ppp.1767).

- Wilhelm, Roland C. et al. (2012). “Life at the wedge: The activity and diversity of arctic ice wedge microbial communities”. In: *Astrobiology* 12.4, pp. 347–360. ISSN: 15311074. DOI: [10.1089/ast.2011.0730](https://doi.org/10.1089/ast.2011.0730).
- WISDOM-radar. 2022. *WISDOM-radar*. URL: <https://www.wisdom-radar.eu/>. Accessed: 2022-03-19.
- Yershov, Eduard Dmitrievich (2004). *General geocryology*. Cambridge university press.
- Yoshikawa, Kenji (1993). “Notes on open-system pingo ice, Adventdalen, Spitsbergen”. In: *Permafrost and Periglacial Processes* 4.4, pp. 327–334. ISSN: 10991530. DOI: [10.1002/ppp.3430040405](https://doi.org/10.1002/ppp.3430040405).
- Zhang, T. et al. (Apr. 1999). “Statistics and characteristics of permafrost and ground-ice distribution in the Northern Hemisphere”. In: *Polar Geography* 23.2, pp. 132–154. ISSN: 19390513. DOI: [10.1080/10889379909377670](https://doi.org/10.1080/10889379909377670).

# A. Appendix

## A.1 Preliminary Study

The aim of the preliminary study is to assess the performance of the pulseEKKO systems (high and low frequency) in two well-known areas and to provide the key information of the soil properties to WISDOM as well as defining basic processes for the processing pipelines. In addition, this initial fieldwork campaign exposes challenges and problems that will need to be taken into account on future sessions (eg. handling of equipment at low temperatures, efficient preparation and in-situ organisation to avoid unnecessary exposure to harsh weather).

### A.1.1 Old Aurora Station

The Old Aurora Station is located 5 km southeast from Longyearbyen following the road that connects the town with the different mining complex. Parallel to the road ice wedge polygons are found and provide a relatively good site for quick measurements (a drawback is the presence of some electrical installations and underground pipes to feed water on nearby houses). The aim is to do a single line with all available frequencies for pulseEkko and compare the results. Unfortunately, after half a day of HF measurements the pulseEkko DVL stopped working so new data on LF could not be retrieved. Instead, data from 2012 has been used as it fullfills the same goal, comparing the LF to the HF system. [Table A.1](#) presents the data on the starting and ending position of each of the profiles as well as its corrected length. On [Table A.2](#) it is shown the different GPR parameters utilised for each of the frequencies.

Table A.1: Start and End positions for GPR measurements at Aurora station. HF measurements were taken on 02/03/2022 between 11h and 12h. The LF measurements took place 28/02/2012 and 29/02/2012 for Line 6 and 12, respectively.

Line	Frequency [MHz]	Start Position UTM 33 [m]		End Position UTM 33 [m]		Length [m]	
		E	N	E	N	Calculated	Corrected
HF	900	518826	8681051	518658	8681199	224.24	224.74
HF	450	518821	8681053	518656	8681200	220.68	221.18
HF	225	518822	8681053	518658	8681199	219.57	220.07
6	50	518649	8681157	518797	8681043	186.82	-
12	100	518636	8681166	518784	8681057	183.81	-

Table A.2: GPR acquisition parameters during Aurora station fieldwork

	Frequency				
	50 MHz	100 MHz	225 MHz	450 MHz	900MHz
Antenna Separation [m]	2	1	0.5	0.25	0.17
Time window [ns]	304	300	70	40	40
Sampling Interval [ns]	1.6	0.8	0.4	0.2	0.1
Step Size [m]	0.25	0.25	0.5	0.5	0.5
Num. Stacks	8	8	8	8	8
Trigger method	Odometer	Odometer	Odometer	Odometer	Odometer

Figure A.1.a shows a map of the polygon area with three different lines. Each of the lines has a start and end, corresponding to the direction in which the GPR started to take measurements. Along the lines numbered inverted triangles are found. These symbols indicate an intersection between the profile line and a polygon trough visible on the aerial picture and it is expected a response from the GPR, provided that below the trough lies an ice wedge. Nevertheless, chances are some troughs are not visible (hence no marker) but the GPR records a response and viceversa, a trough is marked but triggering no GPR response owing to no ice wedge. Note that the LineHF has been recorded in the opposite direction than Line6 and Line12 but all results are displayed from left to right.

Figure A.1.b shows the GPR response for the LF system. The 100MHz profile distinguishes to different regions: an upper layer ca. 1 m depth, corresponding to the active layer of the terrain, and a more noisy layer that can be detected up to 4 m depth, the permafrost. The latter reveals very strong reflectors with the shape of an hyperbola which correspond to wedge ice. The GPR registers these hyperbolic reflections due to a steep change in the dielectric constant (from permafrost to pure ice) and their sharp edges. Focusing on Line 12 (green line on Figure A.1.a), out of 13 points marked as potentially hosting an ice wedge the pulseEKKO indicates that marking #1 contains no wedge ice and that an ice wedge is located at A, a midway point between markings 10 and 11. On the other hand, Line 6 misses a total of six ice wedges beneath a marked trough. Furthermore, the transition between the active layer and the permafrost is pushed downwards and more diffuse (some hyperbolas seem cut on the top) than in Line 12.

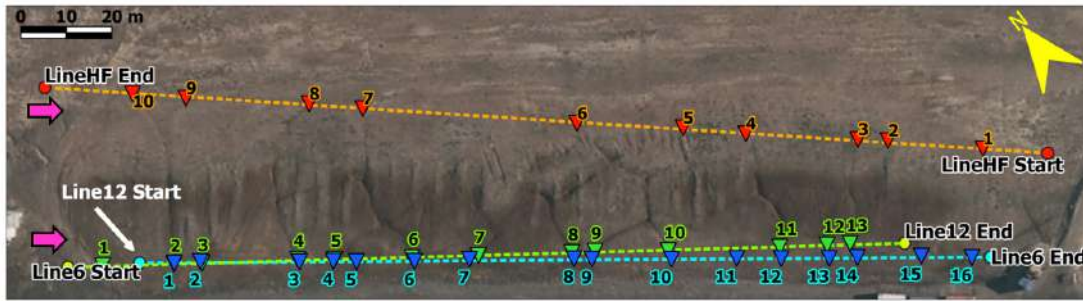
From the results described above can be concluded that 50MHz constitutes a too low frequency if the purpose is mapping ice wedges. Moreover, this frequency fails to provide a correct description of the soil layers even at the most basic level (active layer-permafrost identification). Both profiles, however, might be used to find the velocity in the media via Kirchoff Migration which yields a result of 0.13 m/ns.

The results of the high frequency system are shown in Figure A.2. The most remarkable differences are that two boundary layers (instead of one for the LF) can be distinguished and that no hyperbolic reflectors are found. The 900MHz system gives the most detailed description of the soil stratigraphy: an upper layer of ca. 15-20 cm corresponds to the accumulated snow, up to 1 m depth corresponds to the active layer and below 1 m to permafrost. The ice wedges are detected as a strong reflection on the first and second boundary layers (particularly on the top one). The higher the frequency of the measurement, the stronger the reflection<sup>1</sup>. If one observes troughs marked with 2 and 3, apparently they host no wedge ice beneath. It must be noted that several ice wedges have been missed (points A-F) based on aerial imagery observations as the soil had been altered by the construction of a road, reshaping the terrain and eliminating any trace of troughs. In particular, points B and F should be drilled to confirm the presence of an ice wedge. The reflection at point B at 225 MHz is faint but hints a vertical reflection until 2.5 m depth. At 900 MHz the reflection is revealed to be contained exclusively at 0.8 m depth and rules out wedge ice (could be for example, a stone). Point F presents a ringing effect at frequency 225 MHz that totally disappears at 900 MHz. As this effect is at the edge of the profile, it is difficult to judge. Nevertheless, constant-with-depth horizontal reflections are associated with man-made objects such as pipelines, electric cables, metal bars, etc. It is possible that the 225 MHz profile finished where a pipeline was located while the 900MHz managed to avoid it.

The HF system higher resolution allows to identify accurately the different soil layers but in turn, makes profile interpretation more challenging as a growing number of anomalies appear on the radargram and need to be distinguished from those stemming from wedge ice. Moreover, the absence of hyperbolas makes not possible to determine the velocity via Kirchoff migration. Instead, as penetration is roughly the same for LF and HF systems, it is assumed that 0.13 m/ns still holds.

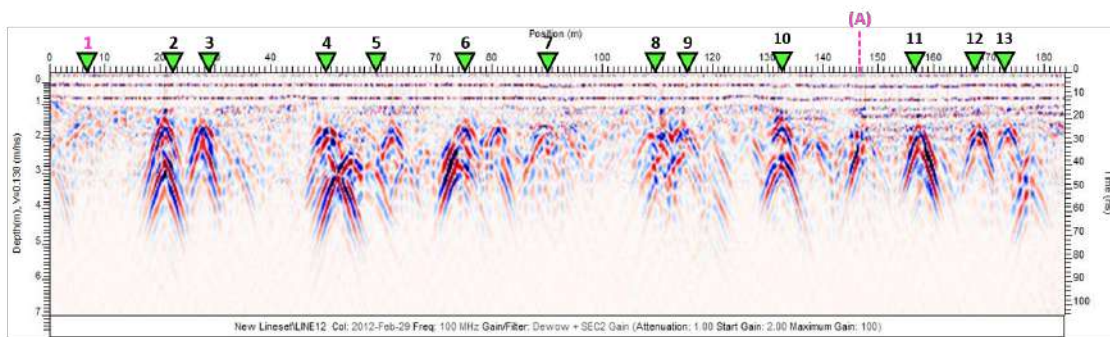
<sup>1</sup>This can only be directly observed if profiles have the same processing steps including gain. This is the case for 225 MHz and 450 MHz



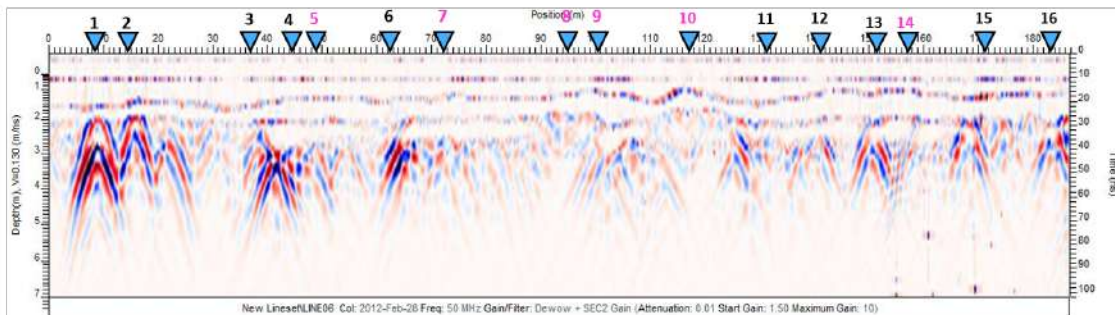


(a)

**Line 12 (100 MHz)**



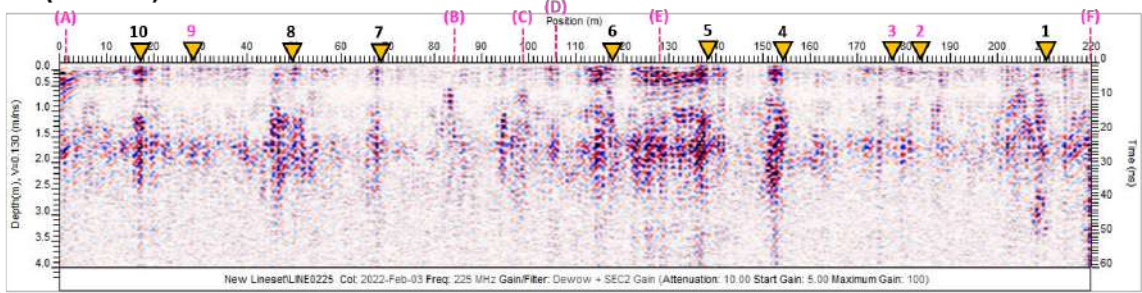
**Line 6 (50MHz)**



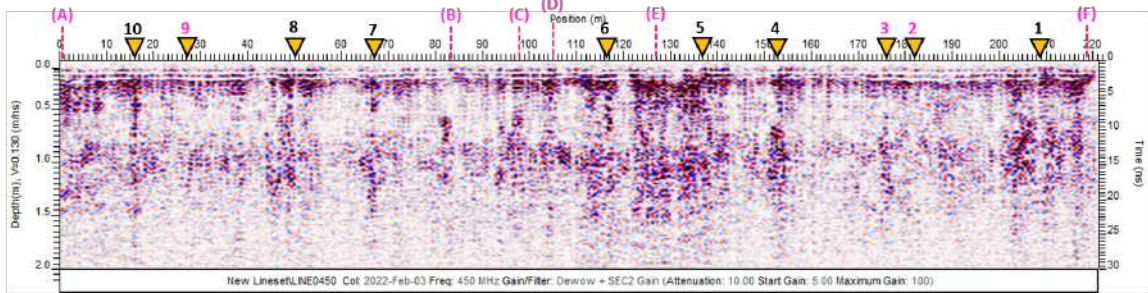
(b)

Figure A.1: a) Map of Old Aurora profile lines (Background image: © Norwegian Polar Institute/CC BY 4.0). b) and c) Old Aurora LF measurements.

**Line HF (225 MHz)**



**Line HF (450 MHz)**



**Line HF (900 MHz)**

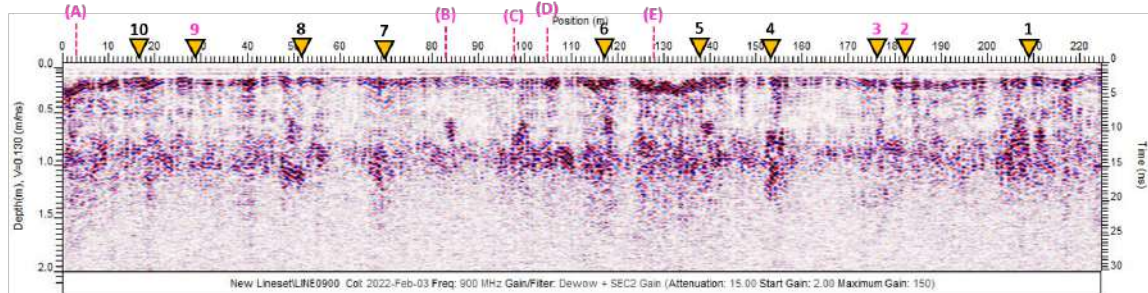


Figure A.2: Old Aurora Station, high frequency profiles